OPTIMIZATION OF FUNCTIONAL PERFORMANCE OF ADDITIVELY MANUFACTURED COBALT-CHROMIUM-MOLYBDENUM ALLOY FOR DENTAL IMPLANTS

AMOS MAGARI NYAKUNDI

MASTER OF SCIENCE

(Mechatronic Engineering)

JOMO KENYATTA UNIVERSITY

OF

AGRICULTURE AND TECHNOLOGY

2024

Optimization of Functional Performance of Additively Manufactured Cobalt-Chromium-Molybdenum Alloy for Dental Implants

Amos Magari Nyakundi

A Thesis Submitted in Partial Fulfilment of the Requirements for the Degree of Master of Science in Mechatronic Engineering of the Jomo Kenyatta University of Agriculture and Technology

2024

DECLARATION

This thesis is my original work and has not been presented for a degree in any other University

Signature…….Date…….

Amos Magari Nyakundi

This thesis has been submitted for examination with our approval as the University Supervisors

Signature…….Date…….

Dr. Martin Ruthandi Maina, PhD

JKUAT, Kenya

Signature……...Date……

Dr. Prasad Ventaka Satya Raghupatruni, PhD

BIUST, Botswana

Signature……...Date……

Prof. Eyitayo Olatunde Olakanmi, PhD

BIUST, Botswana

DEDICATION

I dedicate this work to my dear parents.

ACKNOWLEDGEMENT

I am thankful to the almighty God for guiding and protecting me throughout this work. I extend my heartfelt gratitude to my supervisors, Dr. Martin Ruthandi Maina, Dr. Prasad Raghupatruni, and Prof. Eyitayo Olakanmi, for their unwavering encouragement, guidance, and invaluable assistance during this research. May God bless them. I acknowledge the financial support of the Education for Laser-based Manufacturing (ELbM) project funded by the Intra Africa Mobility Scheme and Africa Lacer Center (ALC). I am also grateful to Prof Sisa Pityana, Mr. Nana Arthur, and the Council for Scientific and Industrial Research (CSIR), Pretoria, South Africa staff, for their help in setting up my experiments. In addition, I would like to thank my coursemates, Jomo Kenyatta University of Agriculture and Technology (JKUAT) mechatronic and mechanical engineering members, for their constructive criticism. Lastly, I thank Botswana International University of Science and Technology (BIUST) for hosting me during the ELbM research mobility program.

TABLE OF CONTENTS

DECLARATION ..... **ii**

DEDICATION ..... **iii**

ACKNOWLEDGEMENT ..... **iv**

TABLE OF CONTENTS ..... **v**

LIST OF TABLES ..... **x**

LIST OF FIGURES ..... **xi**

LIST OF SYMBOLS ..... **xiv**

LIST OF APPENDICES ..... **xv**

ACRONYMS AND ABBREVIATIONS ..... **xvi**

ABSTRACT ..... **xvii**

CHAPTER ONE **18**

INTRODUCTION **18**

1.1 Background 18

1.2 Laser Engineered Net Shaping 19

1.3 Biomaterials 19

1.4 Problem Statement 22

1.5 Objectives 23

1.5.1 Main Objective 23

1.5.2 Specific Objectives 23

1.6 Research Questions 23

1.7 Justification 24

1.8 Thesis Structure 24

CHAPTER TWO 25

LITERATURE REVIEW 25

2.1 Introduction 25

2.2 Additive Manufacturing Techniques 25

2.3 Powder Bed Fusion 26

2.3.1 Selective Laser Melting Process 27

2.3.2 Selective Laser Sintering 28

2.3.3 Electron Beam Melting 28

2.4 Directed Energy Deposition 29

2.4.1 Laser Cladding 30

2.4.2 Laser Engineered Net Shaping (LENS) 30

2.5 Influence of LENS Process Parameters 31

2.6 Defects in Additive Manufacturing 36

2.6.1 Lack of Fusion and Porosity Defects 36

2.6.2 Surface Roughness Variations 38

2.7 Overview of Dental Implants 39

2.8 Dental Implant Materials 40

2.8.1 Magnesium and its Alloys 40

2.8.2 Titanium and Its Alloys 40

2.8.3 Stainless Steel and Its Alloys 41

2.8.4 Nitinol Alloys 41

2.8.5 Cobalt Chromium Molybdenum (CoCrMo) Alloy 41

2.9 Techniques for Optimizing Process Parameters 43

2.9.1 Response Surface Methodology 44

2.9.2 Taguchi Method 48

2.10 Summary of Research Gaps 48

CHAPTER THREE 50

METHODOLOGY 50

3.1 Materials 50

3.2 Experimental Procedure 51

3.3 Design of Experiments 54

3.4 Sample Preparations 55

3.4.1 Sample Cutting and Mounting 55

3.4.2 Grinding and Polishing Process 56

3.4.3 Etching Process for Microstructural Analysis 57

3.5 Sample Characterisation 57

3.5.1 Surface Roughness Measurement 57

3.5.2 Porosity Analysis 58

3.5.3 Microstructural Analysis 58

3.5.4 Microhardness Test 58

3.6 Optimization of Input Factors using Response Surface Methodology 59

3.7 Sample Postprocessing and Analysis 60

3.7.1 Heat Treatment 60

3.7.2 Wear Test 60

3.7.3 X-ray diffraction (XRD) 61

3.8 Summary 61

CHAPTER FOUR 63

RESULTS AND DISCUSSION 63

4.1 Results of RSM Model 63

4.1.1 Microhardness of CoCrMo Alloy Samples Fabricated by LENS Technique 63

4.1.2 Porosity of LENS Fabricated CoCrMo Alloy 65

4.1.3 Surface Roughness of LENS Fabricated CoCrMo Samples 66

4.2 Confirmation of the Adequacy of the Statistical Models 68

4.3 Influence of LENS Process Parameters on the Quality Properties of the Samples 72

4.3.1 Influence of LENS Deposition Variables on Microhardness 72

4.3.2 Effect of LENS Input Parameters on Surface Roughness 78

4.3.3 Effect of LENS Input Parameters on Porosity 82

4.4 Multi-objective Optimization 87

4.5 Validation of Optimum Parameters 88

4.6 X-Ray Diffraction and Wear Rate 89

CHAPTER FIVE 92

CONCLUSIONS AND RECOMMENDATIONS 92

5.1 Conclusions 92

5.2 Recommendations 93

REFERENCES 94

APPENDICES 120

LIST OF TABLES

Table 2.1: Properties of CoCrMo Alloy 42

Table 3.1: Chemical Composition of Cobalt-Chromium-Molybdenum alloy (wt%) as Verified by Electron Dispersive Spectrum (EDS). 50

Table 3.2: List of Equipment 52

Table 3.3: The selected Input Factors 55

Table 3.4: Process Parameters Designed According to the CCD Matrix Approach . 55

Table 4.1: Process Parameters and Results of the CCD Matrix Approach 64

Table 4.2: ANOVA for Microhardness. 64

Table 4.3: ANOVA for Porosity. 66

Table 4.4: ANOVA Results for Surface Roughness in LENS 68

Table 4.5: Confirmatory Tests for Mathematical Models 71

Table 4.6: Optimization Criteria. 88

Table 4.7: RSM Numerical Optimization 88

Table 4.8: Validation Tests Comparing Predicted and Experimental Findings 88

LIST OF FIGURES

Figure 1.1: Particles Release from a Dental Implant 21

Figure 2.1: Schematic Representation of the PBF Process 27

Figure 2.2: Principle of the DED Process 29

Figure 2.3: Schematic Representation of the Coaxial Powder System and Preplaced Powder System 30

Figure 2.4: Schematic Representation of Laser Engineered Net Shaping Process.. 31

Figure 2.5: Porosity Observed in A Sample: a) Keyhole Porosity; b) Gas Porosity 37

Figure 2.7: Steps of RSM..... 44

Figure 2.8: Contour Plot and Surface Plot of a Response Surface..... 46

Figure 3.1: SEM Micrograph of As-Received CoCrMo Alloy Powders..... 51

Figure 3.2: Optomec LENS Machine Used in the Study 52

Figure 3.3: Fabricated Block Samples..... 53

Figure 3.4: Flowability Chart of the Powder 54

Figure 3.5: Mounted Samples. 56

Figure 3.6: Grinding and Polishing Machine at CSIR..... 56

Figure 3.7: Experimental Set Up for Electro-Etching. 57

Figure 3.8: Vickers Indentations on CoCrMo Surface Manufactured by LENS 59

Figure 4.1: Plot of Predicted vs. Actual values of microhardness 69

Figure 4.2: Predicted vs. Actual Values of Porosity 69

Figure 4.3: Predicted vs. Measured Values of Surface Roughness 70

Figure 4.4: Comparison of Microhardness with Process Parameters 73

Figure 4.5: Microstructural Evaluation of LENS Manufactured CoCrMo Samples at Varying Process Parameters 74

Figure 4.6: Contour Graph of the Interaction Effect of Laser Power versus Powder Feed Rate on Microhardness..... 77

Figure 4.7: Contour Graph of the Interaction Effect of Scan Speed versus Powder Feed Rate on Microhardness..... 77

Figure 4.8: Contour Graph of the Interaction Effect of Scan Speed versus Laser Power on Microhardness..... 78

Figure 4.9: Main Effects Plot for Surface Roughness 79

Figure 4.10: Fabricated Samples Under Different Process Parameters..... 79

Figure 4.11: Contour Plot of the Interaction Effect of Laser Power and Scan Speed on Surface Roughness..... 81

Figure 4.12: Contour Plot of the Interaction Effect of Laser Power and Powder Feed Rate on Surface Roughness 82

Figure 4.13: Contour Plot of the Interaction Effect of Scan Speed and Powder Feed Rate on Surface Roughness 82

Figure 4.14: Main Effects Plot for Percentage Porosity..... 83

Figure 4.15: Porosity Images for CoCrMo Alloy Specimen as a Function of Scan Speed..... 84

Figure 4.16: Contour Plot of the Interaction Effect of Scan Speed and Laser Power on Porosity 86

Figure 4.17: Contour Plot of the Interaction Effect of Laser Power and Powder Feed Rate on Porosity. 86

Figure 4.18: Contour Plot of the Interaction Effect of Scan Speed and Powder Feed Rate on Porosity. 87

Figure 4.19: SEM Micrograph of the Optimized Sample. 89

Figure 4.20: XRD Pattern Obtained on As-Built and Heat-Treated LENS-Processed CoCrMo Samples 90

Figure 4.21: SEM Image of the Wear Scars 91

LIST OF SYMBOLS

ϵ	error
d	laser spot size, mm
g_f	gram force, $g\,f$
g/min	grams per minute
μm	micrometers
h	hatch spacing, mm
t	layer thickness, mm
P	laser power, W
$\mathbf{R^2}$	coefficient of determination
v	scanning speed, mm/s

LIST OF APPENDICES

Appendix I: Publications 120

Appendix II: Chemical Composition of Cobalt-Chromium Molybdenum alloy 121

Appendix III: Flowability Study 122

ACRONYMS AND ABBREVIATIONS

AM	Additive Manufacturing
ANOVA	Analysis of Variance
CoCrMo	Cobalt-Chromium-Molybdenum
CAD	Computer Aided Design
DED	Directed Energy Deposition
DMLS	Direct Metal Laser Sintering
EBM	Electron Beam Melting
E_D	Energy Density
GRGA	Grey Relational Grade Analysis
LENS	Laser Engineered Net Shaping
LPBF	Laser Powder Bed Fusion
RSM	Response Surface Methodology
SLM	Selective Laser Melting
SLS	Selective Laser Sintering
SiC	Silicon Carbide
XRD	X-Ray Diffraction

ABSTRACT

Laser Engineered Net Shaping (LENS) allows the manufacture of geometries that include complex structures that are difficult to manufacture with conventional manufacturing methods. Recent developments in additive manufacturing technologies offer a pathway for the clinical success of dental surgeries. Cobalt chromium alloys are used for dental implant applications due to their excellent characteristics. To solve the LENS fabrication challenge, this work utilized response surface methodology (RSM) to investigate the influence of LENS deposition parameters on the microstructural and mechanical performance of the manufactured samples for dental implant applications. Central Composite Design (CCD) was used to design the experiments. The experiments were carried out to investigate the influence of the scanning speed, laser power and powder feed rate on the mechanical performance and microstructural characteristics of CoCrMo alloy fabricated by LENS process. Analysis of statistical data demonstrated that microhardness and porosity were both significantly influenced by laser scan speed and powder feed rate, while surface roughness is impacted substantially by laser scan speed and laser power. The analysis of the responses revealed that the optimum factors were at a scan speed of 5.3 mms^{-1}, powder feed rate of 4.748 $gmin^{-1}$ and laser power of 386.896 W to give surface roughness, porosity, and microhardness responses of 8.7775 μm, 0.06 %, and 387.4286 HV, respectively. The models revealed a strong interaction between the actual experimental data and RSM-predicted responses. The X-ray Diffraction (XRD) pattern of the samples revealed sharp peaks correlating with the phases of CoCrMo alloys that include γ face-centered cubic (FCC) phase and ϵ hexagonal close-packed (HCP) phase. In addition, the wear test on the optimum samples indicates an improvement in wear resistance after heat treatment. The results of this research will serve as a guide for determining suitable LENS input factors for the manufacture of dental implants.

CHAPTER ONE

INTRODUCTION

This chapter provides an overview of the additive manufacturing process. The Laser Engineered Net Shaping process, advantages, challenges, and materials are described. In addition, the objectives of this study and a description of the problem have been presented.

1.1 Background

Commercial and research applications for pharmaceutical and biomedical goods have grown significantly interested in additive manufacturing (AM). The term additive manufacturing refers to the processing methods that allow layer-by-layer fabrication of ceramic, composite or metallic structures from computer-aided design (CAD) files (Pothala & Raju, 2023). AM is increasingly applied in manufacturing companies due to its unique characteristics. Sustainable AM has several advantages like enhanced product functionality, eco-friendly designs, design freedom, improved resource efficiency, and generation of lightweight geometries (Agrawal & Vinodh, 2022; Arif, et al., 2023). The AM process involves building a three-dimensional object from a CAD model by adding materials in a layer-by-layer method which is different from the conventional manufacturing methods that are subtractive in nature (Zhang, Li, & Liou, 2022; Mahamood & Akinlabi, 2017; Akinlabi, et al., 2019). Traditional manufacturing techniques, such as forging and casting, require a detailed planning process to identify the machining steps to achieve the physical geometries. For instance, in computer numerical control (CNC) machining, specific materials require selecting the appropriate tools, and the tool path should be designed carefully to prevent the crashing of the tool. Contrary to the traditional manufacturing methods, AM uses laser power as the tool in melting powder hence reducing machine set-up times and wearing of the tool (Zhang & Liou, 2021). Parts that are difficult to manufacture by traditional processing, like the parts with hollow features, can easily be built by AM. In addition, it is now easy to build an assembly that entails several components. AM also offers more personalized, highly optimized, and customized solutions since the geometry of a part can easily be adjusted (Mahajan, Singh, & Devgan, 2023). Creating personalized parts such as dental

bridges and implants is faster and easier.

1.2 Laser Engineered Net Shaping

Laser Engineered Net Shaping (LENS) is used to manufacture metal components from a CAD solid model. The powder material is added to a melt pool by a nozzle. This technique does not use a powder bed like other additive manufacturing processes like selective laser melting (Kumar & Prasad, 2021; Riza, Masood, & Wen, 2014). It is a blown-powder method. The LENS technique is used to build components with complex geometries and repair damaged components. The technique has a few limitations, such as poor surface finish of the components, the need for postprocessing, and distortion of a part due to residual stresses (Kumar & Prasad, 2021). LENS uses a larger spot size and a higher laser power than other additive manufacturing techniques, making its deposition rate higher. The process allows the varying of the powder composition by using multiple powder feeders, which is important when making a component with different compositions (Avila, Bose, & Bandyopadhyay, 2018). Mixing different powder material ratios at the melt pool makes it possible to research new metallurgical phenomena. In other additive manufacturing processes, such as selective laser melting (SLM) and selective laser sintering (SLS), the powders are premixed before melting. Contrary to other AM methods, such as SLM, LENS can be used to fabricate implants with less powder requirement (Izadi, Farzaneh, Mohammed, Gibson, & Rolfe, 2020). The LENS process parameters should be optimized to fabricate parts with high wear resistance, low surface roughness, and high mechanical properties.

1.3 Biomaterials

Human organs and tissues sometimes fail to execute regular actions due to age, injuries, or degeneration. Some of these conditions are managed using medication. Nevertheless, some of the conditions cannot be rectified by using medicines and necessitate using biomaterials (Kiran & Ramakrishna, 2021). Biomaterials are used to support physiological body functions or replace body components. They are used to recompose different tissues to improve the patient's quality of life. The distinguishing factor of a biomaterial from other materials is the ability to exist in contact with human body tissues without causing damage to the body tissue (Kiran & Ramakrishna, 2021;

Gobbi, et al., 2020). The requirements of biomaterials before they are used in the body include being non-immunogenic, non-toxic, chemically inert and biocompatible (Kiran & Ramakrishna, 2021; Paital & Dahotre, 2008). In addition, they should have high corrosion resistance, good mechanical properties, high hardness, good fatigue performance and good wear resistance.

Metallic materials used in biomedical applications have become critical as the need for implant devices such as dental, orthopedic and cardiovascular implants increases (Saravanan, Hamidon, Murad, & Zailani, 2021; Schweiger, Güth, Erdelt, Edelhoff, & Schubert, 2020). Cobalt chromium molybdenum alloy (CoCrMo) is one of the biomaterials used to manufacture dental and heavy-loaded joints implants (Milošev, 2012; Maina, 2018; Fellah, et al., 2023). Also, it is used in the biomedical industry for hard tissue reconstruction due to its favorable wear, mechanical and biocompatibility properties (Milošev, 2012; Hong, Min, & Kwon, 2016). CoCrMo alloys rarely cause irritation, allergic reactions and sensitization except for individuals allergic to chromium or cobalt (Fellah, et al., 2023; Grosgogeat, Vaicelyte, Gauthier, Janssen, & Le Borgne, 2022). The percentage of individuals allergic to using CoCrMo alloy is low (Sahoo, Das, & Davim, 2019). CoCrMo alloys have a balance between corrosion resistance, biocompatibility and mechanical properties (Wilson J. , 2018). Due to their application in the dental field, surface roughness is an important parameter that affects surface hardness, the adhesion of bacteria on the implant surface, and osseointegration. Thus, the amount of bacteria adherence reduces, and surface hardness improves by decreasing the surface roughness of bio-compatible materials (Yung, Xiao, Choy, Wang, & Cai, 2018; Dank, Aartman, Wismeijer, & Tahmaseb, 2019). Inconsistent surface roughness will lead to varied osseointegration, which may negatively impact the stability of the dental implant (Li J. , et al., 2020).

Despite their success, dental implants are associated with various problems that result in revision surgeries, thus reducing the lifetime of implants (Dejob, et al., 2022). The reasons for revision surgeries include aseptic loosening, bone loss due to the generation of wear particles, and metal ion release (Holt, Murnaghan, Reilly, & Meek, 2007; Gallo, Goodman, Konttinen, & Raska, 2013; Christiansen, et al., 2019). Figure 1.1 shows titanium particles release from the dental implant. Metal ion release due to

corrosion and wear can cause metallosis and cancer (Bandyopadhyay, et al., 2019; Pritchett, 2012). Cancer was linked to Cr^{3+} and Co^{2+} ion release due to biocorrosion and wear of the implants. However, revision surgeries are accompanied by poor clinical outcomes, significant economic effects on the healthcare system and influence the lifespan of the implant (Wang, Ning, & Pei, 2021). Also, dental procedures may expose the implant to bacteria, resulting in implant-associated infections.

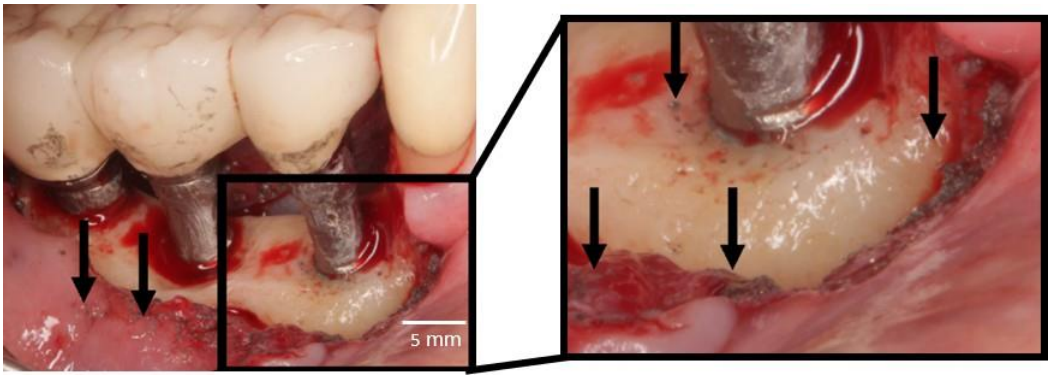

.

Figure 1.1: Particles Release from a Dental Implant

Source: (Suárez-López del Amo, Garaicoa-Pazmiño, Fretwurst, Castilho, & Squarize, 2018)

Fabrication of CoCrMo alloy using conventional manufacturing methods is difficult due to its high hardness and wear resistance (Zaman, et al., 2017). These properties result in shorter tool life and rapid tool wear. Lost wax casting method used in the processing of CoCrMo for dental applications has limitations that include low material utilization rate and poor surface roughness, which results in poor restorations (Wu, Dong, Qu, Yan, & Li, 2022; Konieczny, Szczesio-Wlodarczyk, Sokolowski, & Bociong, 2020). In addition, the cast element usually has pores in its structure which result in poor mechanical properties. The process also involves a lot of manual work, can lead to low accuracy and is time-consuming. Cast CoCrMo alloys have a higher surface roughness after heat treatment than laser-sintered CoCrMo alloys (Kassapidou, et al., 2020). Milling results in a lot of material waste and, therefore, cannot be a suitable method for fabricating the alloy (Konieczny, Szczesio-Wlodarczyk, Sokolowski, & Bociong,

2020). Hot forged CoCrMo alloy requires intermediate annealing before obtaining the final shape (Chandrasekaran, 2019). Forging CoCrMo alloy needs a sophisticated press with heat-resistant tooling. It is difficult for the process to occur at lower temperatures, and hot forging is needed with an intermediate annealing process (Chandrasekaran, 2019). Isothermal forging of CoCrMo alloy requires the use of expensive tooling materials. The poor machinability of the alloy is due to its hardness (Zaman, et al., 2017). The manufacturing process influences the microstructure and properties of CoCrMo alloy. Due to the difficulties in fabrication using conventional methods caused by strain hardening, high material hardness, and increased tool wear, an alternative fabrication method is required. LENS can simplify the fabrication route, allow the manufacture of near-net-shaped implants, and potentially reduce the cost of production.

1.4 Problem Statement

Medical implant devices should have high wear resistance, mechanical strength and low surface roughness for their smooth functioning. The fabrication of CoCrMo alloy using conventional manufacturing methods is difficult due to its high hardness (Abdul Patar, Suhaimi, Sharif, Mohruni, & Kejia, 2024). Also, the fabrication of dental implants is a complex process since they have a complex geometry that varies from patient to patient. Therefore, it is challenging to manufacture medical equipment by applying conventional manufacturing methods. Additive manufacturing is becoming increasingly attractive in the medical field since it helps fabricate customized components to best match the human's tissues and bones. In LENS, selecting optimum process parameters for specific alloys is still challenging. Improper selection of parameters may result in poor surface finish and mechanical properties (Izadi, Farzaneh, Mohammed, Gibson, & Rolfe, 2020; Seshagirirao, Raju, & Mantrala, 2022; Revathi, et al., 2019). In LENS, the input process parameters with the most influence on mechanical properties and microstructure of parts are powder feed rate, laser power and laser scan speed (Zhang, Li, & Liou, Additive manufacturing of cobalt-based alloy on tool steel by directed energy deposition, 2022) . To improve the quality of parts, these parameters should be optimized while other input parameters are kept constant at their optimum levels, as indicated by previous scholars. To potentially reduce costs, save time and resources, mathematical models for predicting surface roughness, microstructure and mechanical properties of

CoCrMo alloy are needed. The mathematical models will correlate the important input parameters for each response. Also, the model will help predict the response and input parameters. Although research on the influence of LENS process parameters has been carried out, little research has been carried out on optimizing LENS process parameters for CoCrMo alloy using response surface methodology (RSM) for dental implant applications.

1.5 Objectives

1.5.1 Main Objective

The main objective is to optimize the LENS processed cobalt-chromium-molybdenum (CoCrMo) alloy through the determination of optimum parameters for improved surface roughness, microstructure, and mechanical properties for dental implant applications.

1.5.2 Specific Objectives

To achieve the main objective, the following were the specific objectives:

i. To experimentally investigate the influence of LENS process parameters on the surface roughness, microstructural characteristics and mechanical properties of CoCrMo alloy.
ii. To develop and validate analytical models for predicting surface roughness, microstructural characteristics, and mechanical properties of CoCrMo alloy.
iii. To optimize the surface roughness, microstructural characteristics and mechanical properties of CoCrMo alloy.

1.6 Research Questions

i. What mathematical models can accurately predict the surface roughness, microstructure, and mechanical properties of CoCrMo alloy?
ii. How do different process parameters influence the surface roughness, microstructure, and mechanical properties of CoCrMo alloy?
iii. What combination of process parameters results in the optimal balance between

surface roughness, microstructural integrity and mechanical properties of CoCrMo alloy?

1.7 Justification

The study was conducted based on the biomedical applications of cobalt-chromium-molybdenum alloy in the manufacturing of dental implants. Its high hardness also makes it difficult to manufacture using conventional methods. Implants should exhibit reliability for long term use and high performance. The reliability for long-term use is influenced by their mechanical properties (Gobbi, et al., 2020). To achieve long-term use of the implants, the LENS process parameters should be optimized for good mechanical properties and surface finish. Also, the selection of the process parameters is a challenging task, which also justified the need to carry out this study. The failure of implants necessitates expensive reconstructive surgeries. The results of this study will guide the selection of optimum process parameters to improve the quality of dental implants. Also, the findings of this study can promote knowledge and skills empowerment.

1.8 Thesis Structure

This thesis comprises five chapters. Chapter one has outlined the essential information on the background of this study, the problem statement, objectives, and justification. The background in this chapter discusses additive manufacturing and its applications in the dental industry. Chapter two entails a literature review on additive manufacturing of CoCrMo and optimization using response surface methodology. Chapter three covers the experimental work completed to investigate the influence of LENS input process parameters on the responses, model development and optimization of the process parameters. Chapter four outlines the result and discussion. Finally, the conclusions and recommendations for further research are outlined in chapter five.

CHAPTER TWO

LITERATURE REVIEW

2.1 Introduction

This chapter describes additive manufacturing techniques, influence of LENS process parameters, defects in additive manufacturing and optimization methods. The different types of biomaterials and a summary of gaps determined by reviewing literature are also presented.

2.2 Additive Manufacturing Techniques

Additive manufacturing (AM) methods allow the efficient use of material and fabrication of components with complex geometry. Presently, additive manufacturing is employed, and research is carried out for applications in fields like the automotive, aerospace, marine, and medical industries (Islam, et al., 2024). Several materials can be used during the AM process, which allows the creation of new products with lower material costs and minimal waste (Wong & Hernandez, 2012). AM allows the customization of devices. Nevertheless, this needs the tracing of the various components compared to the production of the parts in high volumes. Additive Manufacturing technologies are used in dentistry to fabricate devices such as overdentures metal frameworks for removable partial dentures (RPD) and tooth and implant-supported fixed dental prostheses (FDP) (Revilla-León, Meyer, & Özcan, 2019). Further research is necessary to evaluate their clinical result through their function, accuracy, and reproducibility. Technological improvements in the future will enable the broadening of dentistry applications (Revilla-León, Meyer, & Özcan, 2019).

Additive manufacturing components have high porosity, tensile residual stresses, and poor surface finish that accelerate crack initiation. The tensile residual stresses affect the fatigue life of components (Bastola, Jahan, Rangasamy, & Rakurty, 2023). The poor surface finish is due to balling, zones where there is incomplete melting and the staircase effect (Narasimharaju, et al., 2024; Li, Warner, Fatemi, & Phan, 2016; Ye, Zhang, Zhao, & Dong, 2021). The staircase effect is an occurrence where the layer marks are

visible on the surface of components giving the impression of a staircase.

AM methods include powder bed fusion (PBF) and directed energy deposition (DED). The two methods have different powder delivery methods that impact surface roughness of parts, part complexity and flexibility of material usage.

2.3 Powder Bed Fusion

PBF entails the selective melting of powder particles into 3D objects using a heat source focused on particular areas. The different types of PBF methods include selective laser sintering (SLS), selective laser melting (SLM) and electron beam melting (EBM). Figure 2.1 shows the principle of powder bed fusion. The different methods vary by the type of materials used and the amount of light used to transmit energy into the powder bed (Awad, Fina, Goyanes, Gaisford, & Basit, 2020). PBF method requires a high powder volume. It is mostly applicable to smaller and highly complex components. Besides, it is limited to premixed and single-composition powder feedstock. In contrast, DED requires low powder volume and is applicable to large-scale components. Besides, multiple chemistries and compositions are possible to print on the same substrate (Bandyopadhyay, et al., 2022). PBF uses an electron or laser beam to fuse a layer of powder that has been spread on a build-plate surface. After the fusing of one layer, an additional layer is added. This technique is ideal for design scenarios where a lot of powder is presented or the previous work was done using the DED technique (Bandyopadhyay, et al., 2022). Also, large amounts of powder are required when an alloying element is combined with pre-alloyed feedstock atomized from a commercial alloy.

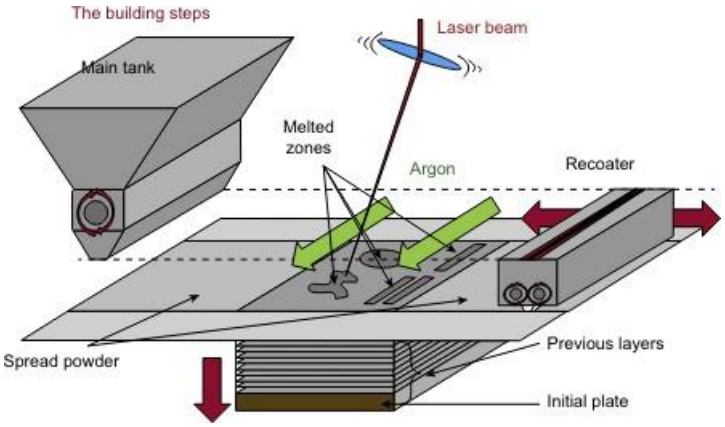

Figure 2.1: Schematic Representation of the PBF Process

Source: (Sun, Brandt, & Easton, 2017).

2.3.1 Selective Laser Melting Process

Selective Laser Melting process (SLM) is an AM technique used to fabricate complex three-dimensional parts by solidifying layers of powder materials based on a 3D CAD model. SLM technology allows the manufacture of difficult geometries that are impossible with conventional methods like forging, extrusion, and casting (Kumar & Prasad, 2021; Riza, Masood, & Wen, 2014). In this method, a high-power-density laser is used in melting powders. The principle of the process commences with a building platform applied with thin layers of powders that are melted completely by thermal energy produced by laser beams. The metal powder is spread across the build plate or substrate in very thin layers by a recoater. A high-power laser beam is focused on the powder bed by a computer-generated pattern by designed scanner optics (Hong, Min, & Kwon, 2016; Karimi, Suryanarayana, Okulov, & Prashanth, 2021). This results in a thin metal layer. The build plate is dropped down by a height that is the same size as one layer. The coating blade spreads another layer of powder across the surface. The powder particles are selectively melted to form a shape of a 3D object according to the computer-aided design. The process is conducted in a controlled atmosphere that contains gases such as argon or nitrogen gas to remove the air that can be present in the chamber. The part is removed from the chamber once the process of building it is complete. The SLM process has the same working principle as the EBM process, whereby it employs layer-by-layer technology to fuse the powder particles by a laser. SLM process can process

various materials like Al-based alloys, Ni-based alloys, Fe-based alloys, Ti-based alloys, Cu-based alloys, Co-based alloys, and their composites (Karimi, Suryanarayana, Okulov, & Prashanth, 2021). The SLM process allows the use of various metals and low-volume production, allowing implementation of any design change, allowing the customization of biomedical devices, increased functionality, and relatively low cost (Munir, Biesiekierski, Wen, & Li, 2020) .

Part delamination (separation of a layer from a substrate) may occur on the powder bed system because of lack of fusion and residual stresses due to the high speeds of the SLM system (Arthur N. K., 2019). This can prevent the building process from proceeding as required. Also, the components fabricated by SLM suffer from the challenge of balling (Liu & Kuttolamadom, 2021; Olakanmi, Cochrane, & Dalgarno, 2015). Balling is a phenomenon where there are spherical particles on the surface of a component. This problem affects the surface roughness of the SLMed components.

2.3.2 Selective Laser Sintering

SLS is a powder-based additive manufacturing process that utilizes thermoplastic polymers as the main feedstock material. Laser energy is used to melt and fuse the powder. The fused powder is then stacked layer by layer to form a printed component based on 3D model data (Konieczny, Szczesio-Wlodarczyk, Sokolowski, & Bociong, 2020; Gan, et al., 2020). SLS can produce large components with excellent mechanical strength at a low-cost (Najmon, Raeisi, & Tovar, 2019).

2.3.3 Electron Beam Melting

Electron beam melting (EBM) utilizes an electron beam to melt metal powder layers. The main feed material is metal powders. EBM is ideal for the manufacture of lightweight, dense and durable parts. This technique operates under the principle of developing structures by melting powder layers by an electron beam in a vacuum condition (Singh, Singh, & Hashmi, 2016). The vacuum environment prevents oxidation and contamination of the powder and final component in the manufacturing process (Mehrpouya, et al., 2022). The limitations of EBM include its parts have low accuracy compared to SLM components. This is because the SLM printers use finer powders.

Also, the choice of materials for the EBM process is limited since the process requires expensive and high-quality materials. The cost of EBM 3D printers and that of materials makes this method an expensive option. CoCrMo alloys fabricated by EBM exhibit anisotropic behavior and are brittle. For these reasons, the part must undergo solution annealing and aging (Xiang, et al., 2019).

2.4 Directed Energy Deposition

DED is an AM process that adds material (frequently used for metals like aluminium, titanium, cobalt chromium or stainless steel) alongside the heat input simultaneously (Piscopo & Iuliano, 2022; Raghupatruni & Kumar, 2023). The heat input can be an electron beam, laser or plasma arc. The material feedstock is either wire or metal powder. This technique is used for rapid prototyping, repair, and low-volume part fabrication. The powder deposition occurs in a vacuum or under inert gas (laser or arc systems). The properties and qualities of parts fabricated by DED are determined by the build environment (ambient, inner gas or vacuum), type of DED technique, deposition parameters and beam-material interactions. The high thermal gradients and fast cooling rates result in defects such as cracking and delamination, premature failure, high surface roughness, porosity, non-uniform residual stresses and microstructural changes. Figure 2.2 presents a schematic of the DED process. Svetlizky et al. (2021) recommended process optimization to mitigate these defects. The DED processes include Laser Engineered Net Shaping (LENS) and laser cladding (LC).

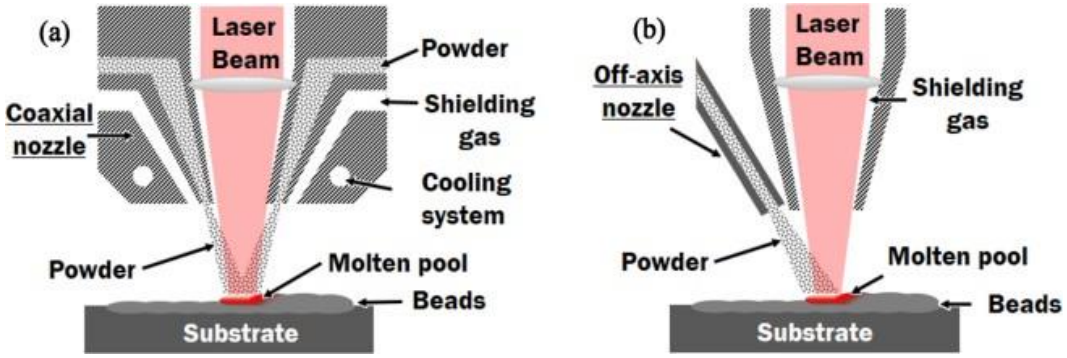

Figure 2.2: Principle of the DED Process

Source: (Ahn, 2021).

2.4.1 Laser Cladding

Laser cladding utilizes a high power laser to form a cladding layer on a substrate. It is possible to mix two or more types of powder and control the powder feed rate of each powder flow in this process and therefore suitable for fabricating functionally graded materials. Laser cladding is used for strengthening and surface repair of components (Zhang, et al., 2023). The commonly used laser cladding methods include pre-placed powder system and coaxial powder system (Zhu, et al., 2021). Figure 2.3 is a schematic representation of the coaxial powder system and preplaced powder system. In the coaxial powder system, the powder is supplied directly into the laser beam. The cladding process and powder feeding are completed simultaneously with the shielding gas (Liu, et al., 2021). In contrary, for the pre-placed powder technique, the cladding material is pre-placed on the substrate followed by melting by the laser beam.

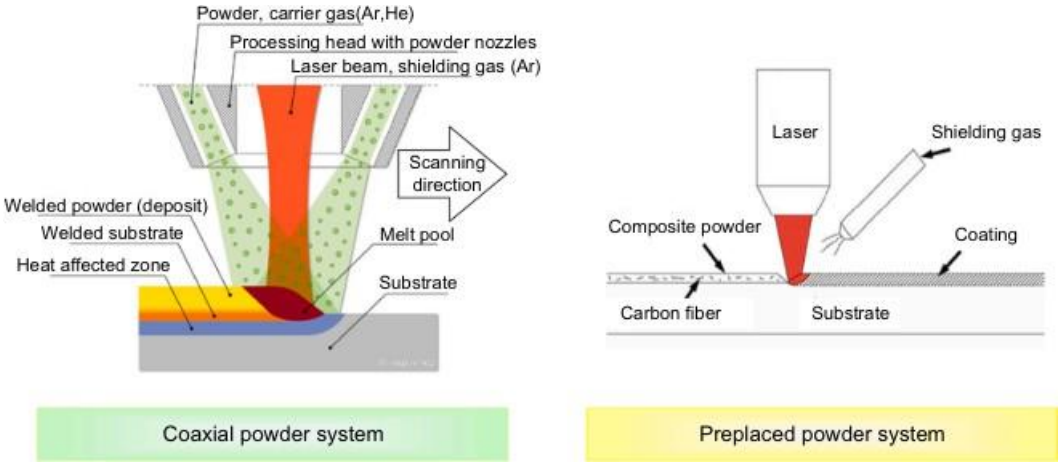

Figure 2.3: Schematic Representation of the Coaxial Powder System and Preplaced Powder System

Source: (Zhu, et al., 2021).

2.4.2 Laser Engineered Net Shaping (LENS)

The LENS technique was developed to produce complex geometrical parts. Also, it can be used to fabricate difficult-to-cut materials. In this method, the powder is blown through nozzles which are coaxial with the laser head into a melt pool on a substrate. The deposited material is melted upon deposition with an electron beam or laser to

make a deposited line. The powder is melted while powder material is added to the molten pool. Several lines are added to make a layer. The process is repeated till a complete part is formed. In this process, the nozzle can move in different directions and is not fixed to a particular axis. Figure 2.4 shows a schematic representation of LENS. Two or three-axis systems have a static plate which allows the nozzle to move up once a layer is deposited. For the four-axis or five-axis systems, the base and the nozzle are run simultaneously.

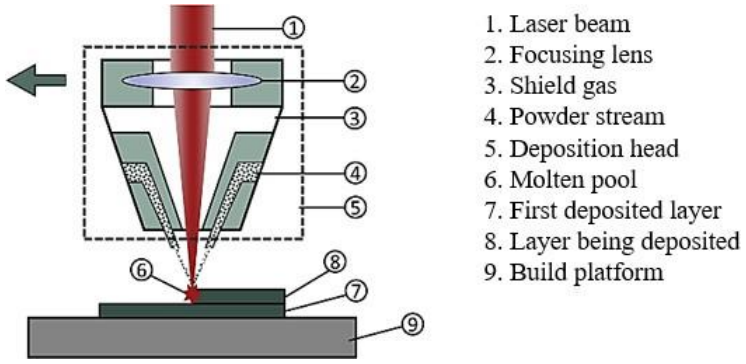

Figure 2.4: Schematic Representation of Laser Engineered Net Shaping Process

Source: (Aramian, Razavi, Sadeghian, & Berto, 2020).

In this study, LENS was selected due to the challenges experienced on the powder bed system. LENS was selected due to its improved laser-material interaction times and slower speeds. However, the LENS components have a rougher surface compared to the SLM process due to the large particle size and spot size used. Nunez et al. (2024) obtained surface roughness values of the range 3.21 μm - 42.91 μm for IN718 fabricated via LENS. Therefore, further studies should be conducted to lower the surface roughness.

2.5 Influence of LENS Process Parameters

The important process parameters include laser power (P), powder feed rate, scan speed (v), hatch spacing (h), layer thickness (t) and laser spot size (d). The parameters are unified by the following energy density (E_D) equation 2.1 (Jeong, et al., 2022):

$$E_D = \frac{P}{v \times d} \tag{2.1}$$

where E_D is the energy density (J/mm^2), v is the scanning speed (mm/s), P is the laser power (W) and d is the laser spot size (mm). Laser power is used to liquefy the powder to form a melt-pool which solidifies to form a layer. Laser power influences the mechanical properties of a component. An increase in laser power results in an increase in the width of the melt pool. When a dense component is required, the laser power should be increased to avoid porous structures (partial melting zones) but doing so has an impact on the microstructural properties (Chen, et al., 2024). An increase in laser power reduces the hardness since, in some cases, the grain size increases. Also, an increase in laser power can result in an increase in residual stresses.

The scanning speed relates to the mass flow rate and the laser power. For instance, a low mass flow rate should be compensated with a low scanning speed. A high scanning speed with a low mass flow rate will result in the fabrication of a part with inadequate material to accomplish the dimensional requirements. A high mass flow rate and a low scanning speed will result in oversized beads. Increasing the scanning speed reduces the energy density (Hao, et al., 2023). Also, when the scanning speed is increased, it will result in a higher cooling rate. The powder feed rate or mass flow rate involves the volume and speed of the powder added to the melt pool. Changing the powder feed rate will influence the mechanical properties. The melt pool will be cooled by excessive powder to a point where most of the metal will not be fused. Thicker layers will be built when the feed rate is high resulting in part non-uniformities. When the feed rate is low, there may be inadequate powder to fill the gaps between the lines resulting in porous zones. The feed rate is optimized by the operator running the feed system to determine the average powder feed rate in grams per minute.

The dimensional accuracy of parts fabricated by LENS is still a challenge and there is no clear protocol to achieve satisfactory build outcomes when manufacturing complex geometry components (Piscopo, Salmi, & Atzeni, 2024). The build accuracy depends on the optimization of the process parameters for a particular powder to fabricate a component at the desired layer height. Also, to resolve the build irregularities,

additional time is required for post-processing. Izadi et al. (2020) reviewed the LENS process parameters of metallic components. The process parameters and their optimization play an essential role in the effectiveness of LENS, and research should be done to optimize them for a high degree of repeatability. The authors concluded that future studies should focus on examining various process parameters other than laser power, scan speeds and power feed rates. Besides, studies should be conducted on the influence of process parameters on geometrical accuracy and the development of mathematical models that reflect the build process.

Oliveira et al. (2019) studied the fabrication of dental implants using AM. Based on the findings of the review, they concluded that AM is an effective alternative to conventional methods for the fabrication of custom dental implants. Also, AM of implants has advantages such as flexibility, customization, the possibility of manipulating physical and chemical parameters and freedom in implant design. However, AM has limitations when used to manufacture implants that include dimensional accuracy, obtaining surface quality and cost of equipment and materials (Oliveira & Reis, 2019). The study confirmed that further studies should be conducted to improve the method for fabricating custom implants.

Liu et al. (2021) fabricated CoCrMo samples using DED technique at various powder feed rates and laser powers. Liu characterized the samples to ascertain their mechanical and microstructural properties. The aim of the study was to comprehend how altering the composition of CoCrMo can lead to specific micro and macro structures that impact the depth-based hardness and modulus. Spectroscopy and high-resolution microscopy indicated the availability of networked and jagged carbides with different amounts of Mo. γ and ϵ phases were confirmed using X-ray Diffraction (XRD). Nano and micro-scale characterization of the alloy manufactured at different process conditions indicated material properties that were the same as those produced by casting. However, this study did not include the influence of scanning speed.

Wo-losz et al. (2020) studied the influence of Laser Engineered Net Shaping (LENS) parameters on the properties of H13 (AISI) steel. The parameters that were varied

during this experiment include powder flow rate, laser spot diameter and deposition velocity. The efficiency of the cladding varied significantly with the change in parameters. The selected parameters affected the size of the heat-affected zone, the shape of the clad, and the hardness and microstructure of the steel. The hardness of the steel ranged between 500 - 800 HV after deposition. The choice of the parameters resulted in the desired surface hardness of the material.

Łazińska et al. (2018) studied the effect of the traverse feed rate on the mechanical and microstructure properties of laser-deposited Fe3Al (Zr, B) Intermetallic Alloy. Based on the results, the LENS method allows for the shaping of the material microstructure through the appropriate selection of the process parameters that affect the rate of heat transfer. Also, the results indicate that the LENS method allows the control of the morphology of structural parts. The authors found that the working table feed influences the porosity of the components, whereas an increase in speed results in an increase in the degree of porosity. In addition, cracks were observed in the specimen for a feed rate that was greater than 20 mms^{-1}. The yield strength and microhardness of the samples were not affected by the working table feed.

Suresh et al. (2019) fabricated CoCrW samples to identify the suitable parameters for optimum wear, hardness and corrosion resistance to the LENS deposited samples. The authors used the Taguchi method to design the experiments and Grey Relational Grade Analysis (GRGA) method and ANOVA to analyze the results. The authors concluded that the properties of corrosion, wear resistance and hardness are influenced by the process parameters. The optimum parameters were a powder feed rate of 7.5 $gmin^{-1}$, a laser power of 350 W, and a scan speed of 20 mms^{-1}. However, the study did not include the influence of these process parameters on the surface roughness in correlation with the other mechanical properties studied.

Kistler et al. (2019) studied the influence of process parameters on the porosity, microstructure and mechanical properties of Ti-6Al-4V repair manufactured by DED. The researchers used design of experiments to study the influence of interlayer dwell

time, substrate thickness, hatch pattern, initial substrate temperature, hardness of the deposition, porosity and number of deposited layers on the microstructure. The variation of the process parameters illustrated how each collectively or independently affects the resulting properties and microstructure of Ti-6Al-4V deposits. The results indicated that the density of the part was influenced by the number of deposited layers. Also, the hardness increased due to the increase in the thickness of the substrate.

Wei et al. (2015) conducted a study on the SLM-forming process of CoCr alloy. Wei analyzed the microstructure of components and the effects of the process parameters like scan space, scan speed, laser power, and laser energy density on the hardness of the alloy, relative density, and surface roughness. The results indicated that different scanning speeds, laser power, and scan spacing lead to different surface roughness, even though the energy density remained the same. The relative density of the alloy increased as the laser power increased (Wei, Tingting, Wenhe, & Liyi, 2015).

Maamoun et al. (2018) investigated the influence of SLM process parameters on the dimensional accuracy, surface roughness and density of alloy parts. The materials used in this study are Al6061 and AISi10Mg alloys. The authors established that surface roughness reduced with an increase in the laser power. Further, they found that surface roughness increased with increased scan speed.

Baciu et. (2021) investigated the surface of 3D Co-Cr-W material for dental applications. The process parameters used include a laser power of 70 W, scanning rate of 1000 mms^{-1} and exposure time of 20 μs. The authors found that after the 3D printing process, the components had semi-melted particles that increased the contact surface of the elements. Blasting media was used to clean the alloy surface and modified the surface roughness of the part to achieve the medical application requirements. The components with a layer thickness of 50 μm had a higher roughness than those with a layer thickness of 25 μm. The authors also recommended further research and medical tests to confirm the implications of surface preparation.

Pupo et al. (2015) conducted a study on the effects of process parameters on the surface

quality of CoCrMo produced by SLM. The authors used a full factorial design to evaluate the effect of process parameters on flatness, surface roughness and surface quality. Pupo used laser power of 200 W, 400 W and 100 W and scanning space of 450 μm, 750 μm and 150 μm. Also, the authors used a scanning speed of 50 mms^{-1} and kept it constant. It was observed that surface roughness is influenced by scan spacing, laser power and scanning speed. The researchers found the optimum parameters for the lowest roughness were a laser power of 400 W and a scanning space of 450 μm. The optimum surface roughness determined was 8 μm.

2.6 Defects in Additive Manufacturing

Additive manufactured components show defects that arise due to the use of process parameters that are not optimized (Bellini, et al., 2021). The defects can potentially result in the failure of parts and therefore, it is critical to constantly minimize defects and improve processes. These defects include lack of fusion, porosity and surface roughness variations.

2.6.1 Lack of Fusion and Porosity Defects

Porosity in an additively manufactured component can either be intentionally designed pore structures for special applications or undesirable defects that can contribute to the failure of the component (Kim, Kim, & Moylan, 2018). Characterization of both types of porosity is vital to determine the mechanical characteristics of a component. In this research, the defect type of porosity was considered. Each pore present in a part indicates a possible point for the formation of cracks. As shown in Figure 2.5 porosity is classified as gas porosity and keyhole porosity (Bellini, et al., 2021).

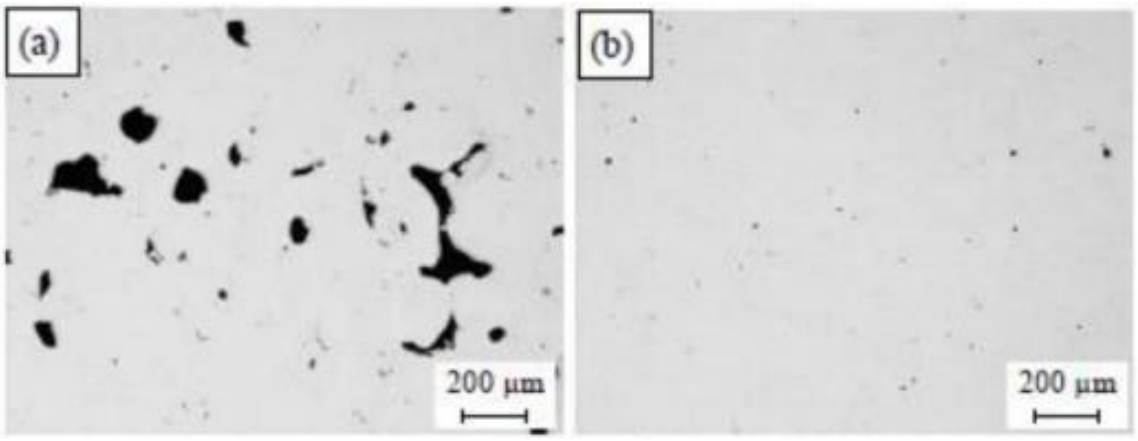

Figure 2.5: Porosity Observed in A Sample: a) Keyhole Porosity; b) Gas Porosity

Source: (Bellini, et al., 2021).

Gas pores are spherical pores that are caused by the gas trapped in the raw powder or the trapped inert gas during melting. Keyhole pores have an irregular shape and are due to insufficient energy density imparted into the melt pool (Bellini, et al., 2021). Lack of fusion (LOF) is the inadequate fusion and melting of the new layer with the preexisting layer. LOF is characterized by large, irregularly shaped pores detrimental to a component's mechanical performance. LOF defects are due to the selection of inappropriate process parameters (Kim, Kim, & Moylan, 2018). Figure 2.6 presents lack of fusion defects. Unmelted powder particles are always present, as shown in Figure 2.6. The presence of unmelted powder particles will result in a decrease in the strength of a part Therefore, proper selection of process parameters can help reduce the porosity of AM parts (Kasperovich, Haubrich, Gussone, & Requena, 2016).

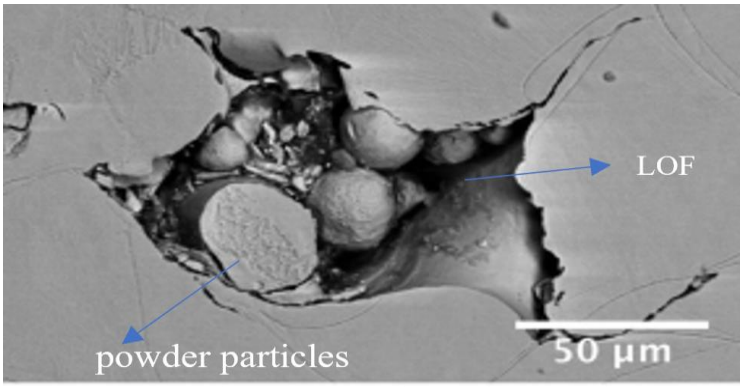

Figure 2.6: SEM micrograph Showing Lack of Fusion

Source: (Tonelli, Fortunato, & Ceschini, 2020).

Tonelli et al. (2020) studied the influence of laser energy density on hardness, surface morphology and microstructure of CoCr alloy fabricated by SLM. The study focused on the correlation between laser energy density (LED) and the responses with the aim of obtaining optimum LED to improve the quality of parts. Tonelli found that LED greater than 200 J mm^{-3} will result in the collapsing of the keyholes. In addition, the authors found that low LED was inadequate to melt the powder completely.

An et al. (2018) conducted a study on pore defect and density of CoCr alloy fabricated by SLM. The authors found that powder thickness is the most influential process parameter on the density of SLM fabricated components. Further, the authors demonstrated that selecting appropriate process parameters minimizes pore formation. The authors also recommended preheating the powder and substrate to discharge gases to reduce the occurrence of gas porosity.

2.6.2 Surface Roughness Variations

Surface roughness is one of the most influential defects that influences crack initiation behavior and can increase the local stress concentrations (Ma, et al., 2023). It is well understood that the ideal surface roughness (Ra) for cell adhesion is 2 µm (Kunrath, 2020). Studies indicate that minimizing surface roughness in AM components will improve their fatigue resistance (Yadollahi, Mahtabi, Khalili, Doude, & Newman Jr, 2018). Surface roughness is due to the stair-step effect, balling phenomenon, and

insufficient melting of the powder particles (Gülcan, Günaydın, Çelik, & Yasa, 2024). The top surface roughness of a part fabricated by LENS is susceptible to the presence of unmelted powder particles during the deposition process. Optimization of the interaction of process conditions and parameters and post-fabrication surface treatment methods can help minimize the surface roughness. Zheng et al. (2019) studied the defect control and microstructure of 316L SS parts manufactured via directed energy deposition. The top surfaces of the components had alternating layered ridges and partially melted particles, which contributed to the high surface roughness of the samples.

2.7 Overview of Dental Implants

The survival and success of dental implants is determined by their mechanical and biological properties. The biological perspective entails implant toxicity and proper osseointegration. Successful osseointegration is determined by implant design, implant material, surface finish and status of the bone (Wang, et al., 2023). The surface properties of the implant are based on roughness, surface morphology and surface elements. The mechanical properties include the chance of loosening, implant strength and fracture probability. The selection of appropriate fabrication techniques, utilization of proper process parameters and utilization of suitable materials is necessary to improve the performance of dental implants. Understanding the mechanisms and reasons behind tooth wear is necessary for developing functional dental implants. Dental wear is caused by overbite, underbite and regular mastication force. The essential factor in wear analysis is the occlusal load. The load varies from one individual to another.

Different wear mechanisms include corrosion wear, fatigue wear, adhesive wear and abrasive wear. The most common type of wear observed in human teeth is abrasive wear. Abrasive wear is divided into two-body and three-body abrasion. Two-body abrasion occurs when two surfaces are in contact with each other. The parameters that affect this type of wear include sliding speed, sliding distance and contact angle. Three-body abrasion initiates when two bodies slide along each other with an external particle interposing between them (Saha & Roy, 2023). Adhesive wear occurs when two bodies slide against each other in the presence of pressure in the mouth. Fatigue wear initiates when

a surface is subjected to movement under cycling loading and high pressure. Corrosion wear entails the loss or removal of dental molecules in the presence of a chemical effect (Souza, et al., 2015).

2.8 Dental Implant Materials

The material used to manufacture dental implants is essential in offering ideal properties such as preventing inflammation around the dental implant. Therefore, the selection of appropriate implant materials is critical to prevent inflammatory conditions and improve treatment outcomes (Haugen & Chen, 2022). Implant materials are discussed in the following sections.

2.8.1 Magnesium and its Alloys

Magnesium and its alloys have an elastic modulus that is closer to that of the natural bone (Radha & Sreekanth, 2017). The use of this alloy will not result in the stress shielding effect. Also, magnesium implants stimulate the formation of a new bone when used as bone fixtures. However, the application of this alloy is still inhibited due to its fast degradation rate, leading to the release of hydrogen gas during the first few weeks after the surgery is conducted. The gas accumulates in the surrounding tissues. Therefore, the release of hydrogen and the faster corrosion rate is a major concern. The degradation rate can be controlled by surface modification technology and adding alloying elements (He, Chen, Yin, Xu, & Liang, 2023). The alloying elements can help improve the mechanical, chemical and physical properties of magnesium.

2.8.2 Titanium and Its Alloys

Titanium alloys have high durability and greater biocompatibility. Compared to CoCrMo alloys and stainless steel, titanium alloys have a lower elastic modulus, lowering the stress shielding effect (Hernandez-Rodriguez, et al., 2019). The stress-shielding effect arises as a result of shear stresses due to the variation of material properties between the implant and the bone. Nevertheless, titanium implants have a lower wear resistance than CoCrMo alloys, resulting in corrosion pits on the implant surfaces (Abdulwahab, Enechukwu, Aigbodion, & Yaro, 2015). Also, the dissolution

of vanadium and dissolution ions may be toxic to the host tissue (Saha & Roy, 2023; Kumar, Devi, Krithika, & Raghavan, 2020). The development of martensite in the microstructure of AM Ti-6Al-4V parts decreases their corrosion resistance and fatigue life (Pothala & Raju, 2023). Therefore, it is necessary to identify alternative titanium alloys to overcome these limitations.

2.8.3 Stainless Steel and Its Alloys

Stainless steel has low corrosion resistance compared to cobalt and titanium-based alloys. The use of stainless steel may result in allergic reactions due to wear debris. The biocompatibility of stainless steel is less satisfactory than that of titanium and cobalt-chromium alloys due to the higher degradation rates (Gobbi, et al., 2020). Therefore, this material can only be used in temporary implants.

2.8.4 Nitinol Alloys

Nitinol (nickel-titanium) alloys have tuneable stiffness and low elastic modulus. These alloys have elastic behavior that is close to the bone. In addition, they are medically safe since their cytocompatibility is comparable to that of CoCrMo alloys, stainless steel alloys and titanium alloys.

2.8.5 Cobalt Chromium Molybdenum (CoCrMo) Alloy

Cobalt chromium molybdenum alloy has gained popularity as a crucial biomaterial fabricated by additive manufacturing. The CoCrMo parts manufactured by additive manufacturing have better mechanical properties compared to the conventional cast parts (Hong & Yeoh, 2020). The alloy is an attractive material for applications in several fields such as medical, nuclear, and aerospace (Zaman, et al., 2017). It has excellent characteristics like high wear resistance, corrosion resistance, creep resistance, and good biocompatibility. The grain size of the alloy is reduced due to the presence of molybdenum in the alloy, thus improving the mechanical properties of the alloy (Zaman, et al., 2017). CoCrMo has excellent bonding characteristics with porcelain and excellent physical properties. In addition, it is stable in the body (Barazanchi, Li, Al-Amleh, Lyons, & Waddell, 2017). The chromium particles in the alloy improve its corrosion resistance

by forming a layer that protects the surface. These characteristics make the alloy suitable for applications under mechanical stress. When implants wear, large debris is released. This will result in a foreign body reaction and implant loosening. Owing to its excellent properties, CoCrMo alloy is used for making dental and orthopedic implants (Minnath, 2018). The properties of CoCrMo alloy are shown in Table 2.1.

CoCrMo alloy orthopedic prostheses are for shoulder, knee, and hip replacements and fixation components for fractured bones. The weight of CoCrMo alloy fabricated dental restorations is light due to its low density. Other applications of CoCrMo alloy include implants like acetabular cups, heart valve cages, tribial trays and cardiovascular stents.

Table 2.1: Properties of CoCrMo Alloy

Mechanical properties	Value	Unit
Young Modulus	235-247	GPa
Tensile strength	1290-1420	MPa
Hardness	363-402	HV
Elongation	25-29	%
Yield strength (elastic limit)	760-839	MPa

Konieczny et al. (2020) reviewed the challenges of CoCr alloy AM methods in dentistry. The authors noted that additive manufacturing processes have allowed the fabrication of complex components tailored to a particular patient. Also, they noted that surface finishing of build parts is essential.

Zhou et al. (2018) conducted a comparative analysis of the mechanical and microstructure properties of CoCr dental alloys manufactured by selective laser melting technique, casting and computer numerical control (CNC) milling. The microhardness and strength of the SLM specimens were higher than that of cast and CNC specimens. Yung et al. (2018) investigated the laser polishing of SLMed CoCr alloy specimens with complex surface geometry. The results of the study include the surface roughness of the polished specimen was improved by 8%. Therefore, it is necessary to optimize process parameters to improve the surface roughness of additively manufactured parts for dental applications to address the issue of postprocessing. Yan et al. (2022) reviewed biomedical alloys and surface modifications. The researchers concluded that more efforts are necessary to develop physical surface modifications on biomedical alloys for biomedical

applications.

Evans et al. (2021) investigated the variations in surface roughness of parts fabricated by Laser Powder Bed Fusion (LPBF). The authors found that surfaces fabricated by LPBF have higher roughness compared to those fabricated by conventional manufacturing processes. The researchers used a limited number of samples, and therefore, additional research is vital to determine optimum surface roughness to ensure the manufacture of quality parts.

Hashmi et al. (2022) reviewed the surface characteristics improvement techniques for metal AM parts. AM technique has the capacity to manufacture 3D parts with complex geometries, but the parts have defects such as poor fatigue life and increased surface roughness. The defects that contribute to an increase in surface roughness include surface pores that are a result of the use of a high scanning speed and molten powders on the surfaces of parts. Hashmi recommended that multi-scale post-processing methods be developed to finish a part from macro to microscale. Also, standardization of postprocessing methods is vital.

Acharya et al. (2021) reviewed the AM of CoCr alloys for biomedical applications. The researchers found that there are significant gaps in knowledge of vital issues such as the role of post-processing treatments and the role of process parameters. The authors concluded that the characterization of wear, fatigue and corrosion performance of CoCrMo alloy parts for biomedical applications has not been exhausted.

2.9 Techniques for Optimizing Process Parameters

Manufacturing optimization is vital to saving costs and increasing productivity. The traditional method of optimization involved observing the influence of one parameter on the response while the other parameters were kept constant (Weremfo, Abassah-Oppong, Adulley, Dabie, & Seidu-Larry, 2022). Nevertheless, this strategy does not examine the interactive effects among variables which results in the incomplete comprehension of the process behavior. Besides, several experiments are needed and this makes it costly and time-consuming. Optimization can be achieved by techniques such as response surface methodology and Taguchi method.

2.9.1 Response Surface Methodology

Response surface methodology (RSM) entails a series of statistical or mathematical methods for the empirical building and exploitation of a model. The technique seeks to relate a response to the input variables that influence it (Thomareis & Dimitreli, 2022; Yong, et al., 2023). Also, it can be used in the prediction and explanation of the relationship between input variables with the responses. The technique can be used to predict the response, detect a lack of fit, identify the outlier data, and make decision-making possible. The application of this method in the design of experiments is aimed at reducing the cost incurred when methods such as the finite element method are used. The steps of applying RSM can be outlined using Figure 2.7.

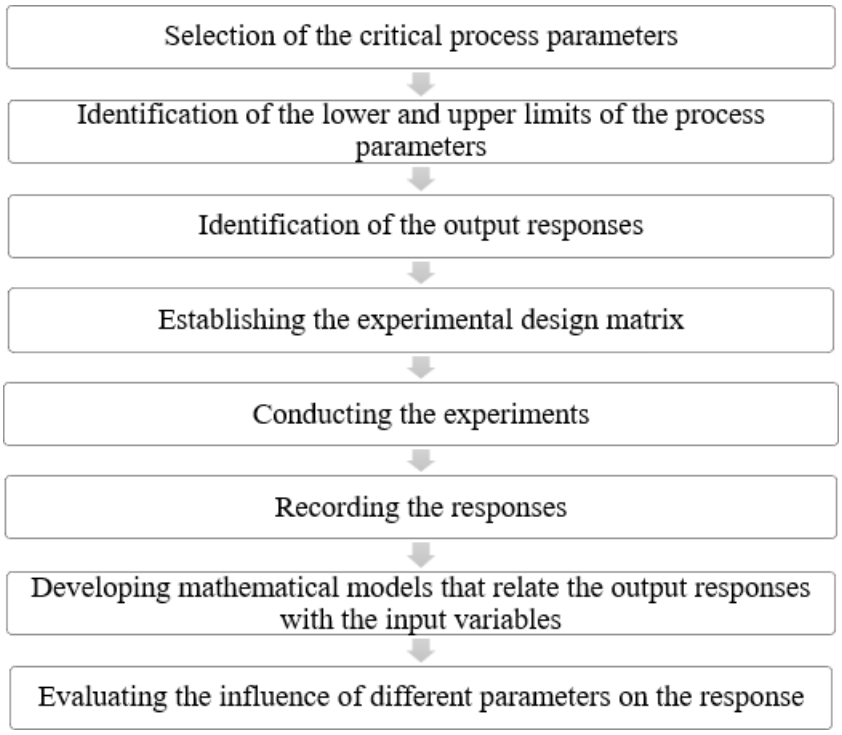

Figure 2.7: Steps of RSM.

The objective of RSM is to optimize a response by design of experiments. The responses are represented graphically as contour plots and in three-dimensional space that assists in visualizing the shape of the response surface. The contour plots show the regions where a response indicates the same magnitude and the optimum level for the factors. On analysis by multiple regression, an equation is produced, which can be used to

plot the response surface as shown in equation 2.2.

$$y = f(x_1, x_2) + \epsilon \tag{2.2}$$

where x_1 and x_2 are independent variables and ϵ represents the error. Figure 2.8a shows a contour plot while Figure 2.8b shows a response surface plot.

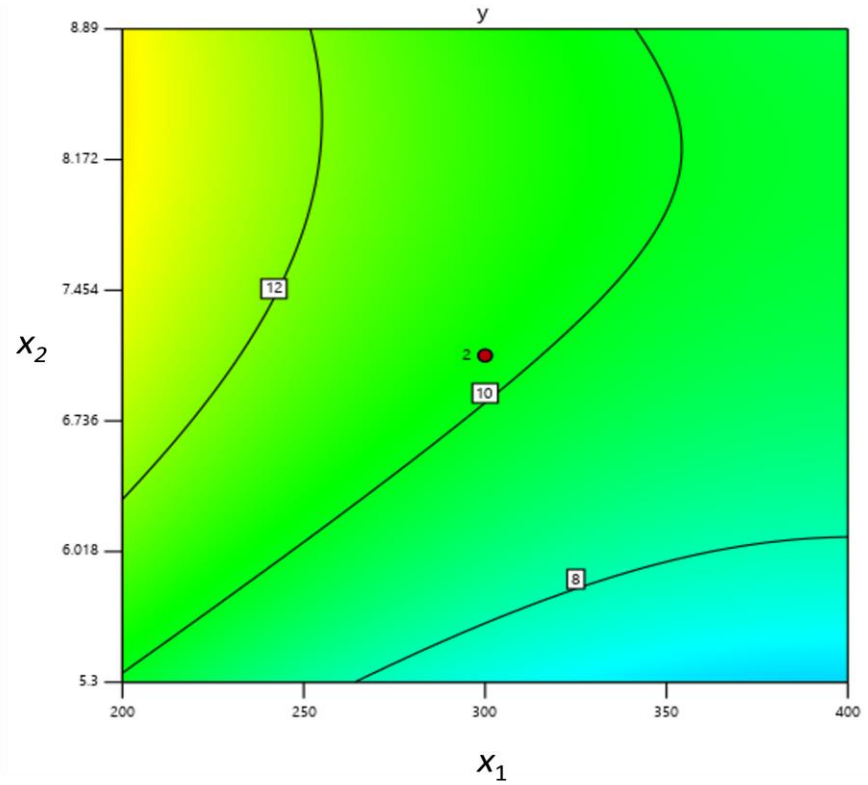

(a) Contour plot

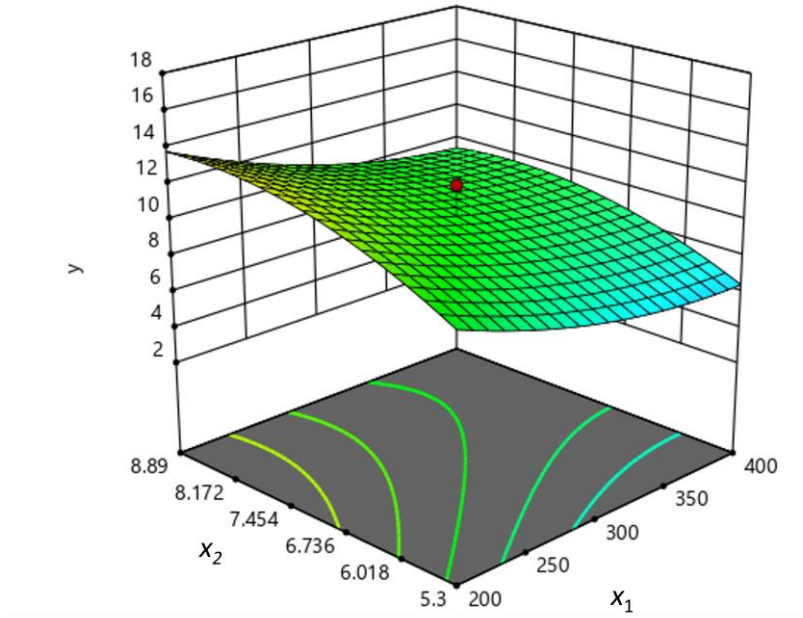

(b) Surface plot

Figure 2.8: Contour Plot and Surface Plot of a Response Surface

To approximate the true response function f, the investigator should begin with a low-order polynomial in a small region. If a linear function defines the response, the approximating function will become a first-order model. The elementary model for RSM can be expressed by equation 2.3:

$$y = \beta_0 + \sum_{i=1}^{k} \beta_i x_i + \sum_{i=1}^{k} + \epsilon \qquad (2.3)$$

The introduction of curvature into the response function necessitates the need for a second-order model as expressed in equation 2.4 (Asiltürk, Neşeli, & Ince, 2016):

$$y = \beta_0 + \sum_{i=1}^{k} \beta_i x_i + \sum_{i=1}^{k} \beta_{ii} x_i^2 + \sum_i \sum_{i=1}^{k} \beta_{ij} x_i x_j + \epsilon \qquad (2.4)$$

where ϵ represents the error, β_0 is a constant, β_i constitute of first order coefficients, βii constitute of second order coefficients and $\beta_{i\,j}$ consists of interaction coefficients and x_j and x_i are the coded independent variables.

The fitted model is assessed by the application of analysis of variance (ANOVA).

ANOVA compares the discrepancy shown by the model with the discrepancy of model residuals. The predictive efficiency of a model is evaluated by the application of the coefficient of determination (R^2) that measures the variation of the predicted values from the mean. The R^2 value ranges from 0 to 1. Therefore, for a good prediction efficiency of a model, the value should be close to 1. Any inclusion of a new term to the model will result in the increase of the value of R^2 (Amirov & Vakhshouri, 2020). Therefore, the adjusted R^2 value must also be determined. The adjusted R^2 value decreases when an insignificant variable is added. The inclusion of non-significant variables in the model will result in adjusted R^2 and R^2 varying intensely. Predicted R^2 assists in predicting new observations on the response and also prevents model overfitting. Residual plots can also be used to verify the adequacy of the model. For an adequate model, the points of the normal probability plot of the residuals form a straight line. Also, the points should be randomly scattered on the plots of predicted response values versus residuals. The F-test can be used to verify the interactions and significance of the variables. The larger the F-value (P>F), the more significant the individual coefficients and the corresponding model. P>F value that is less than 0.05 indicates that the model is significant at the 95 % confidence interval (Weremfo, Abassah-Oppong, Adulley, Dabie, & Seidu-Larry, 2022). Lack of fit can also be used to verify the significance of the model. A desired model is when the lack of fit is insignificant for the selected confidence level ($\alpha = 0.05$) (Weremfo, Abassah-Oppong, Adulley, Dabie, & Seidu-Larry, 2022).

Saidi et al. (2019) modelled and optimized the turning parameters of cobalt alloy based on response surface methodology and desirability function. Saidi adopted an experimental study based on the design of the experiments. The authors established predictive models involving the evolutions of arithmetic mean roughness, material removal rate, tangential force, and cutting power. Saidi used analysis of variance to identify significant cutting parameters influencing surface roughness, material removal rate, tangential force, and cutting power evolutions. The authors used the Pareto technique to confirm the ANOVA results.

Yang et al. (2017) adopted RSM to predict the optimum surface roughness for titanium

alloy. The researchers developed a model and analyzed the effects of cutting parameters on surface roughness. The cutting feed was identified as the parameter with the greatest effect on surface roughness.

2.9.2 Taguchi Method

The Taguchi method is also one of the experimental methodologies used to investigate the minimum number of experiments to be conducted within the allowed limit of levels and factors (Kilickap, 2010). The method helps investigate how parameters affect the variance and mean of a process performance characteristic that defines the functioning of a process. The experimental design entails using orthogonal arrays to organize the parameters that influence the process and the levels at which they vary. Taguchi method emphasizes the control and study of product variability (Lin, Qiu, Zhou, & Chen, 2020; Patel, Parihar, & Makwana, 2021). Also, pairs of combinations are tested. Therefore, the method enables the collection of vital data to identify the factors that have the most influence on product quality with a minimum number of experiments, hence saving time and resources (Sheshadri, et al., 2021). However, the results obtained using this method do not exactly specify what process parameter is the most influencing factor on the response (Sayed, Dawood, Elsayed, & Daoush, 2017).

2.10 Summary of Research Gaps

This chapter has introduced a literature review on different biomaterials, including cobalt-chromium-molybdenum alloys and their applications, the working principle of LENS, influence and optimization of the LENS process parameters. The review has shown that research work on cobalt-chromium-molybdenum alloy is gaining interest, and considerable progress has been made. Each LENS process parameter has an influence on the quality of the part. Literature on various optimization techniques indicates that response surface methodology is desirable in industrial applications since it allows the determination of the interaction between variables, models the system mathematically and saves cost and time by minimizing the experiments.

From the literature review, the following gaps were identified:

i. From the literature, it has been observed that CoCrMo alloy has excellent characteristics for its application in the medical field. Nevertheless, most studies have focused on the fabrication of the alloy using methods such as lost wax casting and powder bed fusion processes such as selective laser melting, with limited research being conducted for the fabrication of CoCrMo alloy using LENS.

ii. Studies on the influence of laser-engineered net shaping process parameters on the qualities of parts using different design of experiment methods has not been exhausted. There is limited research in integrating response surface methodology to assess the effect of LENS parameters on the qualities of parts.

iii. Although the optimization of some biomaterials, such as titanium alloy, has been carried out, there is limited research on the optimization of LENS process parameters for the manufacture of CoCrMo alloy for dental implants.

iv. Several methods exist for predicting surface roughness, microstructure and mechanical properties of CoCrMo alloy. Response surface methodology can be used to optimize LENS process parameters and develop prediction models. There are limited prediction models for surface roughness, microstructure and mechanical properties of CoCrMo alloy for dental implants.

This research addressed the knowledge gaps stated above.

CHAPTER THREE

METHODOLOGY

This chapter outlines the procedures used in the study to meet the set objectives. The description of materials, experimental equipment, and process parameters used are presented. The sample preparation techniques are discussed together with various characterisation techniques. Also, this chapter describes the design of experiments and optimization using response surface methodology (RSM).

3.1 Materials

The experiments involved the optimization of Laser Engineered Net Shaping (LENS) process parameters to fabricate Cobalt-Chromium-Molybdenum alloy for dental implants. The material used in this work was gas-atomized Cobalt-Chromium-Molybdenum (CoCrMo) alloy powder supplied by Weartech Pty (Ltd), South Africa, with the chemical compositions displayed in Table 3.1.

Table 3.1: Chemical Composition of Cobalt-Chromium-Molybdenum alloy (wt%) as Verified by Electron Dispersive Spectrum (EDS).

Si	C	N	O	Co	Cr	Mn	Mo	Fe	S
0.85	2.66	<0.01	1.93	62.61	26.96	<0.1	4.20	0.38	0.30

Most of the CoCrMo powder particle size was +45 μm/-90 μm as per the design specifications of the LENS machine and was confirmed using the Scanning Electron Microscope (SEM). Figure 3.1 presents the powder morphology as obtained using SEM. Most of the powders were nearly spherical but with small satellite particles on their surfaces, which affects the powder flowability. Li et al. (2020) also observed the small satellite particles. Spherical-shaped powder particles are recommended for

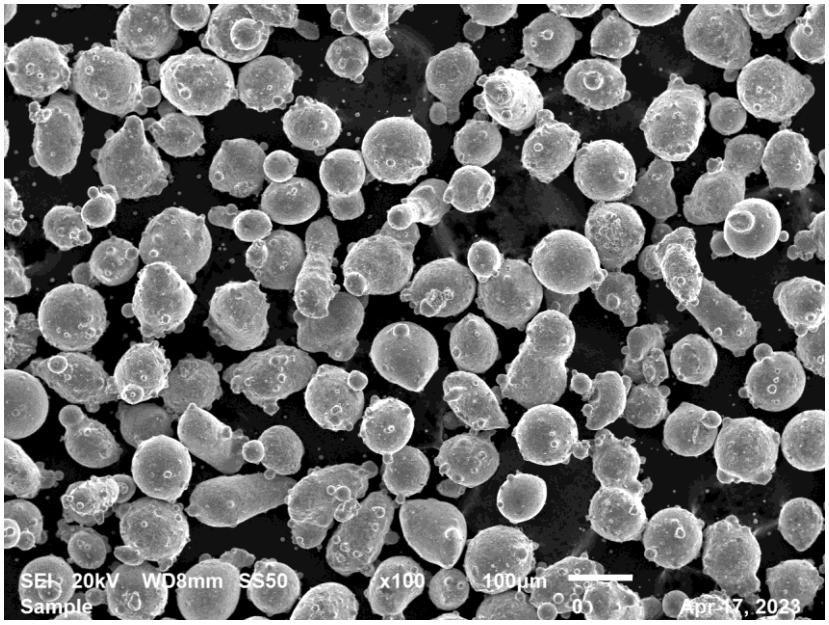

Figure 3.1: SEM Micrograph of As-Received CoCrMo Alloy Powders

AM techniques since they have good flowability and also allow sufficient laser energy absorption (Mahamood, Akinlabi, Shukla, & Pityana, 2014; Jang, Kim, Han, Yoon, & Jung, 2020). Good flowability occurs because the particles do not adhere to each other. The substrate used in this study was SS316L (100 x 100 x 10 mm). SS316L substrate was selected for this study because of its good metallurgical bonding with CoCrMo alloy (Wilson, Jones, Jin, & Shin, 2013). The bonding performance between the substrate and the alloy to be deposited is essential. Unsuccessful bonding can result in delamination.

3.2 Experimental Procedure

The experiments were carried out in the labs at the Council for Scientific and Industrial Research (CSIR), South Africa. Table 3.2 shows the list of equipment that were used for the experimental work.

Table 3.2: List of Equipment

No.	Equipment	Use
1.	Laser Engineered Net Shaping (LENS) machine	Fabrication of samples
2.	MarSurf PS1 surface roughness tester	Surface roughness measurement
3.	Olympus BX51M optical microscope	Microstructural analysis
4.	Zwick Roell Vickers hardness tester	Microhardness measurement
5.	Scanning electron microscope	Microstructural analysis
6.	Rtec tribometer	Wear test
7.	Box furnace	Heat treatment

The Optomec LENS model 850-R integrated with a 1kW IPG fiber laser shown in Figure 3.2 was utilized in this study to manufacture two sets of 16 block samples (10 x 10 x 5 mm) on the SS316L substrates, as shown in Figure 3.3. Argon gas was used to minimize oxidation during fabrication. The LENS machine is used for powder particles with a size that ranges from 45 μm to 100 μm (Arthur, Baloyi, Moller, & Pityana, 2016).

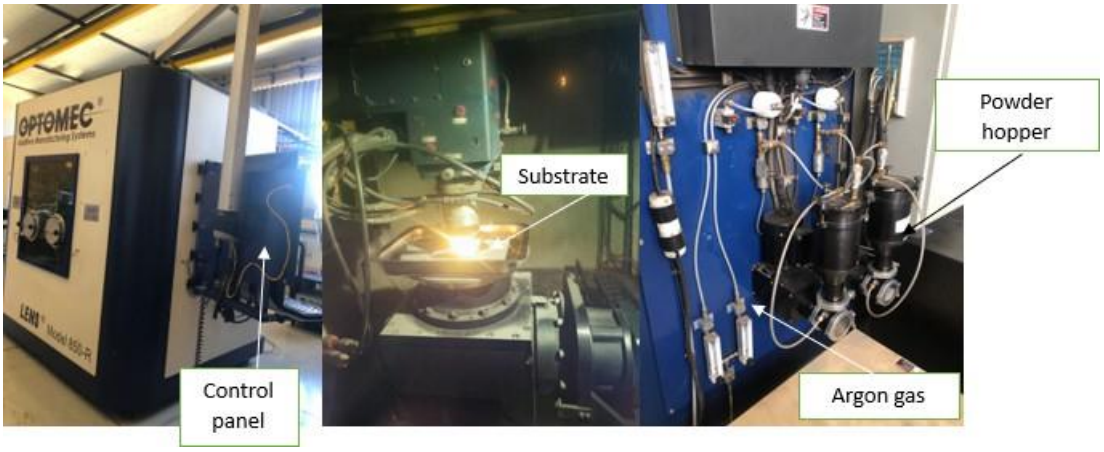

Figure 3.2: Optomec LENS Machine Used in the Study

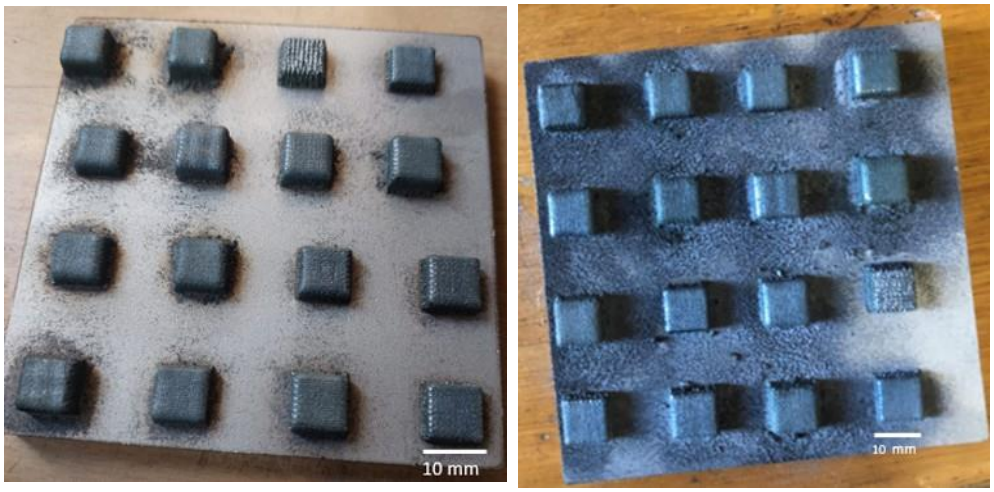

Figure 3.3: Fabricated Block Samples

The powder feed rate of the machine is controlled through its rotational speed. Therefore, flowability graphs were utilized to establish the feed rates of the powders in revolutions per minute (rpm). Powder flow samples were obtained from the nozzle head at varied rpm, constant gas flow rate, constant spot diameter, constant hatch distance and constant layer thickness. Figure 3.4 was obtained from the powder flow rate study. Equation 3.1 was obtained and was used to convert the powder feed rates from grams per minute to rpm.

$$y = 1.2857x - 0.3413 \qquad (3.1)$$

where y is the average mass in grams per minute and x is revolutions per minute.

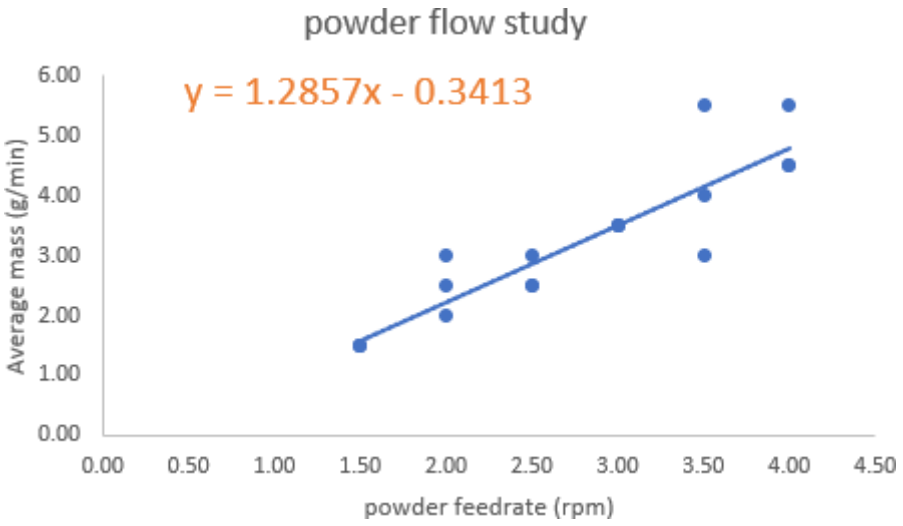

Figure 3.4: Flowability Chart of the Powder

Before deposition, the substrates were prepared by sandblasting and cleaning with acetone to eliminate oil and impurities from their surfaces. Scan speed, powder feed rate, and laser power were the process variables that were varied, while the hatch spacing, laser beam diameter and layer thickness were kept constant. The responses include microhardness, surface roughness and porosity.

3.3 Design of Experiments

Response surface methodology (RSM) was used in this study to predict and explain the interaction between responses and input variables. RSM allows the estimation of interaction between the independent variables, the quadratic effect, and hence provides an idea of the shape of the response surface. The optimization of the process parameters is vital to improving the performance characteristics of implants. The parameter design is a vital step in this method to obtain high-quality products without increasing the cost. Central composite design (CCD) was adopted in the design of experiments due to its effectiveness and high flexibility using Design Expert 13.0 software (Kicsi, Cojocaru, Macoveanu, & Bilba, 2010). CCD is an effective design for building a second-order experimental model. The CCD matrix composed of two center points and fourteen non-center points. The range of the input factors used in this study were identified based on preliminary experiments where samples were printed and cut to determine whether the samples were fully dense. Table 3.3 displays the levels and range of the input factors

that were varied. The CCD table containing the 16 experimental observations with three input process parameters is shown in Table 3.4.

Table 3.3: The selected Input Factors

Parameter	Units	Levels				
		$-\alpha$	-1	0	+1	$+\alpha$
Laser power	W	131.821	200	300	400	468.179
Scanning speed	mms^{-1}	4.07618	5.3	7.095	8.89	10.1138
Powder feed rate	$gmin^{-1}$	1.65	2.5	3.75	5	5.85

Table 3.4: Process Parameters Designed According to the CCD Matrix Approach

Std Run Factors				
		Laser power (W)	Scan speed (mms^{-1})	Powder feed rate ($gmin^{-1}$)
1	14	200	5.3	2.5
2	13	400	5.3	2.5
3	6	200	8.89	2.5
4	11	400	8.89	2.5
5	3	200	5.3	5
6	1	400	5.3	5
7	8	200	8.89	5
8	16	400	8.89	5
9	4	131.821	7.095	3.75
10	5	468.179	7.095	3.75
11	2	300	4.07618	3.75
12	9	300	10.1138	3.75
13	12	300	7.095	1.64776
14	7	300	7.095	5.85224
15	15	300	7.095	3.75
16	10	300	7.095	3.75

3.4 Sample Preparations

Sample preparations were conducted before microstructural analysis, porosity analysis, surface roughness, and microhardness tests. The metallographic sample preparation methods comprised of the following steps:

3.4.1 Sample Cutting and Mounting

The samples were cut from the substrates using a Struers Labotom-5 metal cutting machine. The cutting machine contains a water-cooling system that enables the

minimization of heat generation zones in the samples. The cutting disk used in this study is Struers 40A25 disk. Samples were mounted using the Automatic Mounting Press as shown in Figure 3.5.

Figure 3.5: Mounted Samples.

3.4.2 Grinding and Polishing Process

A Struers TegraPol-25 machine shown in Figure 3.6 was used in grinding the mounted samples using Rhaco grit grinding papers with grit sizes P120, P320, P1200, P4000 and water before polishing with MD Mol and MD Chem cloths with water-based diamond suspensions with particle sizes of 3 μm and 1 μm. The samples were then cleaned with water then rinsed with ethanol before air drying.

Figure 3.6: Grinding and Polishing Machine at CSIR

3.4.3 Etching Process for Microstructural Analysis

Electro-etching was done using stainless-steel electrodes and a 4 V Frederiksen DC power supply in Beraha's solution of 100 mL H2O, 10 mL HCI and 1g Potassium metabisulfite (K2S2O5) for 10 seconds to reveal the microstructure using the optical microscope. The electro-etching equipment used in this study is shown in Figure 3.7.

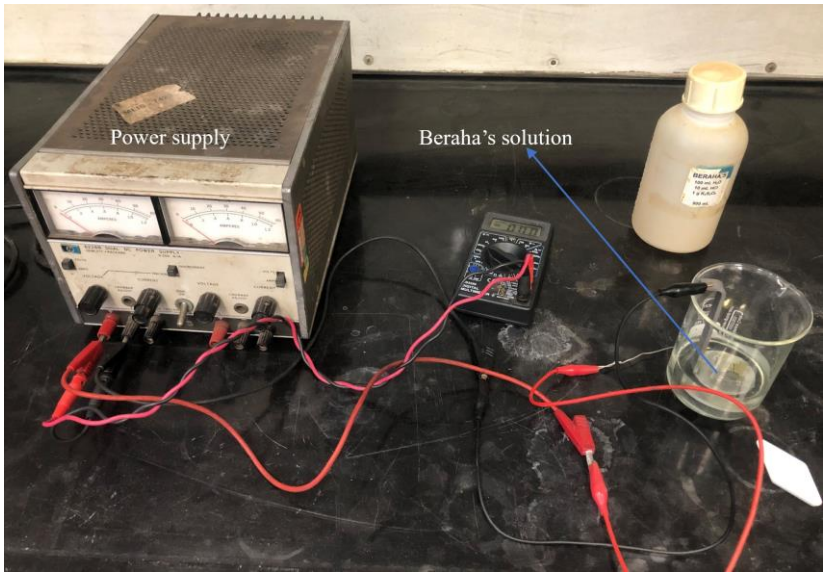

Figure 3.7: Experimental Set Up for Electro-Etching.

3.5 Sample Characterisation

Sample characterisation were conducted to determine the surface roughness, microstructure, microhardness and porosity.

3.5.1 Surface Roughness Measurement

The measurement of the average roughness (*Ra*) of the top surface was executed using the MarSurf PS1 surface roughness tester with a 2 µm diameter probe. Roughness values at three different points of the samples were recorded, and their average was determined, which was replicated twice.

3.5.2 Porosity Analysis

To characterize the pores in the material, the Olympus BX51M optical microscope was used to obtain the images of the polished surface. The surface was divided into 12 portions before analyzing the obtained images using the Stream Essentials image processing software. Stream Essentials software helped calculate the ratio of the area of pores to the whole surface area. The porosity analysis process was replicated twice by grinding and polishing another set of samples before examining them under the microscope.

3.5.3 Microstructural Analysis

An Olympus BX51M optical microscope (OM) was used to view the microstructure properties of cracks, grain structures, and pores. A Scanning Electron Microscope (SEM) installed with an Energy Dispersive X-Ray Spectroscopy (EDS) was used to analyze the powder morphology. Furthermore, SEM was used to analyze the micropores, chemical composition, and microstructure.

3.5.4 Microhardness Test

A Zwick Roell Vickers hardness tester was used to carry out the microhardness tests. The dwell time used was 10 s under a load of 1000 gf according to ASTM E384-17 standard. Manual measurements of indentations were performed by altering the magnification of the camera from x10 to x40 after the automatic measurements to correct any error that may have occurred. Figure 3.8 presents the indentations on a sample. The average microhardness values of 21 uniformly distributed indentations were recorded.

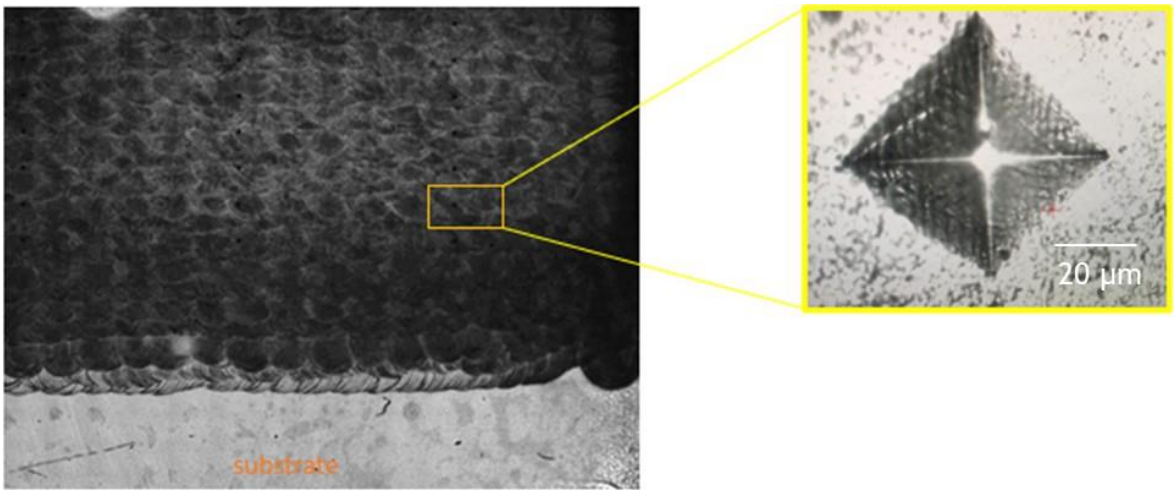

Figure 3.8: Vickers Indentations on CoCrMo Surface Manufactured by LENS

3.6 Optimization of Input Factors using Response Surface Methodology

Optimization based on RSM was carried out to obtain an optimum combination of parameters for minimum surface roughness, minimum porosity, and maximum microhardness. Analysis of Variance (ANOVA) was used to identify the parameters that significantly influence the response. Mathematical equations for microhardness, surface roughness and porosity were developed that can be used to predict the response for any provided parameters. The second-order models were validated by conducting experiments with the new set of optimum parameters. The response values obtained were then compared with the values predicted using the models. The difference between the predicted and the experimental values was computed to determine the percentage error for the validation data. Surface plots and contour plots that can be used to comprehend the influence of process parameters on the response were generated. The desirability approach described in Equation 3.1 was used in this study due to its simplicity, provides importance for individual responses, and offers flexibility in weighing individual responses.

$$\left[\prod_{i=1}^{N} d_i^{r_i}\right]^{1/\sum r_i} \tag{3.1}$$

Where N is the total number of responses, r_i is the importance of a particular response, and d_i is the partial desirability function for particular responses (Long, Li, Shi, Gui, &

Qiu, 2023). According to this method, the desirability function can find multiple points for a numerical optimization process. Graphical and numerical optimization was executed. The most desirable operating conditions based on the identified criterion were identified before validation experiments were executed.

3.7 Sample Postprocessing and Analysis

The optimum parameters obtained using RSM were used to fabricate optimum samples. The optimum samples were used to conduct heat treatment, wear test and X-ray diffraction (XRD) test.

3.7.1 Heat Treatment

Heat treatment was conducted in a box furnace supplied by Carbolite Gero. The heat treatment cycles were formulated based on the findings derived from prior studies, which resulted in an improvement in the mechanical performance of CoCrMo alloy samples manufactured by SLM (Li, Wang, Lou, Xia, & Fang, 2020). The samples were heated to 450 ℃, and the temperature was maintained for 45 min. The samples were then reheated to 750 ℃ and held for 60 min before water quenching to room temperature.

3.7.2 Wear Test

A ball-on-disk wear test was carried out on the heat-treated and as-built specimen at room temperature using a Rtec tribometer. The maximum normal load that can be considered when using the equipment is 150 N. The counterwear body was a silicon carbide (SiC) spherical indenter with a diameter of 6.35 mm. The CoCrMo alloy specimens were grinded with papers with grit sizes P320 and P1200 and polished with diamond suspensions with particle size 0.2 µm to retain a uniform contact area before the tests were performed. The sliding distance was 2 mm, duration was 10 min, acceleration was 0.1 mms^{-2}, velocity was 3 mms^{-1}, and the normal load was 120 N for each sample. The experiments were replicated twice, and the average values were obtained to calculate the specific wear rate. Also, the coefficient of friction (COF) was obtained. The wear volume calculation was executed according to ASTM G99 using

equations 3.2 and 3.3:

$$V_W = \frac{a\pi h^2}{3b}[3R - h](mm^3) \tag{3.2}$$

$$h = R - \sqrt{R^2 - b^2}(\mu m) \tag{3.3}$$

where V_W is the wear volume in (mm^3), a and b are the half-length and width of the wear scar track, respectively, and R is the radius of the pin (Malikongwa, Tlotleng, & Olakanmi, 2021). Archard's model shown in equation 3.4 was adopted to calculate the specific wear rate, W_R taking into account the normal load N, the wear volume V_W and the sliding distance l_s.

$$W_R = \frac{V_w}{N * l_S} \tag{3.4}$$

3.7.3 X-ray diffraction (XRD)

X-ray diffraction (XRD) using Bruker D8 Advance powder diffractometer was conducted on heat-treated and as-built optimum samples to detect the phase composition. The XRD machine is installed with a LynxEye XE energy-dispersive strip detector and a Cu tube X-ray source. cu-Kα radiation with a wavelength of 1.5418 A and 2θ between 20 and 90 degrees was used in this analysis. The machine was run at 40 mA and 40 kV.

3.8 Summary

As indicated in this chapter, the material used in this work was gas-atomized cobalt-chromium-molybdenum (CoCrMo) alloy powder and SS316L substrates. Laser Engineered Net Shaping equipment used was described. Furthermore, the sample characterisation methods and equipment used were discussed. Response surface method was used in the design of experiments. ANOVA analysis was conducted to determine the influence of each factor against the factors of scan speed, powder feedrate and laser power. Mathematical models for optimising the responses and factors were developed. Lastly, the desirability approach used in obtaining the optimum process parameters was described. The optimum set of parameters obtained was used to

fabricate validation samples.

CHAPTER FOUR

RESULTS AND DISCUSSION

This chapter analyses the statistical analysis results for porosity, surface roughness, microhardness, and microstructural properties. RSM was then applied to identify the optimum set of parameters. The contour and main effects plots are also presented in this section. They describe the effects of scan speed, powder feed rate, and laser power on microhardness, surface roughness, and porosity of LENS fabricated CoCrMo alloy. Further, the wear analysis results of LENS fabricated CoCrMo alloy are discussed.

4.1 Results of RSM Model

Table 4.1 presents the 16 experimental observations with three input process parameters and three responses. The responses obtained were analyzed to determine the quadratic models for surface roughness, microhardness, and porosity via RSM. Analysis of Variance (ANOVA) was executed to evaluate the significance of the model and to eliminate the insignificant terms.

4.1.1 Microhardness of CoCrMo Alloy Samples Fabricated by LENS Technique

Table 4.2 presents the ANOVA evaluation of the microhardness findings. The statistical significance of the model is validated by its F-value of 16.75. Further, the p-values < 0.05 confirm the statistical significance of the model terms. Table 4.2 shows that lack of fit of p-value 0.6257 is not significant. The adequate precision value is 14.0147. A ratio higher than four is desirable (Olakanmi, et al., 2019; Sun & Hao, 2012). Therefore, the design space can be explored using the model since the signal is satisfactory.

Table 4.1: Process Parameters and Results of the CCD Matrix Approach

Std	Run	Laser power (W)	Scan speed (mms^{-1})	Powder feed rate ($gmin^{-1}$)	Microhardness (HV)	Porosity (%)	Surface roughness (Ra) (μm)
1	14	200	5.3	2.5	380.833	0.08	8.5167
2	13	400	5.3	2.5	371.262	0.24	3.622
3	6	200	8.89	2.5	389.714	0.05	14.6625
4	11	400	8.89	2.5	374.071	0.14	9.3825
5	3	200	5.3	5	385.857	0.12	10.2033
6	1	400	5.3	5	396.548	0.05	9.2487
7	8	200	8.89	5	369.857	0.34	12.9133
8	16	400	8.89	5	369.452	0.19	10.5
9	4	131.821	7.095	3.75	384.976	0.15	17
10	5	468.179	7.095	3.75	384.31	0.09	9.2833
11	2	300	4.07618	3.75	379.071	0.11	4.68
12	9	300	10.1138	3.75	368.095	0.23	9.3633
13	12	300	7.095	1.64776	377.167	0.09	10.09
14	7	300	7.095	5.85224	388.548	0.16	12.3767
15	15	300	7.095	3.75	391.262	0.1	11.993
16	10	300	7.095	3.75	387.5	0.11	8.4476

Table 4.2: ANOVA for Microhardness.

Source	Sum of Squares	df	Mean Square	F-value	P-value	
Model	1113.21	9	123.69	16.75	0.0014	Significant
A-Laser power	18.86	1	18.86	2.55	0.1611	
B-Scan speed	182.07	1	182.07	24.66	0.0025	
C-Powder feed rate	45.67	1	45.67	6.19	0.0473	
AB	36.84	1	36.84	4.99	0.0669	
AC	157.53	1	157.53	21.34	0.0036	
BC	375.19	1	375.19	50.82	0.0004	
A^2	26.83	1	26.83	3.63	0.1052	
B^2	291.79	1	291.79	39.52	0.0008	
C^2	50.43	1	50.43	6.83	0.0399	
Residual	44.29	6	7.38			
Lack of Fit	37.22	5	7.44	1.05	0.6257	Not significan
Pure Error	7.08	1	7.08			
Cor Total	1157.50	15	R^2	0.9617		
Std. Dev	2.72	Adjusted R^2	0.9043			
Mean	381.16	Predicted R^2	0.7269			
		Adeq Precision	14.0147			

Scan speed (B), feed rate (C), the interaction between laser power and feed rate (AC), the interaction between the scan speed and feed rate (BC), second order of the scan speed (B^2) and the feed rate x feed rate (C^2), are the significant model terms as seen in Table 4.2. P-values > 0.1 implies that the model terms are insignificant. Comparative analysis of F-values of the terms: B, C, AC, BC, B^2, C^2 illustrates the degree of impact

of the model terms as follows: C < C^2 < AC <B < B^2 < BC.

The coefficient of determination, R^2 = 0.9617, demonstrates a good relationship between the experimental and predicted microhardness values. R^2 measures the goodness of fit. The obtained values of predicted R^2 and adjusted R^2 were 0.7269 and 0.9043, respectively, and are in reasonable agreement since their difference is <0.2. Based on the Prob > F values, model terms such as case B, C, AC, BC, B^2, C^2 should be retained in the mathematical model, and the statistically insignificant model terms could be eliminated. The quadratic model for estimating the microhardness values of CoCrMo alloy is described in equation 4.1:

$$\text{Microhardness (HV)} = 389.392 - 3.65131 \times B + 1.82871 \times C + 4.4375 \times AC - 6.84825 \times BC - 5.61217 \times B^2 - 2.33314 \times C^2 \quad (4.1)$$

4.1.2 Porosity of LENS Fabricated CoCrMo Alloy

Since tests for validating the significance of the regression model are vital, ANOVA was utilized in evaluating the tests. Table 4.3 shows the summary statistics of the porosity (%) model. The p-value < 0.05 indicates that the model is statistically significant. The lack of fit of p-value of 0.2546 implies the model fits well in the regression region. Adequate precision of 20.8502 indicates a desirable signal, as previously explained. Furthermore, the R^2 value (0.9758) obtained is close to 1, showing that the statistical model formulated for porosity correlates strongly with the actual experimental data. The significant factors (with p-values < 0.05), as presented in Table 4.3, are scan speed (B), powder feed rate (C), laser power x feed rate (AC), laser power x scan speed (AB), scan speed x feed rate (BC) and scan speed x scan speed (B^2). The obtained empirical relationship that presents the relationship between the LENS parameters and porosity is described in equation 4.2:

$$\text{Porosity}(\%) = 0.103949 + 0.0316189 \times B + 0.0225327 \times C - 0.01875 \times AB - 0.05875 \times AC + 0.06125 \times BC + 0.0255188 \times B^2 \quad (4.2)$$

Table 4.3: ANOVA for Porosity.

Source	Sum of Squares	df	Mean Square	F-value	P-value	
Model	0.0875	9	0.0097	26.86	0.0004	Significant
A: Laser power	0.0004	1	0.0004	1.02	0.3522	
B: Scan speed	0.0137	1	0.0137	37.72	0.0009	
C: Powder feed rate	0.0069	1	0.0069	19.15	0.0047	
AB	0.0028	1	0.0028	7.77	0.0317	
AC	0.0276	1	0.0276	76.28	0.0001	
BC	0.0300	1	0.0300	82.91	< 0.0001	
A^2	0.0006	1	0.0006	1.57	0.2564	
B^2	0.0060	1	0.0060	16.67	0.0065	
C^2	0.0009	1	0.0009	2.36	0.1752	
Residual	0.0022	6	0.0004			
Lack of Fit	0.0021	5	0.0004	8.49	0.2546	Not significant
Pure Error	0.0000	1	0.0000			
Cor Total	0.0897	15	R^2	0.9758		
Std. Dev	0.0190		Adjusted R^2	0.9395		
Mean	0.1406		Predicted R^2	0.8178		
			Adeq Precision	20.8502		

4.1.3 Surface Roughness of LENS Fabricated CoCrMo Samples

Analysis of variance was executed for the surface roughness responses to determine the significance of the model, as indicated in Table 4.4. The obtained p-value < 0.05 confirms the statistical significance of the model at a 95% confidence level. Lack of fit has a p-value of 0.9664 and is insignificant, implying that the model fits well in the whole regression region. R^2 value of 0.9391 obtained is close to 1, which elucidates a small deviation between the predicted and observed values. Furthermore, if the predicted R^2 and adjusted R^2 values are close and high, the model can describe the fabrication process entirely. The predicted R^2 value is 0.6753 while the adjusted R^2 is 0.8477 and are in reasonable agreement as previously explained. The significant model terms are laser power (A), second-order of scan speed (B^2), and scan speed (B) as shown in Table 4.4.

Table 4.4 confirms laser power as the most significant term (F-value = 30.88) in

comparison to scan speed (F-value=24.75) and second order of scan speed, B^2 (F-value = 8.97) in the impartation of surface roughness to the CoCrMo alloy samples. The mathematical model obtained for correlating the responses is described as shown in equation 4.3:

$$\text{Surface roughness } (\mu\text{m}) = +10.2781 - 1.94192 \times A + 1.73861 \times B - 1.2705 \times B^2 \quad (4.3)$$

Table 4.4: ANOVA Results for Surface Roughness in LENS

Source	Sum of Squares	df	Mean Square	F-value	P-value	
Model	154.27	9	17.14	10.28	0.0052	Significant
A-Laser power	51.50	1	51.50	30.88	0.0014	
B-Scan speed	41.28	1	41.28	24.75	0.0025	
C-Powder feed rate	8.11	1	8.11	4.87	0.0696	
AB	0.4250	1	0.4250	0.2548	0.6317	
AC	5.79	1	5.79	3.47	0.1117	
BC	7.89	1	7.89	4.73	0.0726	
A^2	7.39	1	7.39	4.43	0.0799	
B^2	14.95	1	14.95	8.97	0.0242	
C^2	0.4425	1	0.4425	0.2653	0.6249	
Residual	10.01	6	1.67			
Lack of Fit	3.72	5	0.7446	0.1185	0.9664	Not significant
Pure Error	6.28	1	6.28			
Cor Total	164.28	15	R^2	0.9391		
Std. Dev.	1.29		Adjusted R^2	0.8477		
Mean	10.14		Predicted R^2	0.6753		
			Adeq Precision	12.0565		

4.2 Confirmation of the Adequacy of the Statistical Models

To verify the degree of fitting of the regression equations 4.1, 4.2, and 4.3 developed for microhardness, porosity, and surface roughness, the predicted versus actual values were plotted as presented in Figure 4.1, 4.2 and 4.3. The plots indicate a strong relationship between predicted and observed values. Also, this agrees with the R^2 values of 0.9617, 0.9758, and 0.9391 for microhardness, porosity, and surface roughness, respectively.

Further, the mathematical models were validated using a study by Mallik et al. (2014) and confirmatory experiments as presented in Table 4.5. It can be concluded that there is a good agreement between the statistical models and the experimental values.

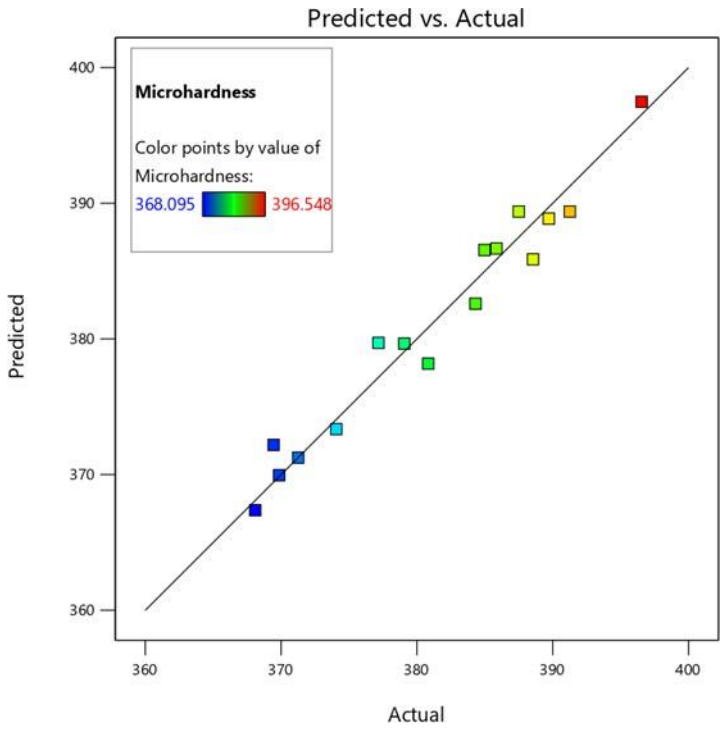

Figure 4.1: Plot of Predicted vs. Actual values of microhardness

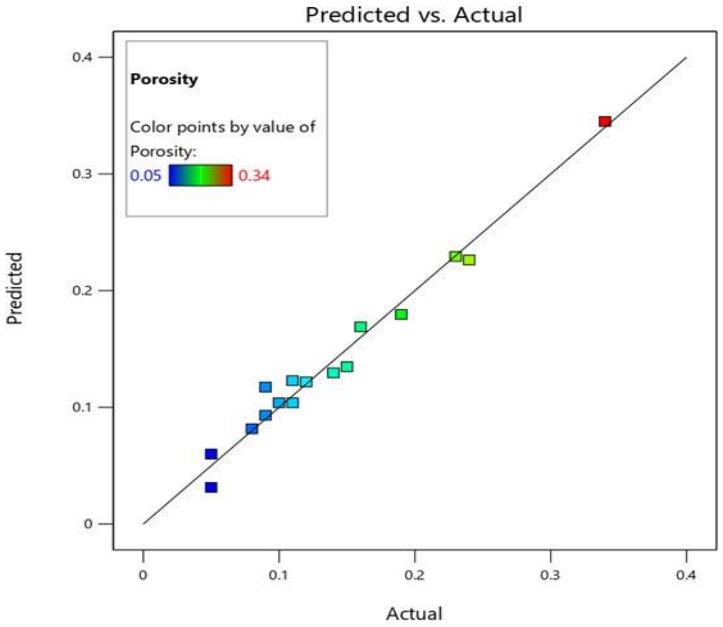

Figure 4.2: Predicted vs. Actual Values of Porosity

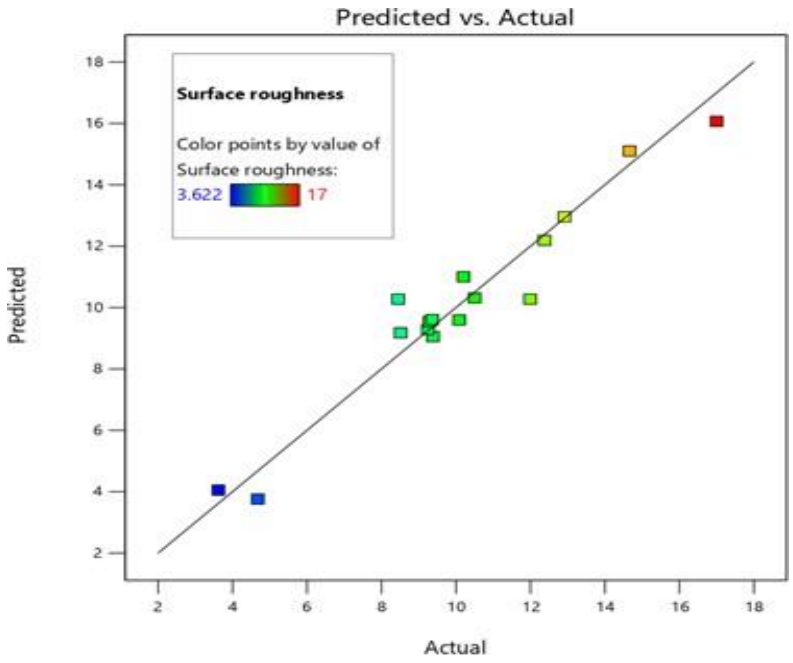

Figure 4.3: Predicted vs. Measured Values of Surface Roughness

Table 4.5: Confirmatory Tests for Mathematical Models

Exp. No.	Laser power (W)	Scan speed (mm/s)	Powder feed rate (g/min)		Microhardness (HV)	Porosity (%)	Surface roughness (μm)	Ref
1	200	10	5	Experimental	431			(Mallik, Rao, & others, 2014)
				Predicted	355.705			
				% Error	+17.47			
2	386.896	5.3	4.748	Experimental	387.4286	0.06	8.7775	
				Predicted	395.510	0.05	8.595	
				% Error	−2.086	+16.67	+2.079	
3	350	5.3	4.748	Experimental			8.456	
				Predicted			8.524	
				% Error			−0.804	

4.3 Influence of LENS Process Parameters on the Quality Properties of the Samples

The following sections present the contour and main effects plots. They describe the effects of scan speed, powder feed rate, and laser power on microhardness, surface roughness, and porosity of LENS fabricated CoCrMo alloy. Further, the wear analysis results of LENS fabricated CoCrMo alloy are discussed.

4.3.1 Influence of LENS Deposition Variables on Microhardness

The mechanical characteristics in additively manufactured parts are desired to be better or comparable to those fabricated by conventional methods. In this study, the CoCrMo alloy processed by LENS exhibited superior microhardness (368.095-396.548 HV) compared to cast CoCrMo alloy that demonstrated hardness values of 265-330 HV and forged CoCrMo alloy with hardness values of 230-350 HV (Monroy, Delgado, Sereno, Ciurana, & Hendrichs, 2014). Hence, LENS can produce parts with better mechanical properties than conventional processes.

The main effects plot, which reveals how the microhardness varies with the input parameters, is presented in Figure 4.4. Figure 4.4 (a) demonstrates that when the laser power is increased from 200 W to 300 W, microhardness increases. However, the microhardness reduces when the laser power is increased above 300 W. The increase in microhardness could be due to the sufficient energy imparted into the melt pool, resulting in full densification. Decreased microhardness as laser power increased above 300 W can be explained by the excessive amount of molten material formation that can reduce viscosity and severe aggregation of particulates, causing a decrease in microhardness. Findings from Table 4.1 confirm the claim above given that microhardness values were 384.976 HV, 391.262 HV, and 384.31 HV as laser dissipated into the melt pool was set at 131.821 W, 300 W, and 468.179 W, respectively, with scan speed (7.095 mms^{-1}) and powder feed rate (3.75 $gmin^{-1}$)) being held constant.

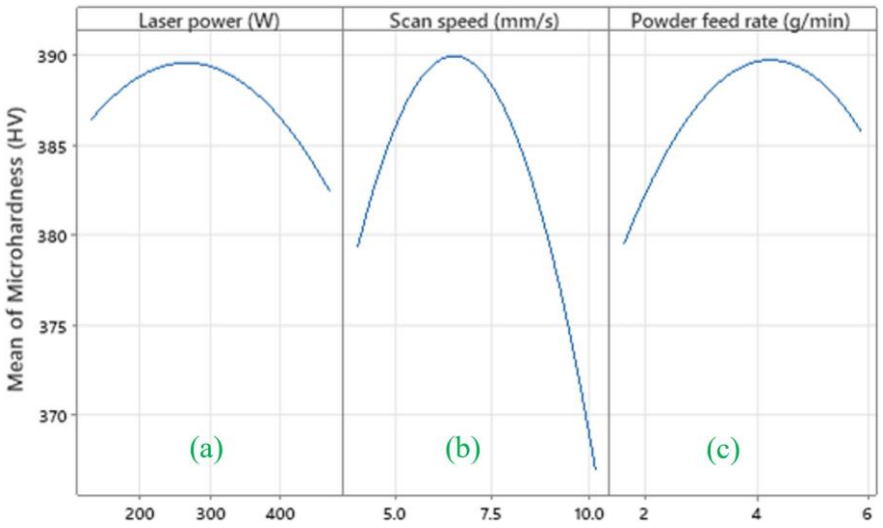

Figure 4.4: Comparison of Microhardness with Process Parameters

Microstructural analysis of the CoCrMo samples fabricated with 131.821 W, 300 W, and 468.179 W confirms that the change of process parameters influences the resulting grain structure (Monroy, Delgado, Sereno, Ciurana, & Hendrichs, 2014) as shown in Figure 4.5 (a) to (c). The micrographs in Figure 4.5 present multidirectional grains, indicating non-directional strength. The inhomogeneous microstructure is attributable to the unequal cooling rates of the melt pool. Figure 4.5 (b) confirms that the sample with the microhardness of 391.262 HV (Table 4.1) has a fine dendritic structure with a cell size of approximately 2 μm. The arrangement of the melt pools signifies complete solidification of each layer free from cracks, defects, or porosity. The microhardness value is superior to those of cast CoCrMo alloy, as previously discussed, and, therefore, suggests that the process parameters are appropriate in the fabrication of dental implants. Figure 4.5 (a) and (c) confirm that the samples produced with laser powers of 131.821 W and 468.179 W have a coarse microstructure, which resulted in a decrease in microhardness.

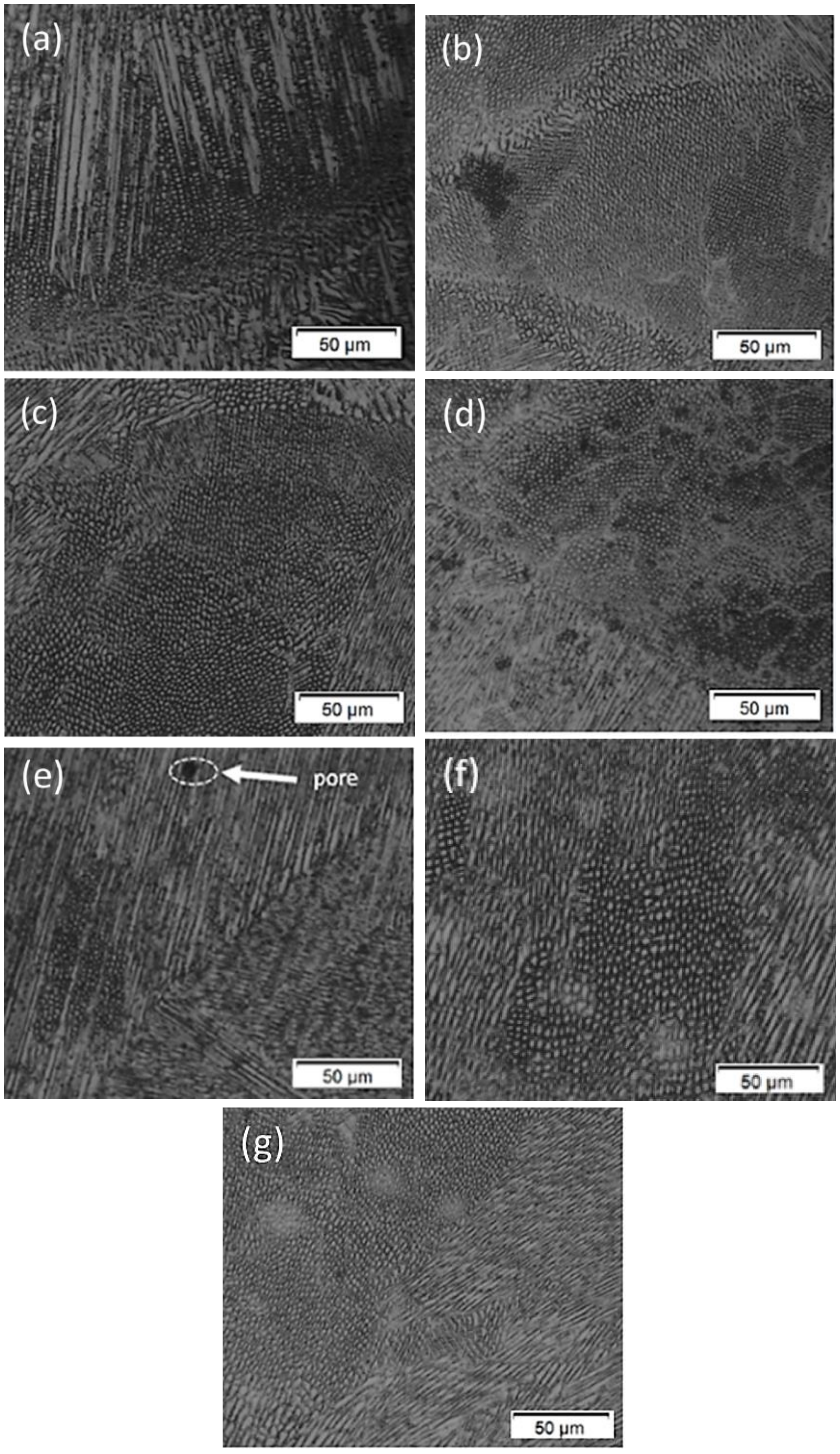

Figure 4.5: Microstructural Evaluation of LENS Manufactured CoCrMo Samples at Varying Process Parameters

Key: (a) 131.82 W, 7.095 mm/s, 3.75 g/min(b) 300 W, 7.095 mm/s, 3.75 g/min (c) 468.18 W, 7.095 mm/s, 3.75 g/min d) 300 W, 4.08 mm/s, 3.75 g/min (e) 300 W, 10.11mm/s, 3.75 g/min (f) 300 W, 7.095 mm/s, 1.65 g/min, (g) 300 w, 7.095 mm/s, 5.85

g/min

The Hall-Petch theory suggests that a fine microstructure is desired to improve microhardness. The theory defines the grain size and Vickers hardness as described in equation 4.4 (Chen, et al., 2022):

$$H_v = H_0 + K_H D^{-1/2} \quad (4.4)$$

Where K_H and H_0 are the corresponding constants and D is the average grain size diameter. The equation demonstrates that grain size positively relates to hardness. Smaller grains will result in more grain boundaries in the microstructure. Finer grain size results in higher material strength and microhardness values. Further, a finer grain size reduces the formation of cracks and microporosity and is preferable due to its excellent fatigue and tensile performance.

A study of Figure 4.4 (b) also shows that the microhardness increases as scan speed increases from 4.08 mms^{-1} to 7.1 mms^{-1}. Nevertheless, microhardness reduces after the scan speed is increased to 10.11 mms^{-1}. Table 4.1 corroborates that microhardness values were 379.071 HV, 391.262 HV, and 368.095 HV as laser beam was scanned at 4.08 mms^{-1}, 7.1 mms^{-1} and 10.11 mms^{-1}, respectively, as feed rate (3.75 $gmin^{-1}$) and laser power (300 W) were held constant. Microstructural analysis of the CoCrMo samples fabricated with 4.08 mms^{-1} (Figure 4.5d), 7.1 mms^{-1} (Figure 4.5b), and 10.11 mms^{-1} (Figure 4.5e) also indicates multidirectional grains.

Figure 4.5 (b) confirms that the increase in scan speed from 4.08 mms^{-1} to 7.1 mms^{-1} resulted in finer grains and, therefore, increased strength according to Hall-Petch's theory as previously discussed. Finer microstructure results in the formation of more grain boundaries which contributes to the trend of increase in microhardness. Other studies reported similar results of an increase in microhardness with increase in the scan speed (Mahamood & Akinlabi, 2017; Phala, Popoola, Tlotleng, & Pityana, 2018). The decrease in microhardness after a further increase of the scan speed to 10.11 mms^{-1} can be elucidated by the coarsening of the microstructure and the existence of pores, as seen in Figure 4.5 (e). The defects in the sample were influenced by inadequate

energy density for sufficient bonding of the powder particles (Li, et al., 2022).

Furthermore, it can be observed from Figure 4.4 (c) that there is an increase in microhardness as powder feed rate increases from 2.0 $gmin^{-1}$ to 4.0 $gmin^{-1}$ and then reduces as feed rate is increased further. Microhardness values were 377.167 HV, 391.262 HV and 388.55 HV as powder feed rate was set at 1.65 $gmin^{-1}$, 3.75 $gmin^{-1}$ and 5.85 $gmin^{-1}$, respectively, while laser power (300 W) and scanning speed (7.095 mms^{-1}) were held constant. Microstructural analysis of the CoCrMo samples fabricated with 1.65 $gmin^{-1}$ (Figure 4.5f), 3.75 $gmin^{-1}$ (Figure 4.5b), and 5.85 $gmin^{-1}$ (Figure 4.5g) reveals a reduction of the grain size when the feed rate was increased to 3.75 $gmin^{-1}$, which results in high microhardness values. This increased microhardness indicates that sufficient material was available for adequate melting, which could also result in microstructural refinement. Duan et al. (Duan, Zhang, & Luo, 2021) observed similar results. The powder feed rate used in the LENS process should be optimal to ensure the reduction of the unmelted particles, minimize pores, and complete melting of the powder particles. In addition, it should enable more material to be absorbed during deposition. Reduced microhardness reported as the feed rate increased above 3.75 $gmin^{-1}$ could be attributed to excessive powder available for melting that requires sufficient energy for microstructural refinement.

In conclusion, an observation of Figure 4.4 shows that the plot for the scan speed is steeper than those of feed rate and laser power, indicating that it significantly influences the microhardness more than feed rate and laser power. This is also affirmed by ANOVA analysis (Table 4.2), where the p-value of scan speed ($p=0.0025$) is less than that of the powder feed rate ($p=0.0473$) and laser power ($p=0.1611$).

Figures 4.6, 4.7 and 4.8 presents the contour graphs of the interactive influence of process variables on microhardness. The plot for feed rate and laser power expressed in Figure 4.6 was developed with the scan speed set at the center point while altering the laser power and feed rate. Microhardness values greater than 390 HV can be imparted into the samples by setting the powder feed rate within 4.5 $gmin^{-1}$ to 5.0 $gmin^{-1}$ and laser power 350.0 W to 400.0 W. Figure 4.7 presents the contour plot representing the correlation between feed rate and scan speed. At scan speed of 5.3

mms^{-1} and feed rate of 4.5 gmin^{-1} to 5 gmin^{-1}, microhardness values above 390 HV can be observed. Figure 4.8 shows that microhardness values > 390 could be obtained at scan speed: 6.5 mms^{-1} and laser power: 280 W.

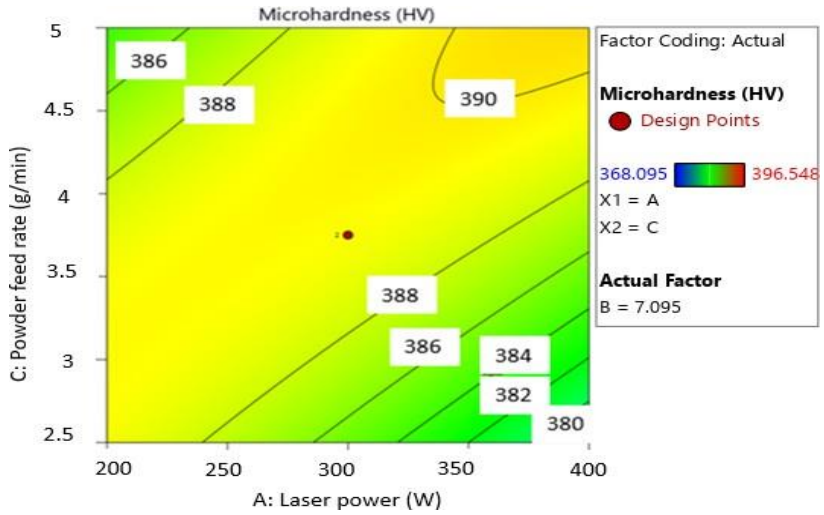

Figure 4.6: Contour Graph of the Interaction Effect of Laser Power versus Powder Feed Rate on Microhardness

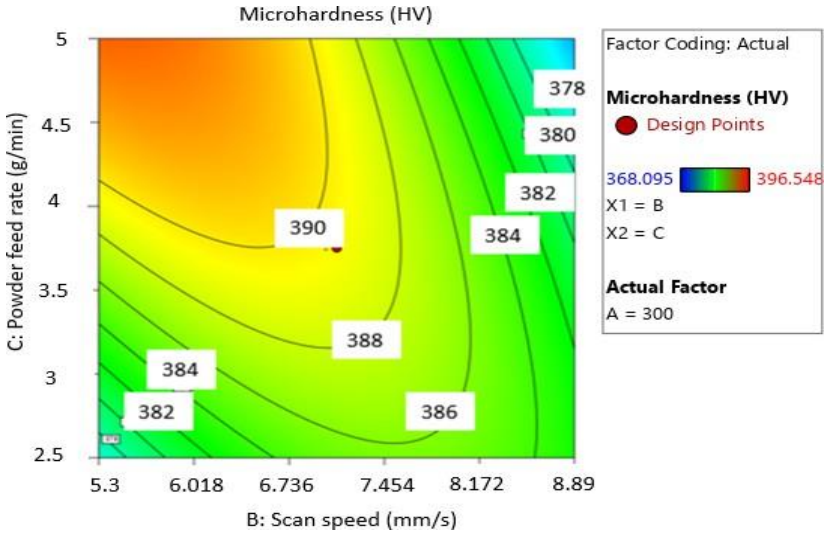

Figure 4.7: Contour Graph of the Interaction Effect of Scan Speed versus Powder Feed Rate on Microhardness

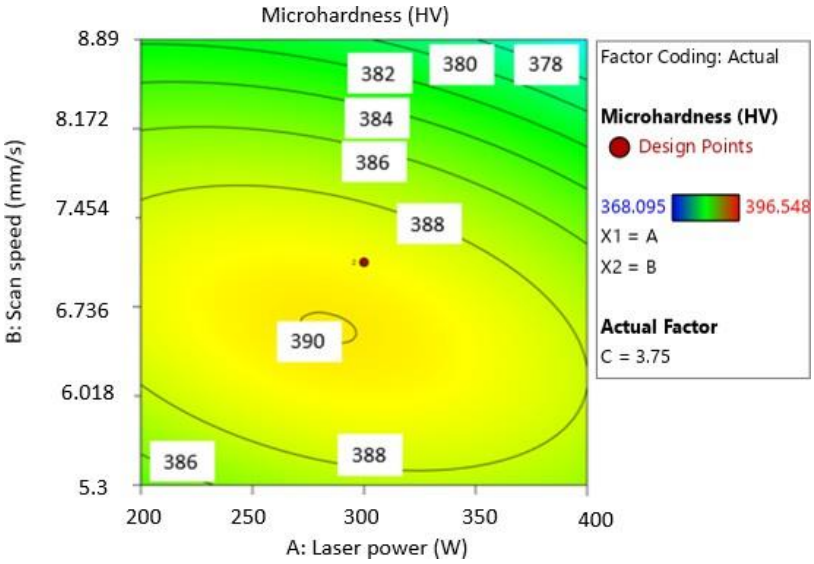

Figure 4.8: Contour Graph of the Interaction Effect of Scan Speed versus Laser Power on Microhardness.

4.3.2 Effect of LENS Input Parameters on Surface Roughness

Figure 4.9 presents a main effects plot that describes how surface roughness varies with the parameters. By increasing the laser power from 131.821 W to 300 W with the scan speed (7.095 mms^{-1}) and powder feed rate (3.75 $gmin^{-1}$) kept constant, a decrease in surface roughness from 17 µm to 8.4476 µm was noted as illustrated in Figure 4.9 (a). In addition, there was a slight increase in surface roughness to 9.2833 µm after a further increase of laser power to 468.179 W. Figure 4.10 presents samples fabricated by laser powers 300 W (Figure 4.10 a), 131.821 W (Figure 4.10 c), and 468.179 W (Figure 4.10 b), which confirms the findings in Figure 4.9 (a). Figure 4.9 (a) illustrates that laser power of 131.821 W was inadequate to melt the powder particles on the surface of the sample completely. This implies that at a laser power of 300 W, there was adequate power for more powder to be melted and complete fusibility of the powder, resulting in a smoother surface. The melting of the metal powders eliminated spatter particles on the surface of the specimen and improved the interlayer connection (Hassanin, et al., 2023). In addition, the increase in laser power improved the wettability of the melt pool. Hence, reducing the discrepancies in surface tension. Similarly, Li et al. (2003) and Mahamood et al. (2013) reported a decrease in surface roughness when they increased the laser power values. Nevertheless, the increase in

surface roughness after laser power was increased to 468.179 W could be attributed to the melting of a large amount of material with recoil pressure that could disrupt the surface of the melt pool. The higher recoil pressure due to increased laser power leads to spattering (Svetlizky, et al., 2021).

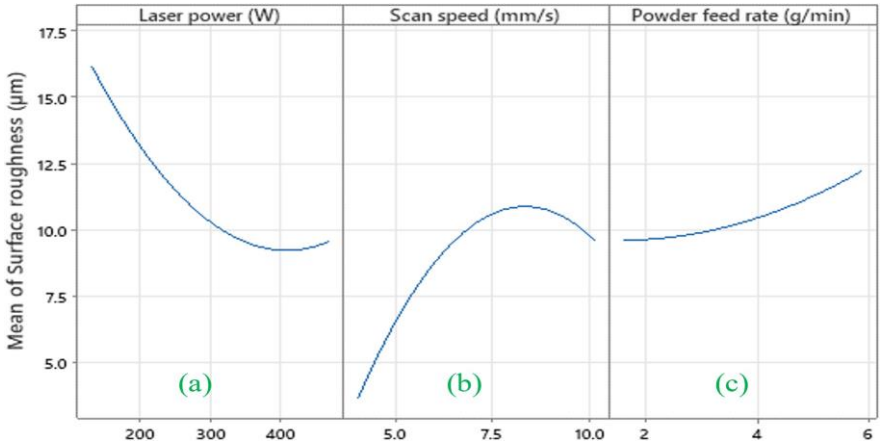

Figure 4.9: Main Effects Plot for Surface Roughness

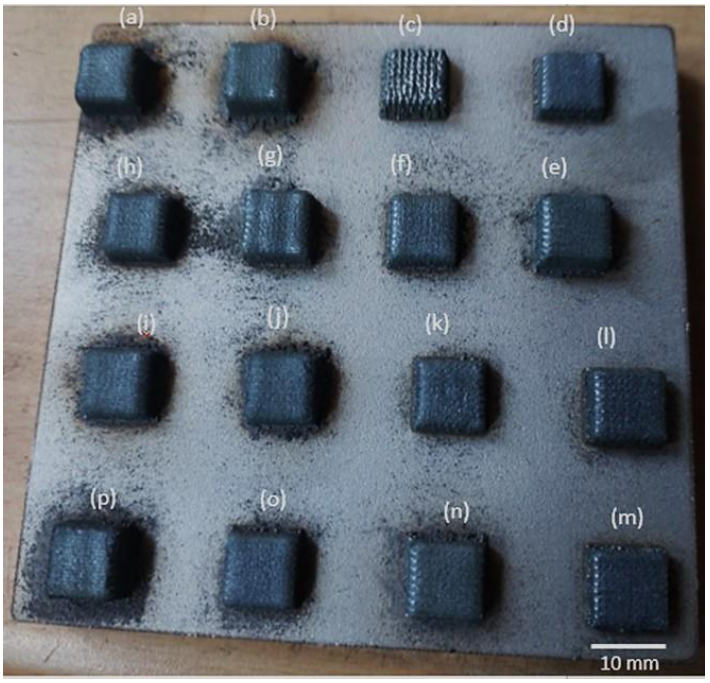

Figure 4.10: Fabricated Samples Under Different Process Parameters

Figure 4.9 (b) presents the effect of scan speed on the surface roughness of LENS fabricated CoCrMo alloy. The effects plot reveals that the change in scan speed from 5.0 mms^{-1} to 7.5 mms^{-1} led to an increase in surface roughness up to a particular point before a slight decrease in surface roughness was observed. Findings from Table 4.1 confirm this claim where an increase in scan speed from 4.07618 mms^{-1} to 7.095 mms^{-1} while the powder feed rate (3.75 $gmin^{-1}$) and laser power (300 W) were kept constant resulted in the increase in surface roughness from 4.68 µm to 11.993 µm. An additional increase of the scan speed above 7.095 mms^{-1} decreased the surface roughness to 9.3633 µm. These findings shown in Figure 4.9 (b) can also be supported by Figure 4.10 (p) (scan speed: 4.07618 mms^{-1}) and f (scan speed: 7.095 mms^{-1}). At a scan speed of 4.07618 mms^{-1} the low top surface roughness can be based on the sufficient time available for the melt pools to flatten before solidification with the aid of surface curvature and gravity forces that restrain the external sheer forces (Calignano, Manfredi, Ambrosio, Iuliano, & Fino, 2013; Aqilah, et al., 2018). Furthermore, a large melt pool can be obtained when the scan speed is kept low. The melt pool is widened by an increase in the liquid volume, therefore, resulting in larger thermal disparities throughout the melt pool and subsequently altering the surface tensions. At a scanning speed of 7.095 mms^{-1}, the rapid solidification rate could contribute to the generation of scales on the top surface of the specimen that could result in high surface roughness values (Maamoun, Xue, Elbestawi, & Veldhuis, 2018; Mahamood & Akinlabi, 2017). Li et al. (2017) observed a similar trend. The decrease in surface roughness after a further increase in the scan speed can be attributed to the decrease in consolidation time which resulted in a decrease in the splashing of powder. Also, the high scan speed decreased melt pool instability, resulting in a smoother surface (Asherloo, et al., 2023).

Table 4.4 confirms that the feed rate had little impact on surface roughness as compared to laser scan speed and laser power, and this conclusion is validated by its insignificant P-value and small F-value. However, an interesting trend can be noted in Figure 4.9 (c), whereby an increase in feed rate from 2 $gmin^{-1}$ to 5.8 $gmin^{-1}$ could increase the surface roughness. Table 4.1 validates this claim given that the surface roughness values were 10.09 µm, 11.993 µm and 12.3767 µm as the powder feed rate was 1.64776 $gmin^{-1}$, 3.75 $gmin^{-1}$ and 5.85 $gmin^{-1}$, respectively, with scan speed

(7.095 mms^{-1}) and laser power (300 W) held constant. At a feed rate of 1.64776 $gmin^{-1}$, the power available was sufficient to melt the powder, creating a large melt pool, as previously explained. Further increase of the feed rate to 3.75 $gmin^{-1}$, resulted in a smaller melt pool due to insufficient melting of the powder, contributing to an increase in surface roughness. Figure 4.10 (h) powder feed rate: 1.64776 $gmin^{-1}$, (f) powder feed rate: 3.75 $gmin^{-1}$ and (g) powder feed rate: 5.85 $gmin^{-1}$ also supports the findings in Figure 4.9 (c).

Figures 4.11, 4.12 and 4.13 presents contour plots demonstrating how the interactions between laser power and scan speed, laser power and feed rate, and powder feed rate and scan speed influence the surface roughness, respectively. Figure 4.11 shows that surface roughness is best minimized (< 8 µm) when a scan speed of 5.3 mms^{-1} is used in collaboration with laser power within the range of 265 W to 400 W. Figure 4.12 shows that surface roughness below 8 µm is attainable when powder feed rate of 2.5 $gmin^{-1}$ is combined with laser power of 400 W. Furthermore, Figure 4.13 confirms that an interaction of scan speed of 5.3 mms^{-1} with low powder feed rate of 2.5 $gmin^{-1}$ will yield low surface roughness of 6 µm.

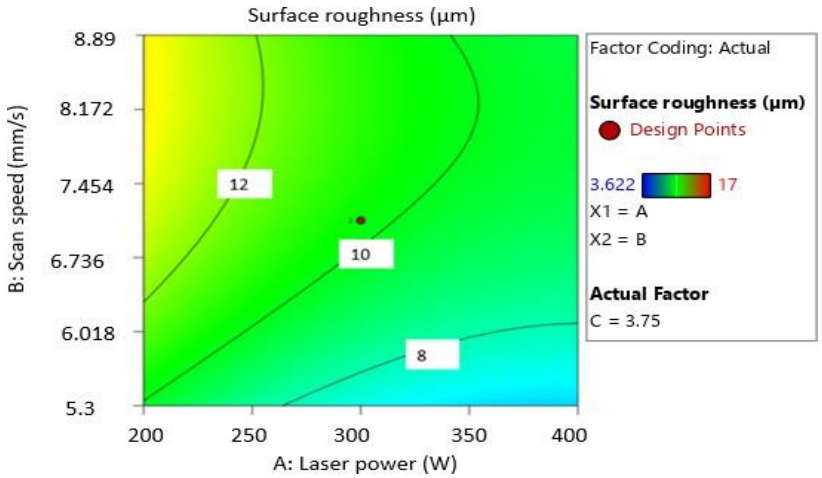

Figure 4.11: Contour Plot of the Interaction Effect of Laser Power and Scan Speed on Surface Roughness.

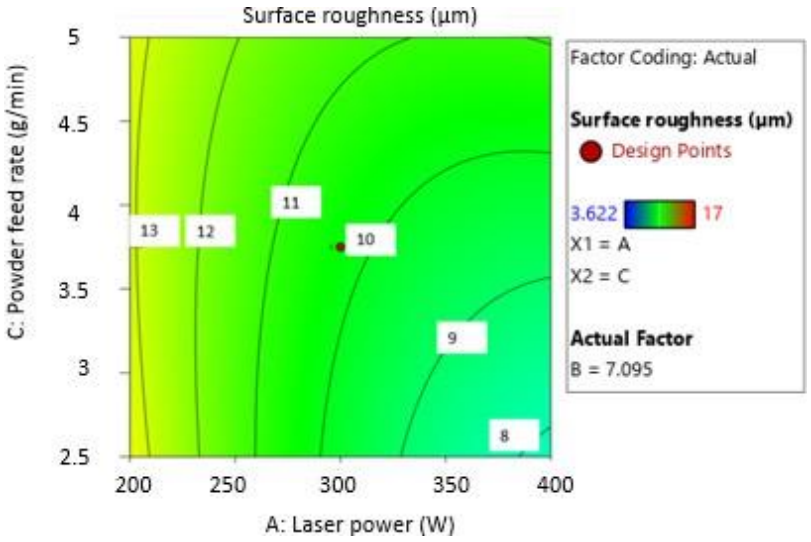

Figure 4.12: Contour Plot of the Interaction Effect of Laser Power and Powder Feed Rate on Surface Roughness

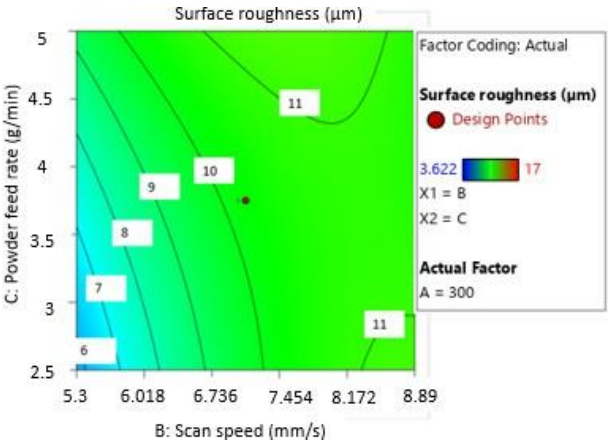

Figure 4.13: Contour Plot of the Interaction Effect of Scan Speed and Powder Feed Rate on Surface Roughness

4.3.3 Effect of LENS Input Parameters on Porosity

The effect of powder feed rate, scan speed, and laser power on the porosity of LENS fabricated samples is revealed in Figure 4.14. Figure 4.14 (b) elucidates that porosity reduces as the scan speed increases to 5 mms^{-1}, and thereafter, the percentage porosity

increases as scan speed is increased further. Findings from Table 4.1 validate this claim, given that porosity values were 0.11%, 0.10% and 0.23% for scan speeds of 4.07618 mms^{-1}, 7.095 mms^{-1} and 10.1138 mms^{-1}, respectively, with the powder feed rate (3.75 $gmin^{-1}$) and laser power (300 W) being held constant. The increase in porosity noted after the scan speed was increased above 7.095 mms^{-1} can be attributed to a decrease in the size of the melt pool that results in a reduction in the flow of the melt pool and wettability. In addition, the energy density imparted into the melt pool could be inadequate to achieve fully dense samples (Kumar, et al., 2019; Maodzeka, Olakanmi, Mosalagae, Hagedorn-Hansen, & Pityana, 2023). By increasing the scan speed, the speed of movement of the laser also increases; the melt pool temperature is low; hence, there will be insufficient material and laser power interaction, resulting in the occurrence of pores. These are similar to observations made by Benarji et al. (Benarji, Ravi Kumar, Jinoop, Paul, & Bindra, 2021) during directed energy deposition of SS316 structures. Figure 4.15 (a) to (c) also supports the above findings.

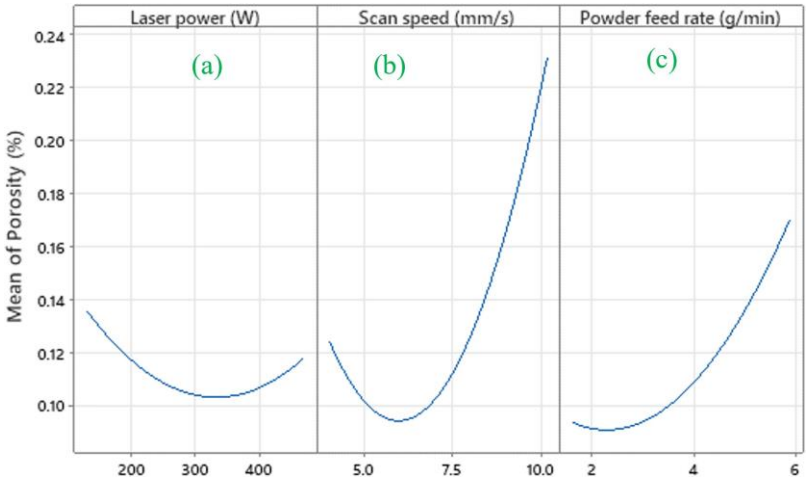

Figure 4.14: Main Effects Plot for Percentage Porosity

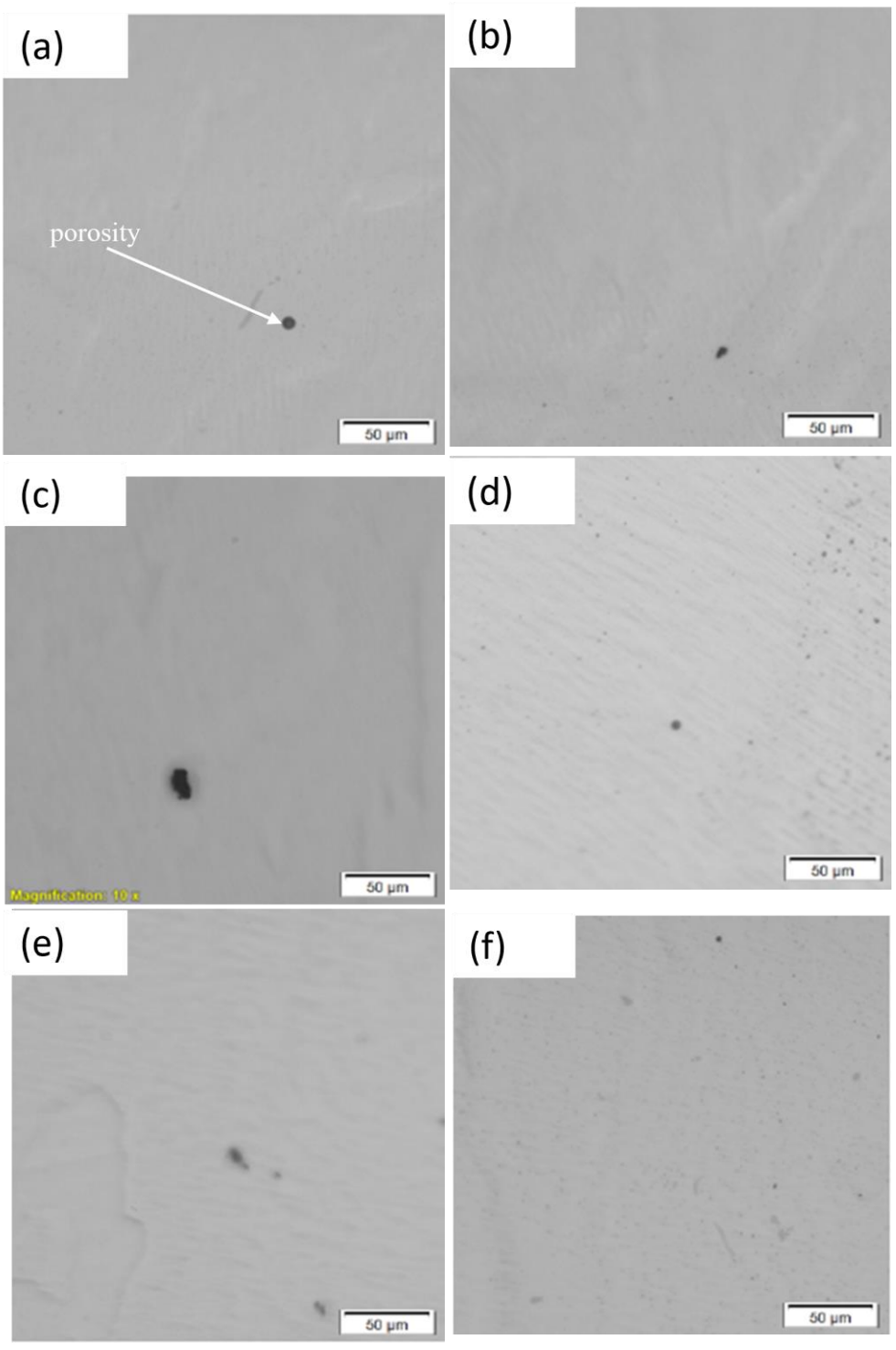

Figure 4.15: Porosity Images for CoCrMo Alloy Specimen as a Function of Scan Speed

(a) 4.07 mm/s, (b) 7.095 mm/s (c) 10.11 mm/s; laser power (d) 131 W and powder feed rate (e) 5.8 g/min, (f) 1.65 g/min.

Most of the observed porosity in the samples was gas-induced porosity (dark spots), as shown in Figure 4.15. The spherical pores could be attributed to the entrapment of argon gas in the melt pool or gases that may be present in the raw powder. It should be noted that only samples fabricated by laser power 131.821 W had both gas and lack of fusion porosity, and this could be due to insufficient energy density for melting powder particles and depositing a new layer on the preceding layer with adequate overlap (Zhang, Li, & Bai, 2017). The sample was an exceptional case with poor interlayer bonding; therefore, only the gas porosity as presented in Figure 4.15 (d) is reported in the calculation of the percentage porosity. Increasing the energy density can reduce the lack of fusion and gas porosity (Zheng, et al., 2019). According to Figure 4.15, it is evident that there was no clear trend in the distribution and spacing of pores.

A study of Figure 4.14 (c) shows that by increasing the powder feed rate from 3.75 $gmin^{-1}$ to 5.85 $gmin^{-1}$, the percentage porosity increases from 0.10% to 0.16 %. This could be due to insufficient laser power to melt the excessive powder fully. The excessive amount of powder also increases the powder density, increasing the entrapment of the shielding gas (Lin, Shen, Wu, Hwang, & Lee, 2020; Mrdak, Medjo, Veljić, Arsić, & Rakin, 2019). The optical microscope images shown in Figure 4.15 (b) for the sample with a feed rate of 3.75 $gmin^{-1}$ and Figure 4.15 (e) for the sample with a feed rate of 5.85 $gmin^{-1}$ validate the observations in Figure 4.14 (c). Furthermore, Figure 4.14 (a) indicates a decrease in the percentage porosity to 0.10% by increasing laser power to 300 W. This may be explained by sufficient energy imparted into the material to melt the powder particles sufficiently.

The influence of process parameter interactions on porosity is presented in Figure 4.16, 4.17 and 4.18. The plot for laser power against the scan speed presented in Figure 4.16 indicates that porosity < 0.1% can be obtained with a combination of scan speed of 5.3 mms^{-1} to 6.0 mms^{-1} and laser power between 200 W to 300 W. Figure 4.17 illustrates that a percentage porosity of 0.05 % can be achieved with a combination of feed rate

of 2.5 $gmin^{-1}$ and laser power of 200 W. The interplay of scan speed and feed rate will lead to a percentage porosity of 0.10% by setting powder feed rate between 4.0 $gmin^{-1}$ to 5.0 $gmin^{-1}$ in combination with scan speed within 5.3 mms^{-1} to 6.0 mms^{-1} as illustrated in Figure 4.18.

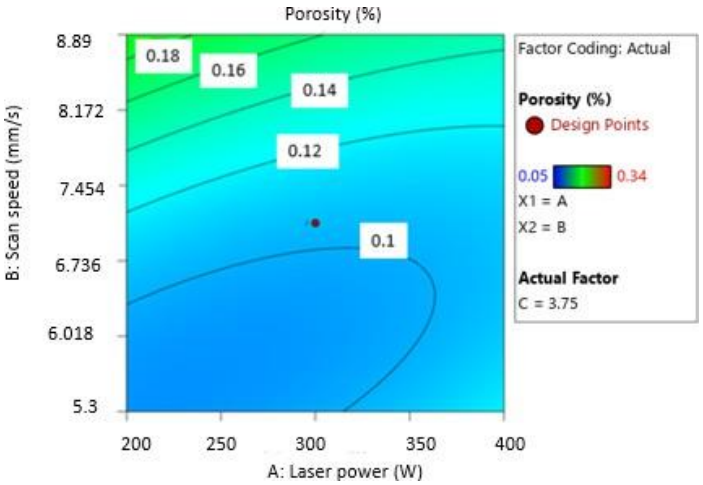

Figure 4.16: Contour Plot of the Interaction Effect of Scan Speed and Laser Power on Porosity

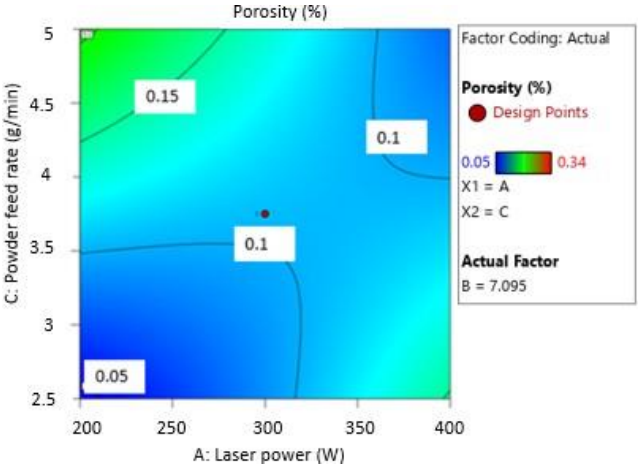

Figure 4.17: Contour Plot of the Interaction Effect of Laser Power and Powder Feed Rate on Porosity.

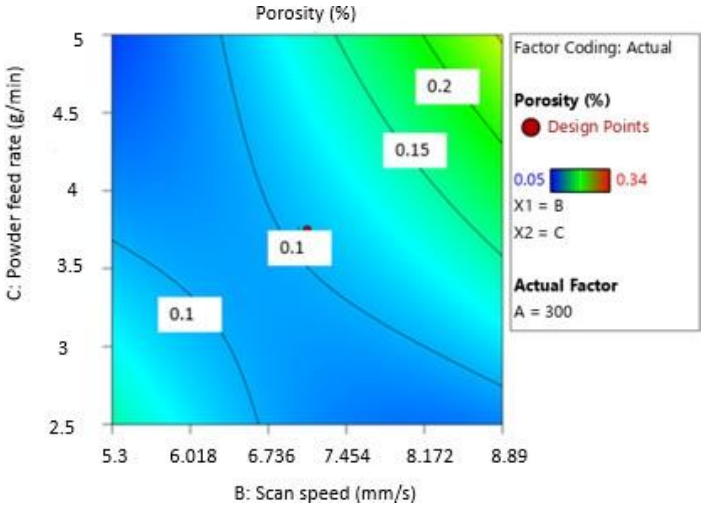

Figure 4.18: Contour Plot of the Interaction Effect of Scan Speed and Powder Feed Rate on Porosity.

4.4 Multi-objective Optimization

This study aims to obtain samples free from defects such as cracks, porosity, and a homogenous microstructure characterized by fine dendrites, which results in good mechanical properties. It is critical to select optimum input factors to balance the interplay of the process variables with quality performance. To better serve the dental application of CoCrMo alloy, a smooth surface is desired to prevent fatigue failure of dental implants. Further, low surface roughness is critical in the interaction between cells and implants. A parameter set should be selected to obtain fully dense parts since porosity influences the mechanical performance of the fabricated components. The optimization criteria for the responses and process variables are indicated in Table 4.6. Table 4.7 presents the most desirable operating conditions based on the identified criterion. The optimum parameters obtained from the RSM predicted results are scan speed: 5.3 mms^{-1}, laser power: 386.896 W, and powder feed rate 4.748 $gmin^{-1}$.

Table 4.6: Optimization Criteria.

Factor/Response	Criterion	Lower Limit	Upper Limit	Importance
Laser power, W	is in range	200	400	3
Scan speed, mm/s	is in range	5.3	8.89	3
Powder feed rate, g/min	is in range	2.5	5	3
Microhardness, HV	maximize	368.095	396.548	5
Porosity, %	minimize	0.05	0.34	5
Surface roughness, μm	minimize	3.622	17	5

Table 4.7: RSM Numerical Optimization

Solution	Laser power	Scan speed	Powder feed rate	Microhardness	Porosity	Surface roughness	Desirability	
1	**386.896**	**5.300**	**4.748**	**395.510**	**0.050**	**8.595**	**0.846**	**Selected**
2	387.672	5.300	4.746	395.504	0.050	8.593	0.846	
3	386.071	5.300	4.751	395.517	0.050	8.597	0.846	
4	385.066	5.300	4.755	395.525	0.050	8.600	0.846	
5	384.686	5.300	4.756	395.527	0.050	8.601	0.846	
6	389.034	5.300	4.741	395.494	0.050	8.590	0.846	
7	387.652	5.300	4.753	395.556	0.050	8.610	0.846	

4.5 Validation of Optimum Parameters

A validation experiment was executed to validate the optimum input factors determined by RSM. The results of the validation sample indicated the following: microhardness 387.4286 HV, porosity 0.06% and surface roughness 8.7775 μm, as presented in Table 4.8. This reveals that components with desired properties can be obtained by using the optimal input factors. Error analysis was carried out to compare the results of the confirmatory tests with those of the predicted model as shown in Table 4.8.

Table 4.8: Validation Tests Comparing Predicted and Experimental Findings

	Microhardness (HV)	Porosity (%)	Surface roughness (μm)
Experimental	387.4286	0.06	8.7775
Predicted	395.510	0.05	8.595
Error (%)	-2.086	+16.67	+2.079

The error analysis was computed as presented in equation 4.5.

$$Error(\%) = \frac{|\sigma E - \sigma P|}{\sigma E} \times 100\% \quad (4.5)$$

Where σ_P is the predicted value and σ_E is the experimental value.

Table 4.8 presents low percentage error for the models for porosity, surface roughness and microhardness of 16.67%, 2.079%, and 2.086 % respectively. The optimized specimen exhibits fine dendritic structures, as depicted in Figure 4.19.

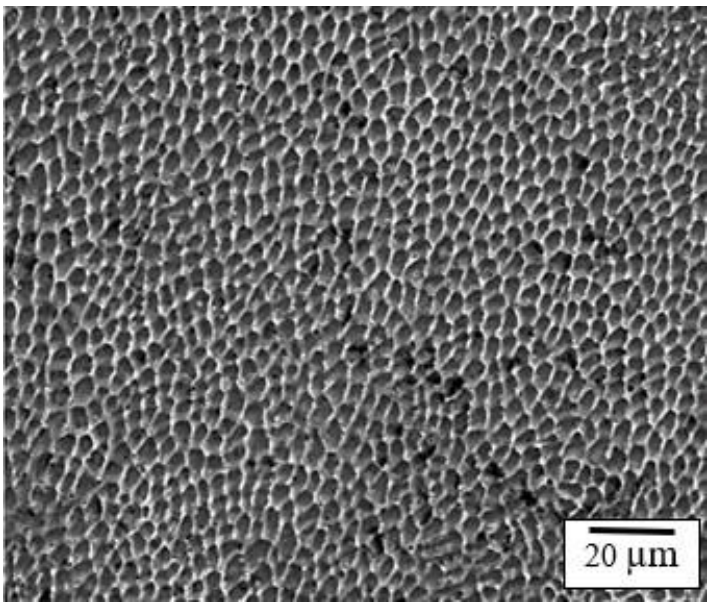

Figure 4.19: SEM Micrograph of the Optimized Sample.

4.6 X-Ray Diffraction and Wear Rate

The XRD pattern of the samples, shown in Figure 4.20, reveals sharp peaks correlating with the phases of CoCrMo alloys that include the γ face-centered cubic (FCC) phase and ϵ hexagonal close-packed (HCP) phase (AlMangour, Luqman, Grzesiak, Al-Harbi, & Ijaz, 2020). The ϵ-HCP phase is thermodynamically stable at room temperature while the γ- FCC phase is stable at high temperatures above 1173 K. Nevertheless, γ- FCC to ϵ-HCP phase transformation is associated with slow nucleation, making it a slow phase transformation process. There was no significant deviation between the XRD peaks of heat-treated and as-built specimens.

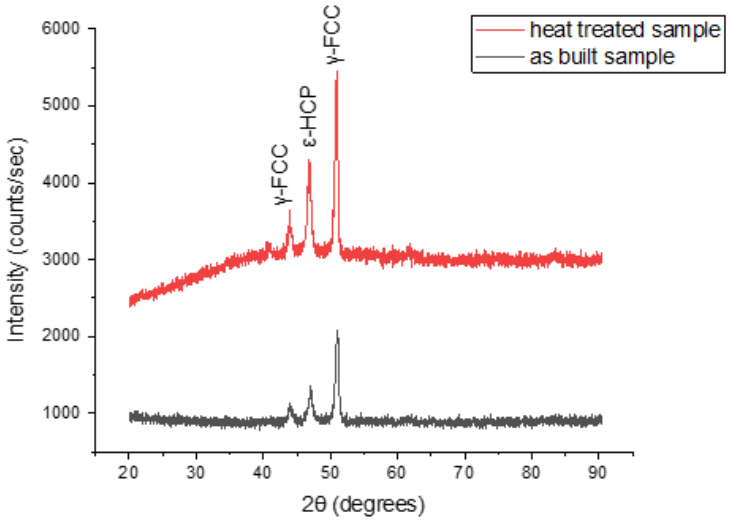

Figure 4.20: XRD Pattern Obtained on As-Built and Heat-Treated LENS-Processed CoCrMo Samples

Wear tests conducted on the optimum sample indicate that the coefficient of friction (COF) of heat-treated samples (COF=0.255148) is slightly less than that of the as-built samples (COF=0.256242), which show better wear performance. This confirms that heat treatment has an influence on COF which is similar to the findings by Karabulut et al. (Karabulut, Tascioglu, & Kaynak, 2021). The wear volume of the heat-treated samples (0.049625 mm^3) was lower compared to the as-built samples (0.074865 mm^3). The specific wear rate of as-built samples (3.11946 x 10^{-4} $mm^3N^{-1}m^{-}1$) was higher compared to the heat-treated samples (2.067595x10^{-4} $mm^3N^{-1}m^{-1}$). The improvement in wear resistance after heat treatment could be attributed to the increase in the fraction of the ϵ-HCP phase (Li, Wang, Lou, Xia, & Fang, 2020). Figure 4.21 presents the SEM micrograph of the worn surface of the heat-treated sample, which shows abrasive wear behavior and several scratches. Abrasive wear could be attributed to the heat treatment process, which could have resulted in a coarse microstructure (Özer & Kisasöz, 2022). The coarsening of the microstructure can be due to the annealing effects during heat treatment.

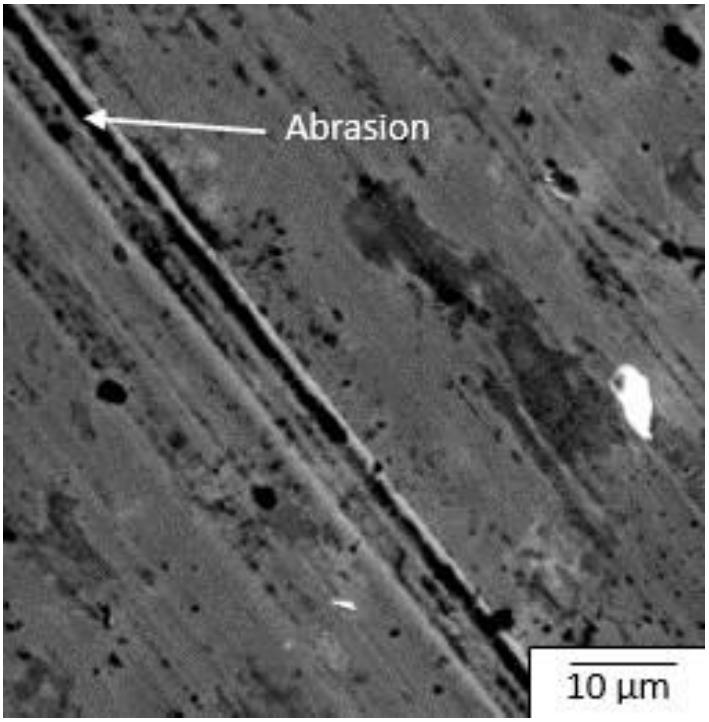

Figure 4.21: SEM Image of the Wear Scars

CHAPTER FIVE

CONCLUSIONS AND RECOMMENDATIONS

5.1 Conclusions

Response surface methodology was used to investigate the impact of laser power, powder feed rate, and scan speed on the porosity, microhardness, and surface roughness of CoCrMo alloy manufactured by LENS. In addition, validation tests were executed to verify the input parameters predicted from this work. The following was deduced from this work:

i. Analysis of variance (ANOVA) indicates that powder feed rate and scan speed significantly influence microhardness, whereas laser power was not statistically significant. The influence of the input factors on quality properties is as follows: laser power< powder feed rate < scan speed.
ii. Scan speed and powder feed rate have a direct relationship with porosity. The impact of laser power on porosity was not significant. Comparing the F-values of scan speed and feed rate, the feed rate has the least influence on porosity.
iii. An increase in laser power to 300 W led to a decrease in surface roughness. On the contrary, an increase in scan speed resulted in an increase in surface roughness up to a value of 7.5 mms^{-1}, above which the surface roughness began to decrease. The feed rate had no significant influence on surface roughness.
iv. The optimum process parameters predicted at a desirability value of 0.846 were a powder feed rate of 4.748 $gmin^{-}1$, laser power of 386.896 W, and scan speed of 5.3 mms^{-1}. The responses obtained via the validation test were microhardness: 387.4286 HV, porosity: 0.06 %, and surface roughness: 8.7775 µm.
v. Reliable mathematical models that can be utilized to predict the microhardness, porosity, and surface roughness for laser engineered net shaped cobalt-chromium-molybdenum alloys were developed.

5.2 Recommendations

The recommendations for future research include:

i. Further study should be conducted on optimizing the process parameters of other biomaterials for mechanical and microstructural comparison for dental implant applications.
ii. Further study should be carried out to improve the surface roughness of LENS fabricated CoCrMo alloy using postprocessing methods such as laser polishing.
iii. Further study should be conducted to fabricate an actual dental implant using LENS.

REFERENCES

Abdul Patar, M. A., Suhaimi, M. A., Sharif, S., Mohruni, A. S., & Kejia, Z. (2024). Micro Drilling 3D Printed Cobalt Chromium Molybdenum for Biomedical Applications: An Experimental Study on the Tool Wear and Machinability. *International Journal of Precision Engineering and Manufacturing*, 1–13.

Abdulwahab, M., Enechukwu, O., Aigbodion, V. S., & Yaro, S. A. (2015). Mitigation of the wear failure of Ti-6Al-4V dental biomedical implant by isothermal treatment. *Journal of Failure Analysis and Prevention*, *15*, 952–957.

Acharya, S., Soni, R., Suwas, S., & Chatterjee, K. (2021). Additive manufacturing of Co–Cr alloys for biomedical applications: A concise review. *Journal of Materials Research*, *36*, 3746–3760.

Agrawal, R., & Vinodh, S. (2022). Project selection for sustainable additive manufacturing: A case study. *Green Production Engineering and Management*, 61–80.

Ahn, D.-G. (2021). Directed energy deposition (DED) process: State of the art. *International Journal of Precision Engineering and Manufacturing-Green Technology*, *8*, 703–742.

Akinlabi, E. T., Okamoto, Y., Maina, M. R., Akinlabi, S. A., Pityana, S., Tlotleng, M., . . . Mahamood, R. M. (2019). Laser Metal Deposition of Titanium Alloy (Ti6Al4V): A Review. *2019 International Conference on Engineering, Science, and Industrial Applications (ICESI)*, (pp. 1–5).

AlMangour, B., Luqman, M., Grzesiak, D., Al-Harbi, H., & Ijaz, F. (2020). Effect of processing parameters on the microstructure and mechanical properties of Co–Cr–Mo alloy fabricated by selective laser melting. *Materials Science and Engineering: A*, *792*, 139456.

Amirov, N., & Vakhshouri, A. R. (2020). Numerical modeling and optimization of product selectivity and catalyst activity in Fischer-Tropsch synthesis via response surface methodology: Cobalt carbide particle size and H2/CO ratio effects. *International Journal of Hydrogen Energy*, *45*, 31913–31925.

An, C., Zhang, J. S., Zhang, Y. M., Lv, D. X., & Ruan, L. (2018). Experimental study on density and pore defect of cobalt-chromium alloy manufactured by selective laser melting. *IOP Conference Series: Materials Science and Engineering, 382*, p. 022082.

Anderson, T. W., & Finn, J. D. (2012). *The new statistical analysis of data.* Springer Science and Business Media.

Aqilah, D. N., Sayuti, A. K., Farazila, Y., Suleiman, D. Y., Amirah, M. A., & Izzati, W. B. (2018). Effects of process parameters on the surface roughness of stainless steel 316L parts produced by selective laser melting. *Journal of Testing and Evaluation, 46,* 1673–1683.

Aramian, A., Razavi, N., Sadeghian, Z., & Berto, F. (2020). A review of additive manufacturing of cermets. *Additive Manufacturing, 33,* 101130.

Arif, Z. U., Khalid, M. Y., Noroozi, R., Hossain, M., Shi, H. H., Tariq, A., . . . Umer, R. (2023). Additive manufacturing of sustainable biomaterials for biomedical applications. *Asian Journal of Pharmaceutical Sciences*, 100812.

Armentia, M., Abasolo, M., Coria, I., & Albizuri, J. (2020). Fatigue design of dental implant assemblies: a nominal stress approach. *Metals, 10,* 744.

Arthur, K. P., Baloyi, P., Moller, H., & Pityana, S. L. (2016). Influence of process parameters on layer build-up and microstructure of Ti6Al4V (ELI) alloy on the optomec LENS.

Arthur, N. K. (2019). Laser based manufacturing of Ti6Al4V: A comparison of LENS and selective laser melting. *Materials Science Forum, 950*, pp. 44–49.

Arthur, N. K., Malabi, K. P., Baloyi, P., Moller, H., & Pityana, S. L. (2016). Influence of process parameters on layer build-up and microstructure of Ti6Al4V (ELI) alloy on the optomec LENS.

Asherloo, M., Hwang, J., Leroux, R., Wu, Z., Fezzaa, K., Paliwal, M., . . . Mostafaei, A. (2023). Understanding process-microstructure-property relationships in laser powder bed fusion of non-spherical Ti-6Al-4V powder. *Materials Characterization, 198,*

112757.

Asiltürk, I., Neşeli, S., & Ince, M. A. (2016). Optimisation of parameters affecting surface roughness of Co28Cr6Mo medical material during CNC lathe machining by using the Taguchi and RSM methods. *Measurement, 78*, 120–128.

Avila, J. D., Bose, S., & Bandyopadhyay, A. (2018). Additive manufacturing of titanium and titanium alloys for biomedical applications. In *Titanium in Medical and Dental Applications* (pp. 325–343). Elsevier.

Awad, A., Fina, F., Goyanes, A., Gaisford, S., & Basit, A. W. (2020). 3D printing: Principles and pharmaceutical applications of selective laser sintering. *International Journal of Pharmaceutics, 586*, 119594.

Baciu, E.-R., Cimpoeșu, R., Vițalariu, A., Baciu, C., Cimpoeșu, N., Sodor, A., . . . Murariu, A. (2021). Surface Analysis of 3D (SLM) Co–Cr–W Dental Metallic Materials. *Applied Sciences, 11*, 255.

Bandyopadhyay, A., Shivaram, A., Isik, M., Avila, J. D., Dernell, W. S., & Bose, S. (2019). Additively manufactured calcium phosphate reinforced CoCrMo alloy: Bio-tribological and biocompatibility evaluation for load-bearing implants. *Additive manufacturing, 28*, 312–324.

Bandyopadhyay, A., Traxel, K. D., Lang, M., Juhasz, M., Eliaz, N., & Bose, S. (2022). Alloy design via additive manufacturing: Advantages, challenges, applications and perspectives. *Materials Today*.

Barazanchi, A., Li, K. C., Al-Amleh, B., Lyons, K., & Waddell, J. N. (2017). Additive technology: update on current materials and applications in dentistry. *Journal of Prosthodontics, 26*, 156–163.

Bastola, N., Jahan, M. P., Rangasamy, N., & Rakurty, C. S. (2023). A review of the residual stress generation in metal additive manufacturing: Analysis of cause, measurement, effects, and prevention. *Micromachines, 14*, 1480.

Bellini, C., Berto, F., Di Cocco, V., Iacoviello, F., Mocanu, L. P., & Razavi, N. (2021). Additive manufacturing processes for metals and effects of defects on mechanical strength: a review. *Procedia Structural Integrity*, *33*, 498–508.

Benarji, K., Ravi Kumar, Y., Jinoop, A. N., Paul, C. P., & Bindra, K. S. (2021). Effect of heat-treatment on the microstructure, mechanical properties and corrosion behaviour of SS 316 structures built by laser directed energy deposition based additive manufacturing. *Metals and Materials International*, *27*, 488–499.

Brennan, M. C., Keist, J. S., & Palmer, T. A. (2021). Defects in metal additive manufacturing processes. *Defects in metal additive manufacturing processes*. Springer.

Calignano, F., Manfredi, D., Ambrosio, E. P., Iuliano, L., & Fino, P. (2013). Influence of process parameters on surface roughness of aluminum parts produced by DMLS. *The International Journal of Advanced Manufacturing Technology*, *67*, 2743–2751.

Chandrasekaran, M. (2019). Forging of metals and alloys for biomedical applications. In *Metals for Biomedical Devices* (pp. 293–310). Elsevier.

Chen, H., Sun, L., Li, L., Zhu, W., Gong, Q., Castro, R. D., & Rushworth, A. (2024). Microstructure evolution and grain growth characteristics of IN625 in laser surface melting: Effects of laser power and scanning speed. *Journal of Materials Processing Technology*, *331*, 118525.

Chen, Z., Cao, S., Wu, X., & Davies, C. H. (2019). Surface roughness and fatigue properties of selective laser melted Ti–6Al–4V alloy. In *Additive manufacturing for the aerospace industry* (pp. 283–299). Elsevier.

Chen, Z., Lu, Y., Luo, F., Zhang, S., Wei, P., Yao, S., & Wang, Y. (2022). Effect of laser scanning speed on the microstructure and mechanical properties of laser-powder-bed-fused K418 nickel-based alloy. *Materials*, *15*, 3045.

Chiba, A., Kumagai, K., Nomura, N., & Miyakawa, S. (2007). Pin-on-disk wear behavior in a like-on-like configuration in a biological environment of high carbon cast and low carbon forged Co–29Cr–6Mo alloys. *Acta Materialia*, *55*, 1309-1318.

doi:https://doi.org/10.1016/j.actamat.2006.10.005

Chong, M. S., Teo, Y. E., & Teoh, S. H. (2012). Fatigue failure of materials for medical devices. *Degradation of Implant Materials*, 303–328.

Chowdhury, S., Yadaiah, N., Prakash, C., Ramakrishna, S., Dixit, S., Gupta, L. R., & Buddhi, D. (2022). Laser powder bed fusion: a state-of-the-art review of the technology, materials, properties and defects, and numerical modelling. *Journal of Materials Research and Technology, 20*, 2109–2172.

Christiansen, R. J., Münch, H. J., Bonefeld, C. M., Thyssen, J. P., Sloth, J. J., Geisler, C., . . . Jakobsen, S. S. (2019). Cytokine profile in patients with aseptic loosening of total hip replacements and its relation to metal release and metal allergy. *Journal of Clinical Medicine, 8*, 1259.

Cosma, C., Moldovan, M., Simion, M., & Balc, N. (2022). Impact of laser parameters on additively manufactured cobalt-chromium restorations. *The Journal of Prosthetic Dentistry, 128*, 421–429.

Cutolo, A., Neirinck, B., Lietaert, K., de Formanoir, C., & Van Hooreweder, B. (2018). Influence of layer thickness and post-process treatments on the fatigue properties of CoCr scaffolds produced by laser powder bed fusion. *Additive Manufacturing, 23*, 498–504.

Dank, A., Aartman, I. H., Wismeijer, D., & Tahmaseb, A. (2019). Effect of dental implant surface roughness in patients with a history of periodontal disease: A systematic review and meta-analysis. *International journal of implant dentistry, 5*, 1–11.

Dass, A., & Moridi, A. (2019). State of the art in directed energy deposition: From additive manufacturing to materials design. *Coatings, 9*, 418.

Dejob, L., Attik, N., Tadier, S., Gaillard, C., Toury, B., & Salles, V. (2022). Nitrate-Free Synthesis and Electrospinning of Carbonated Hydroxyapatite Coatings on TA6V Implants. *Advanced Materials Interfaces, 9*, 2102342.

Dong, X., Zhou, Y., Sun, Q., Qu, Y., Shi, H., Liu, W., . . . others. (2020). Fatigue behavior of biomedical Co–Cr–Mo–W alloy fabricated by selective laser melting. *Materials Science and Engineering: A, 795*, 140000.

Duan, C., Zhang, Y., & Luo, X. (2021). Effect of Powder Feeding Rate on the Forming Quality of Alloy by Laser Melting Deposition. *Journal of Physics: Conference Series*, *2083.*

Dutta, B. (2022). Directed Energy Deposition (DED) Technology.

Evans, R., & Gockel, J. (2021). Surface Roughness Variation in Laser Powder Bed Fusion Additive Manufacturing. *2021 International Solid Freeform Fabrication Symposium.*

Feenstra, D. R., Banerjee, R., Fraser, H. L., Huang, A., Molotnikov, A., & Birbilis, N. (2021). Critical review of the state of the art in multi-material fabrication via directed energy deposition. *Current Opinion in Solid State and Materials Science*, *25*, 100924.

Fellah, M., Hezil, N., Bouras, D., Obrosov, A., Mohammed, A. S., Montagne, A., . . . Weiß, S. (2023). Structural, mechanical and tribological performance of a nano structured biomaterial Co–Cr–Mo alloy synthesized via mechanical alloying. *Journal of Materials Research and Technology*, *25*, 2152–2165.

Fu, D., Li, X., Zhang, M., Wang, M., Zhang, Z., & Qu, S. (2020). Influence of effective laser energy on the structure and mechanical properties of laser melting deposited Ti6Al4V alloy. *Materials, 13,* 962.

Gallo, J., Goodman, S. B., Konttinen, Y. T., & Raska, M. (2013). Particle disease: biologic mechanisms of periprosthetic osteolysis in total hip arthroplasty. *Innate immunity*, *19*, 213–224.

Gallo, P., & Berto, F. (2015). Influence of surface roughness on high temperature fatigue strength and cracks initiation in 40CrMoV13. 9 notched components. *Theoretical and Applied Fracture Mechanics, 80,* 226–234.

Gan, X., Fei, G., Wang, J., Wang, Z., Lavorgna, M., & Xia, H. (2020). Powder quality and electrical conductivity of selective laser sintered polymer composite components. In

Structure and Properties of Additive Manufactured Polymer Components (pp. 149–185). Elsevier.

Ghani, S. A., Harun, W. S., Mat Taib, Z. A., Ab Rashid, F. F., Hazlen, R. M., & Omar, M. A. (2016). Finite element analysis of porous medical grade cobalt chromium alloy structures produced by selective laser melting. *Advanced Materials Research, 1133*, pp. 113–118.

Gobbi, S. J., Reinke, G., Gobbi, V. J., Rocha, Y., Sousa, T. P., & Coutinho, M. M. (2020). Biomaterial: concepts and basics properties. *Eur Int J Sci Technol, 9*, 23–42.

Goharian, A., & Abdullah, M. R. (2017). Bioinert metals (stainless steel, titanium, cobalt chromium). *Trauma Plating System. Amsterdam: Elsevier*, 115–142.

Grimaudo, N. J. (2001). Biocompatibility of nickel and cobalt dental alloys. *General dentistry, 49*, 498–503.

Grosgogeat, B., Vaicelyte, A., Gauthier, R., Janssen, C., & Le Borgne, M. (2022). Toxicological Risks of the Cobalt–Chromium Alloys in Dentistry: A Systematic Review. *Materials, 15*, 5801.

Gülcan, O., Günaydın, K., Çelik, A., & Yasa, E. (2024). Mechanical properties of laser powder bed fusion produced overhang parts with different support geometries: an experimental study. *Progress in Additive Manufacturing, 9*, 211–229.

Guoqing, Z., Junxin, L., Xiaoyu, Z., Jin, L., & Anmin, W. (2018). Effect of heat treatment on the properties of CoCrMo alloy manufactured by selective laser melting. *Journal of Materials Engineering and Performance, 27*, 2281–2287.

Hanzl, P., Zetek, M., Bakša, T., & Kroupa, T. (2015). The influence of processing parameters on the mechanical properties of SLM parts. *Procedia Engineering, 100*, 1405–1413.

Hao, L., Wang, W., Zeng, J., Song, M., Chang, S., & Zhu, C. (2023). Effect of scanning speed and laser power on formability, microstructure, and quality of 316L stainless steel prepared by selective laser melting. *Journal of Materials Research and Technology,*

25, 3189–3199.

Hardness, A. B. (1999). Standard Test Method for Microindentation Hardness of Materials. *ASTM Committee: West Conshohocken, PA, USA*, *384*, 399.

Hashmi, A. W., Mali, H. S., Meena, A., Puerta, V., & Kunkel, M. E. (2022). Surface characteristics improvement methods for metal additively manufactured parts: A review. *Advances in Materials and Processing Technologies*, 1–40.

Hashmi, S. (2014). *Comprehensive materials processing*. Newnes.

Hassanin, H., El-Sayed, M. A., Ahmadein, M., Alsaleh, N. A., Ataya, S., Ahmed, M. M., & Essa, K. (2023). Optimising surface roughness and density in titanium fabrication via laser powder bed fusion. *Micromachines*, *14*, 1642.

Haugen, H. J., & Chen, H. (2022). Is there a better biomaterial for dental implants than titanium?—A review and meta-study analysis. *Journal of Functional Biomaterials*, *13*, 46.

He, M., Chen, L., Yin, M., Xu, S., & Liang, Z. (2023). Review on magnesium and magnesium-based alloys as biomaterials for bone immobilization. *Journal of Materials Research and Technology*.

Hernandez-Rodriguez, M. A., Mercado-Solis, R. D., Presbítero, G., Lozano, D. E., Martinez-Cazares, G. M., & Bedolla-Gil, Y. (2019). Influence of boron additions and heat treatments on the fatigue resistance of CoCrMo alloys. *Materials*, *12*, 1076.

Holt, G., Murnaghan, C., Reilly, J., & Meek, R. M. (2007). The biology of aseptic osteolysis. *Clinical Orthopaedics and Related Research (1976-2007)*, *460*, 240–252.

Hong, J. H., & Yeoh, F. Y. (2020). Mechanical properties and corrosion resistance of cobalt-chrome alloy fabricated using additive manufacturing. *Materials Today: Proceedings*, *29*, 196–201.

Hong, M.-H., Min, B. K., & Kwon, T.-Y. (2016). The influence of process parameters on the surface roughness of a 3D-printed Co–Cr dental alloy produced via selective laser

melting. *Applied Sciences, 6*, 401.

Hussein, M. A., Mohammed, A. S., & Al-Aqeeli, N. (2015). Wear characteristics of metallic biomaterials: a review. *Materials, 8*, 2749–2768.

Islam, M. A., Mobarak, M. H., Rimon, M. I., Al Mahmud, M. Z., Ghosh, J., Ahmed, M. M., & Hossain, N. (2024). Additive manufacturing in polymer research: Advances, synthesis, and applications. *Polymer Testing*, 108364.

Iso, E. N. (1997). 4287–Geometrical product specifications (GPS)–Surface texture: profile method–terms, definitions and surface texture parameters. *International Organization for Standardization: Geneva, Switzerland*.

Izadi, M., Farzaneh, A., Mohammed, M., Gibson, I., & Rolfe, B. (2020). A review of laser engineered net shaping (LENS) build and process parameters of metallic parts. *Rapid Prototyping Journal*.

Jang, T.-S., Kim, D., Han, G., Yoon, C.-B., & Jung, H.-D. (2020). Powder based additive manufacturing for biomedical application of titanium and its alloys: A review. *Biomedical engineering letters, 10*, 505–516.

Jeong, J., Webster, S., Liao, S., Mogonye, J.-E., Ehmann, K., & Cao, J. (2022). Cooling rate measurement in directed energy deposition using photodiode-based planck thermometry (PDPT). *Additive Manufacturing Letters, 3*, 100101.

Jing, Y., Wang, P., & Yan, X. (2021). Effect of Process Parameters and Layer Thickness on the Quality and Performance of Ti-6Al-4V Fabricated by Selective Laser Melting. *Coatings, 11*, 1323.

Kajima, Y., Takaichi, A., Nakamoto, T., Kimura, T., Yogo, Y., Ashida, M., . . . others. (2016). Fatigue strength of Co–Cr–Mo alloy clasps prepared by selective laser melting. *Journal of the mechanical behavior of biomedical materials, 59*, 446–458.

Karabulut, Y., Tascioglu, E., & Kaynak, Y. (2021). Heat treatment temperature-induced microstructure, microhardness and wear resistance of Inconel 718 produced by

selective laser melting additive manufacturing. *Optik, 227*, 163907.

Karimi, J., Suryanarayana, C., Okulov, I., & Prashanth, K. G. (2021). Selective laser melting of Ti6Al4V: Effect of laser re-melting. *Materials Science and Engineering: A, 805*, 140558.

Kasperovich, G., Haubrich, J., Gussone, J., & Requena, G. (2016). Correlation between porosity and processing parameters in TiAl6V4 produced by selective laser melting. *Materials and Design, 105*, 160–170.

Kassapidou, M., Hjalmarsson, L., Johansson, C. B., Johansson, P. H., Morisbak, E., Wennerberg, A., & Stenport, V. F. (2020). Cobalt–Chromium alloys fabricated with four different techniques: Ion release, toxicity of released elements and surface roughness. *Dental Materials, 36*, e352–e363.

Khuri, A. I., & Mukhopadhyay, S. (2010). Response surface methodology. *Wiley Interdisciplinary Reviews: Computational Statistics, 2*, 128–149.

Kicsi, A., Cojocaru, C., Macoveanu, M., & Bilba, D. (2010). Response surface methodology applied for zinc removal from aqueous solutions using sphagnum peat moss as sorbent. *Journal of Environmental Protection and Ecology, 11*, 614–622.

Kilickap, E. (2010). Optimization of cutting parameters on delamination based on Taguchi method during drilling of GFRP composite. *Expert systems with applications, 37*, 6116–6122.

Kim, F. H., Kim, F. H., & Moylan, S. P. (2018). *Literature review of metal additive manufacturing defects.* US Department of Commerce, National Institute of Standards and Technology.

Kiran, A. S., & Ramakrishna, S. (2021). *An Introduction to Biomaterials Science and Engineering.* World Scientific.

Kircher, R. S., Christensen, A. M., & Wurth, K. W. (2009). Electron beam melted (EBM) Co-Cr-Mo alloy for orthopaedic implant applications.

Kistler, N. A., Corbin, D. J., Nassar, A. R., Reutzel, E. W., & Beese, A. M. (2019). Effect of processing conditions on the microstructure, porosity, and mechanical properties of Ti-6Al-4V repair fabricated by directed energy deposition. *Journal of Materials Processing Technology, 264*, 172–181.

Ko, K.-H., Kang, H.-G., Huh, Y.-H., Park, C.-J., & Cho, L.-R. (2021). Effects of heat treatment on the microstructure, residual stress, and mechanical properties of Co–Cr alloy fabricated by selective laser melting. *Journal of the Mechanical Behavior of Biomedical Materials*, 105051.

Konieczny, B., Szczesio-Wlodarczyk, A., Sokolowski, J., & Bociong, K. (2020). Challenges of Co–Cr alloy additive manufacturing methods in dentistry—the current state of knowledge (systematic review). *Materials, 13*, 3524.

Kumar, P., Farah, J., Akram, J., Teng, C., Ginn, J., & Misra, M. (2019). Influence of laser processing parameters on porosity in Inconel 718 during additive manufacturing. *The International Journal of Advanced Manufacturing Technology, 103*, 1497–1507.

Kumar, S. A., & Prasad, R. V. (2021). Basic principles of additive manufacturing: different additive manufacturing technologies. In *Additive manufacturing* (pp. 17–35). Elsevier.

Kumar, S. T., Devi, S. P., Krithika, C., & Raghavan, R. N. (2020). Review of metallic biomaterials in dental applications. *Journal of Pharmacy and Bioallied Sciences, 12*.

Kunrath, M. F. (2020). Customized dental implants: Manufacturing processes, topography, osseointegration and future perspectives of 3D fabricated implants. *Bioprinting, 20*, e00107.

Łazińska, M., Durejko, T., Czujko, T., & Bojar, Z. (2018). The effect of the traverse feed rate on the microstructure and mechanical properties of laser Deposited Fe3Al (Zr, B) intermetallic alloy. *Materials, 11*, 792.

Lee, S., Shao, S., Wells, D. N., Zetek, M., Kepka, M., & Shamsaei, N. (2022). Fatigue behavior and modeling of additively manufactured IN718: The effect of surface treatments and surface measurement techniques. *Journal of Materials Processing*

Technology, 302, 117475.

Lee, W.-F., Wang, J.-C., Hsu, C.-Y., & Peng, P.-W. (2020). Microstructure, mechanical properties, and retentive forces of cobalt-chromium removable partial denture frameworks fabricated by selective laser melting followed by heat treatment. *The Journal of Prosthetic Dentistry*.

Li, H., Wang, M., Lou, D., Xia, W., & Fang, X. (2020). Microstructural features of biomedical cobalt–chromium–molybdenum (CoCrMo) alloy from powder bed fusion to aging heat treatment. *Journal of Materials Science and Technology, 45*, 146–156.

Li, J., Hu, J., Zhu, Y., Yu, X., Yu, M., & Yang, H. (2020). Surface roughness control of root analogue dental implants fabricated using selective laser melting. *Additive Manufacturing, 34*, 101283.

Li, J., Ren, H., Liu, C., & Shang, S. (2019). The effect of specific energy density on microstructure and corrosion resistance of CoCrMo alloy fabricated by laser metal deposition. *Materials, 12*, 1321.

Li, L., Meng, X., Huang, S., Wang, H., Li, P., & Zhou, J. (2022). Investigating the effect of the scanning speed on the characteristics of Al-Li alloy fabricated by selective laser melting. *Journal of Manufacturing Processes, 75*, 719–728.

Li, P., Warner, D. H., Fatemi, A., & Phan, N. (2016). Critical assessment of the fatigue performance of additively manufactured Ti–6Al–4V and perspective for future research. *International Journal of Fatigue, 85*, 130–143.

Li, Y., Hu, Y., Cong, W., Zhi, L., & Guo, Z. (2017). Additive manufacturing of alumina using laser engineered net shaping: Effects of deposition variables. *Ceramics international, 43*, 7768–7775.

Li, Y., Yang, H., Lin, X., Huang, W., Li, J., & Zhou, Y. (2003). The influences of processing parameters on forming characterizations during laser rapid forming. *Materials Science and Engineering: A, 360*, 18–25.

Lin, M.-C., Qiu, G.-P., Zhou, X. H., & Chen, C.-N. (2020). Using Taguchi and neural network approaches in the optimum design of product development process. *International Journal of Computer Integrated Manufacturing, 33*, 343–359.

Lin, P.-Y., Shen, F.-C., Wu, K.-T., Hwang, S.-J., & Lee, H.-H. (2020). Process optimization for directed energy deposition of SS316L components. *The International Journal of Advanced Manufacturing Technology, 111*, 1387–1400.

Liu, M., & Kuttolamadom, M. (2021). Characterization of Co-Cr-Mo Alloys Manufacturing via Directed Energy Deposition. *International Manufacturing Science and Engineering Conference, 85062*.

Liu, Y., Ding, Y., Yang, L., Sun, R., Zhang, T., & Yang, X. (2021). Research and progress of laser cladding on engineering alloys: A review. *Journal of Manufacturing Processes, 66*, 341–363.

Liverani, E., Fortunato, A., Leardini, A., Belvedere, C., Siegler, S., Ceschini, L., & Ascari, A. (2016). Fabrication of Co–Cr–Mo endoprosthetic ankle devices by means of Selective Laser Melting (SLM). *Materials and Design, 106*, 60–68.

Long, H., Li, T., Shi, H., Gui, Y., & Qiu, C. (2023). Experimental Study of Laser Cladding Ni-Based Coating Based on Response Surface Method. *Coatings, 13*, 1216.

Ma, H. Y., Wang, J. C., Qin, P., Liu, Y. J., Chen, L. Y., Wang, L. Q., & Zhang, L. C. (2023). Advances in additively manufactured titanium alloys by powder bed fusion and directed energy deposition: Microstructure, defects, and mechanical behavior. *Journal of Materials Science and Technology*.

Maamoun, A. H., Xue, Y. F., Elbestawi, M. A., & Veldhuis, S. C. (2018). Effect of selective laser melting process parameters on the quality of al alloy parts: Powder characterization, density, surface roughness, and dimensional accuracy. *Materials, 11*, 2343.

Mahajan, A., Singh, G., & Devgan, S. (2023). Additive manufacturing of metallic biomaterials: A concise review. *Archives of Civil and Mechanical Engineering, 23*,

187.

Mahamood, R. M., & Akinlabi, E. T. (2017). Scanning speed and powder flow rate influence on the properties of laser metal deposition of titanium alloy. *The International Journal of Advanced Manufacturing Technology*, *91*, 2419–2426.

Mahamood, R. M., Akinlabi, E. T., Shukla, M., & Pityana, S. (2013). Characterizing the effect of laser power density on microstructure, microhardness, and surface finish of laser deposited titanium alloy. *Journal of Manufacturing Science and Engineering*, *135*, 064502.

Mahamood, R. M., Akinlabi, E. T., Shukla, M., & Pityana, S. (2014). Revolutionary Additive Manufacturing: An Overview. *Lasers in Engineering (Old City Publishing)*, *27*.

Maharubin, S., Hu, Y., Sooriyaarachchi, D., Cong, W., & Tan, G. Z. (2019). Laser engineered net shaping of antimicrobial and biocompatible titanium-silver alloys. *Materials Science and Engineering: C*, *105*, 110059.

Maina, M. R. (2018). Laser Additive Manufacturing of Titanium-Based Implants: A Review. *Biomedical Engineering: Concepts, Methodologies, Tools, and Applications*, 1028–1037.

Malikongwa, K., Tlotleng, M., & Olakanmi, E. O. (2021). Optimisation of the wear resistance properties of laser cladded T-800 coatings. *The International Journal of Advanced Manufacturing Technology*, *114*, 481–496.

Mallik, M. K., Rao, C. S., & others. (2014). Effect of heat treatment on hardness of Co-Cr-Mo alloy deposited with laser engineered net shaping. *Procedia Engineering*, *97*, 1718–1723.

Mantrala, K. M., Das, M., Balla, V. K., Rao, C. S., & Kesava Rao, V. V. (2015). Additive manufacturing of Co-Cr-Mo alloy: influence of heat treatment on microstructure, tribological, and electrochemical properties. *Frontiers in Mechanical Engineering*, *1*, 2.

Mantrala, K. M., Das, M., Balla, V. K., Rao, C. S., & Rao, V. K. (2014). Laser-deposited CoCrMo alloy: Microstructure, wear, and electrochemical properties. *Journal of Materials Research, 29*, 2021–2027.

Mantrala, K. M., Rao, C. S., Rao, V. K., & Munaf, S. A. (2018). Effect of process parameters on the tensile properties of LENS deposited Co-Cr-Mo alloy. *International Journal of Manufacturing Technology and Management, 32*, 509–516.

Maodzeka, D. K., Olakanmi, E. O., Mosalagae, M., Hagedorn-Hansen, D., & Pityana, S. L. (2023). Hybrid optimisation studies on the microstructural properties and wear resistance of maraging steel 1.2709 parts produced by laser powder bed fusion. *Optics and Laser Technology, 159*, 108914.

Marks, P. (2011). 3D printing takes off with the world's first printed plane. *3D printing takes off with the world's first printed plane*. Elsevier.

Mehkri, S., Abishek, N. R., Sumanth, K. S., & Rekha, N. (2021). Study of the Tribocorrosion occurring at the implant and implant alloy Interface: Dental implant materials. *Materials Today: Proceedings, 44*, 157–165.

Mehrpouya, M., Tuma, D., Vaneker, T., Afrasiabi, M., Bambach, M., & Gibson, I. (2022). Multimaterial powder bed fusion techniques. *Rapid prototyping journal, 28*, 1–19.

Milošev, I. (2012). CoCrMo alloy for biomedical applications. In *Biomedical Applications* (pp. 1–72). Springer.

Minnath, M. A. (2018). Metals and alloys for biomedical applications. In *Fundamental Biomaterials: Metals* (pp. 167–174). Elsevier.

Monroy, K. P., Delgado, J., Sereno, L., Ciurana, J., & Hendrichs, N. J. (2014). Effects of the selective laser melting manufacturing process on the properties of CoCrMo single tracks. *Metals and Materials International, 20*, 873–884.

Mrdak, M., Medjo, B., Veljić, D., Arsić, M., & Rakin, M. (2019). The influence of powder feed rate on mechanical properties of atmospheric plasma spray (APS) Al-12Si

coating. *Reviews on Advanced Materials Science, 58*, 75–81.

Munir, K., Biesiekierski, A., Wen, C., & Li, Y. (2020). Selective laser melting in biomedical manufacturing. *Manufacturing and Materials Processing*, 235–269.

Najmon, J. C., Raeisi, S., & Tovar, A. (2019). Review of additive manufacturing technologies and applications in the aerospace industry. *Additive manufacturing for the aerospace industry*, 7–31.

Narasimharaju, S. R., Liu, W., Zeng, W., See, T. L., Scott, P., Jiang, X., & Lou, S. (2024). Surface texture characterisation of longitudinal and latitudinal external and internal surfaces of laser powder bed fusion processed bespoke ball artefact. *Journal of Manufacturing Processes, 116*, 120–148.

Nganbe, M., March, G. M., Kim, P. R., & Beaulé, P. E. (2014). Unusual fatigue failure of cobalt chrome alloy cementless femoral stem: implant retrieval and biomechanical analysis. *Journal of Medical and Biological Engineering, 34*, 426–430.

Ngoveni, A. S., Popoola, A. P., Arthur, N. K., & Pityana, S. L. (2019). Residual stress modelling and experimental analyses of Ti6Al4V ELI additive manufactured by laser engineered net shaping. *Procedia Manufacturing, 35*, 1001–1006.

Noll, I., Bartel, T., & Menzel, A. (2020). A computational phase transformation model for selective laser melting processes. *Computational Mechanics, 66*, 1321–1342.

Nuñez, L., Downey, C. M., van Rooyen, I. J., Charit, I., & Maughan, M. R. (2024). Analysis of surface roughness in metal directed energy deposition. *The International Journal of Advanced Manufacturing Technology*, 1–20.

Olakanmi, E. O., Cochrane, R. F., & Dalgarno, K. W. (2015). A review on selective laser sintering/melting (SLS/SLM) of aluminium alloy powders: Processing, microstructure, and properties. *Progress in Materials Science, 74*, 401–477.

Olakanmi, E. O., Hoosain, S., Lawal, S. A., & Pityana, S. L. (2022). Process and materials design for laser cladded inconel-625/tungsten carbide wear-resistant composite

coatings.

Olakanmi, E. O., Nyadongo, S. T., Malikongwa, K., Lawal, S. A., Botes, A., & Pityana, S. L. (2019). Multi-variable optimisation of the quality characteristics of fiber-laser cladded Inconel-625 composite coatings. *Surface and Coatings Technology, 357*, 289–303.

Oliveira, T. T., & Reis, A. C. (2019). Fabrication of dental implants by the additive manufacturing method: A systematic review. *The Journal of Prosthetic Dentistry, 122*, 270–274.

Özer, G., & Kisasöz, A. (2022). The role of heat treatments on wear behaviour of 316L stainless steel produced by additive manufacturing. *Materials Letters, 327*, 133014.

Paital, S. R., & Dahotre, N. B. (2008). Review of laser based biomimetic and bioactive Ca–P coatings. *Materials Science and Technology, 24*, 1144–1161.

Patel, N. S., Parihar, P. L., & Makwana, J. S. (2021). Parametric optimization to improve the machining process by using Taguchi method: A review. *Materials Today: Proceedings, 47*, 2709–2714.

Pegues, J. W., Shamsaei, N., Roach, M. D., & Williamson, R. S. (2019). Fatigue life estimation of additive manufactured parts in the as-built surface condition. *Material Design and Processing Communications, 1*, e36.

Phala, M. F., Popoola, A. P., Tlotleng, M., & Pityana, S. L. (2018). Effect of laser scanning speed on surface properties of Ti-Si laser clad intermetallic coatings fabricated on Ti-6Al-4V alloy. *International Journal of Microstructure and Materials Properties, 13*, 331–343.

Pimenta, A. R., Tavares, S. S., Dias, D. F., Correa, S. R., Sobreiro, A. L., & Diniz, M. G. (2021). Failure analysis of a titanium hip prosthesis. *Journal of Failure Analysis and Prevention, 21*, 28–35.

Piscopo, G., & Iuliano, L. (2022). Current research and industrial application of laser powder directed energy deposition. *The International Journal of Advanced Manufacturing*

Technology, 119, 6893–6917.

Piscopo, G., Salmi, A., & Atzeni, E. (2024). Investigation of dimensional and geometrical tolerances of laser powder directed energy deposition process. *Precision Engineering, 85*, 217–225.

Pothala, S., & Raju, M. J. (2023). Recent advances of metallic bio-materials in additive manufacturing in biomedical implants -A review. *Materials Today: Proceedings*.

Pramanik, A., Dixit, A. R., Chattopadhyaya, S., Uddin, M. S., Dong, Y., Basak, A. K., & Littlefair, G. (2017). Fatigue life of machined components. *Advances in Manufacturing, 5*, 59–76.

Prashanth, K. G. (2020). Selective laser melting: Materials and applications. *Selective laser melting: Materials and applications, 4*, 13. Multidisciplinary Digital Publishing Institute.

Pritchett, J. W. (2012). Adverse reaction to metal debris: metallosis of the resurfaced hip. *Current Orthopaedic Practice, 23*, 50–58.

Pupo, Y., Monroy, K. P., & Ciurana, J. (2015). Influence of process parameters on surface quality of CoCrMo produced by selective laser melting. *The International Journal of Advanced Manufacturing Technology, 80*, 985–995.

Radha, R., & Sreekanth, D. (2017). Insight of magnesium alloys and composites for orthopedic implant applications–A review. *Journal of magnesium and alloys*, *5*, 286–312.

Raghupatruni, P., & Kumar, S. A. (2023). Review of Microstructure and Mechanical properties of materials manufactured by direct energy deposition. *Advances in Metal Additive Manufacturing*, 161–178.

Razavi, S. M., Avanzini, A., Cornacchia, G., Giorleo, L., & Berto, F. (2021). Effect of heat treatment on fatigue behavior of as-built notched Co-Cr-Mo parts produced by Selective Laser Melting. *International Journal of Fatigue, 142*, 105926.

Razavi, S. M., Bordonaro, G. G., Ferro, P., Torgersen, J., & Berto, F. (2018). Fatigue behavior of porous Ti-6Al-4V made by laser-engineered net shaping. *Materials, 11*, 284.

Revankar, G. D., Shetty, R., Rao, S. S., & Gaitonde, V. N. (2017). Wear resistance enhancement of titanium alloy (Ti–6Al–4V) by ball burnishing process. *Journal of Materials Research and Technology*, *6*, 13–32.

Revathi, A., Mitun, D., Balla, V. K., Dwaipayan, S., Devika, D., & Manivasagam, G. (2019). Surface properties and cytocompatibility of Ti-6Al-4V fabricated using Laser Engineered Net Shaping. *Materials Science and Engineering: C, 100*, 104–116.

Revilla-León, M., Meyer, M. J., & Özcan, M. (2019). Metal additive manufacturing technologies: literature review of current status and prosthodontic applications. *Int J Comput Dent*, *22*, 55–67.

Riza, S. H., Masood, S. H., & Wen, C. (2014). Laser-assisted additive manufacturing for metallic biomedical scaffolds. *Comprehensive Materials Processing, 10*, 285–301.

Saha, S., & Roy, S. (2023). Metallic Dental Implants Wear Mechanisms. *Materials, and Manufacturing Processes: A Literature Review. Materials*, *16*, 161.

Sahoo, P., Das, S. K., & Davim, J. P. (2019). Tribology of materials for biomedical applications. In *Mechanical Behaviour of Biomaterials* (pp. 1–45). Elsevier.

Saidi, R., Fathallah, B. B., Mabrouki, T., Belhadi, S., & Yallese, M. A. (2019). Modeling and optimization of the turning parameters of cobalt alloy (Stellite 6) based on RSM and desirability function. *The International Journal of Advanced Manufacturing Technology*, *100*, 2945–2968.

Salmi, M. (2021). Additive manufacturing processes in medical applications. *Materials*, *14*, 191.

Sanaei, N., & Fatemi, A. (2020). Analysis of the effect of surface roughness on fatigue performance of powder bed fusion additive manufactured metals. *Theoretical and Applied Fracture Mechanics*, *108*, 102638.

Santos, L. M., Borrego, L. P., Ferreira, J. A., De Jesus, J., Costa, J. D., & Capela, C. (2019). Effect of heat treatment on the fatigue crack growth behaviour in additive manufactured AISI 18Ni300 steel. *Theoretical and Applied Fracture Mechanics*, *102*, 10–15.

Saprykin, A. A., Sharkeev, Y. P., Saprykina, N. A., & Ibragimov, E. A. (2020). Surface formation mechanisms in selective laser melting of cobalt-chromium-molybdenum powder. *Key Engineering Materials*, *839*, pp. 73–78.

Saprykin, A. A., Sharkeev, Y. P., Saprykina, N. A., Khimich, M. A., & Ibragimov, E. A. (2021). Structure and properties of a cobalt-chromium-molybdenum alloy obtained by selective laser melting. *IOP Conference Series: Materials Science and Engineering*, *1100*, p. 012055.

Saravanan, R., Hamidon, R., Murad, N. M., & Zailani, Z. A. (2021). Machining of cobalt chromium molybdenum (CoCrMo) alloys: A review. *Intelligent Manufacturing and Mechatronics*, 413–424.

Sayed, M. A., Dawood, O. M., Elsayed, A. H., & Daoush, W. R. (2017). Application of Taguchi method in optimization of process parameters of ODS tungsten heavy alloys. *Advances in materials Research*, *6*, 079.

Schweiger, J., Güth, J.-F., Erdelt, K.-J., Edelhoff, D., & Schubert, O. (2020). Internal porosities, retentive force, and survival of cobalt–chromium alloy clasps fabricated by selective laser-sintering. *Journal of Prosthodontic Research, 64*, 210–216.

Sealy, M. P., Guo, Y. B., Caslaru, R. C., Sharkins, J., & Feldman, D. (2016). Fatigue performance of biodegradable magnesium–calcium alloy processed by laser shock peening for orthopedic implants. *International Journal of Fatigue*, *82*, 428–436.

Seki, E., Kajima, Y., Takaichi, A., Kittikundecha, N., Cho, H. H., Htat, H. L., . . . Wakabayashi, N. (2019). Effect of heat treatment on the microstructure and fatigue strength of CoCrMo alloys fabricated by selective laser melting. *Materials Letters*, *245*, 53–56.

Seshagirirao, D. V., Raju, S., & Mantrala, K. M. (2022). Tensile, hardness and metallurgical analysis of laser cured Co-Cr-Mo alloy samples. *Advances in Materials and Processing Technologies*, 1–11.

Sheshadri, R., Nagaraj, M., Lakshmikanthan, A., Chandrashekarappa, M. P., Pimenov, D. Y., Giasin, K., . . . Wojciechowski, S. (2021). Experimental investigation of selective laser melting parameters for higher surface quality and microhardness properties: taguchi and super ranking concept approaches. *Journal of Materials Research and Technology, 14*, 2586–2600.

Sing, S. L., & Yeong, W. Y. (2018). Effect of heat treatment on cobalt-chromium-molybdenum.

Singh, K., Sadeghi, F., Correns, M., & Blass, T. (2019). A microstructure based approach to model effects of surface roughness on tensile fatigue. *International Journal of Fatigue, 129*, 105229.

Singh, R., Singh, S., & Hashmi, M. S. (2016). Implant materials and their processing technologies. *Reference Module in Materials Science and Materials Engineering*.

Song, X., Zhai, W., Huang, R., Fu, J., Fu, M., & Li, F. (2020). Metal-Based 3D-Printed Micro Parts and Structures.

Souza, J. C., Henriques, M., Teughels, W., Ponthiaux, P., Celis, J.-P., & Rocha, L. A. (2015). Wear and corrosion interactions on titanium in oral environment: literature review. *Journal of Bio-and Tribo-Corrosion, 1*, 1–13.

Stamenković, D., Obradović-Đuričić, K., Rudolf, R., Bobovnik, R., & Stamenković, D. (2019). Selective laser melting and sintering technique of the cobalt-chromium dental alloy. *Srpski arhiv za celokupno lekarstvo, 147*, 664–669.

Suárez-López del Amo, F., Garaicoa-Pazmiño, C., Fretwurst, T., Castilho, R. M., & Squarize, C. H. (2018). Dental implants-associated release of titanium particles: A systematic review. *Clinical oral implants research, 29*, 1085–1100.

Sufiiarov, V. S., Popovich, A. A., Borisov, E. V., Polozov, I. A., Masaylo, D. V., & Orlov, A. V. (2017). The effect of layer thickness at selective laser melting. *Procedia engineering*, *174*, 126–134.

Sun, S., Brandt, M., & Easton, M. J. (2017). Powder bed fusion processes: An overview. *Laser additive manufacturing*, 55–77.

Sun, Y., & Hao, M. (2012). Statistical analysis and optimization of process parameters in Ti6Al4V laser cladding using Nd: YAG laser. *Optics and Lasers in Engineering*, *50*, 985–995.

Suresh, G., Narayana, K. L., & Mallik, M. K. (2019). Hardness, wear and corrosion properties of Co-Cr-W alloy deposited with laser engineered net shaping in medical applications. *Carbon (C)*, *2*, 3.

Svetlizky, D., Das, M., Zheng, B., Vyatskikh, A. L., Bose, S., Bandyopadhyay, A., . . . Eliaz, N. (2021). Directed energy deposition (DED) additive manufacturing: Physical characteristics, defects, challenges and applications. *Materials Today*, *49*, 271–295.

Thomareis, A. S., & Dimitreli, G. (2022). Techniques used for processed cheese characterization. In *Processed Cheese Science and Technology* (pp. 295–349). Elsevier.

Tonelli, L., Fortunato, A., & Ceschini, L. (2020). CoCr alloy processed by Selective Laser Melting (SLM): Effect of Laser Energy Density on microstructure, surface morphology, and hardness. *Journal of Manufacturing Processes*, *52*, 106–119.

Videršč̆ak, D., Schauperl, Z., Šolić, S., Ćatić, A., Godec, M., Kocijan, A., . . . Donik, Č. (2021). Additively Manufactured Commercial Co-Cr Dental Alloys: Comparison of Microstructure and Mechanical Properties. *Materials*, *14*, 7350.

Wai Cho, H. H., Takaichi, A., Kajima, Y., Htat, H. L., Kittikundecha, N., Hanawa, T., & Wakabayashi, N. (2021). Effect of Post-Heat Treatment Cooling Conditions on Microstructures and Fatigue Properties of Cobalt Chromium Molybdenum Alloy Fabricated through Selective Laser Melting. *Metals*, *11*, 1005.

Wang, J.-H., Ren, J., Liu, W., Wu, X.-Y., Gao, M.-X., & Bai, P.-K. (2018). Effect of Selective Laser Melting Process Parameters on Microstructure and Properties of Co-Cr Alloy. *Materials, 11*, 1546.

Wang, S., Zhao, X., Hsu, Y., He, Y., Wang, F., Yang, F., . . . Liu, Y. (2023). Surface modification of titanium implants with Mg-containing coatings to promote osseointegration. *Acta biomaterialia*.

Wang, X., Ning, B., & Pei, X. (2021). Tantalum and its derivatives in orthopedic and dental implants: osteogenesis and antibacterial properties. *Colloids and Surfaces B: Biointerfaces, 208*, 112055.

Wei, D., Koizumi, Y., Takashima, T., Nagasako, M., & Chiba, A. (2018). Fatigue improvement of electron beam melting-fabricated biomedical Co–Cr–Mo alloy by accessible heat treatment. *Materials Research Letters, 6*, 93–99.

Wei, L., Tingting, L., Wenhe, L., & Liyi, J. (2015). Study on selective laser melting forming process of cobalt chromium alloy. *Chinese Journal of Lasers, 42*, 0503001.

Weremfo, A., Abassah-Oppong, S., Adulley, F., Dabie, K., & Seidu-Larry, S. (2022). Response surface methodology as a tool to optimize the extraction of bioactive compounds from plant sources. *Journal of the Science of Food and Agriculture*.

Wilson, J. (2018). Metallic biomaterials: State of the art and new challenges. *Fundamental Biomaterials: Metals*, 1–33.

Wilson, J. M., Jones, N., Jin, L., & Shin, Y. C. (2013). Laser deposited coatings of Co-Cr-Mo onto Ti-6Al-4V and SS316L substrates for biomedical applications. *Journal of Biomedical Materials Research Part B: Applied Biomaterials, 101*, 1124–1132.

Wołosz, P., Baran, A., & Polański, M. (2020). The influence of laser engineered net shaping (LENS) technological parameters on the laser deposition efficiency and properties of H13 (AISI) steel. *Journal of Alloys and Compounds, 823*, 153840.

Wong, K. V., & Hernandez, A. (2012). A review of additive manufacturing. *International*

scholarly research notices, 2012.

Wu, M., Dong, X., Qu, Y., Yan, J., & Li, N. (2022). Analysis of microstructure and fatigue of cast versus selective laser-melted dental Co-Cr alloy. *The Journal of Prosthetic Dentistry, 128*, 218–e1.

Xiang, D. D., Wang, P., Tan, X. P., Chandra, S., Wang, C., Nai, M. L., . . . Liu, E. (2019). Anisotropic microstructure and mechanical properties of additively manufactured Co–Cr–Mo alloy using selective electron beam melting for orthopedic implants. *Materials Science and Engineering: A, 765*, 138270.

Xin, X.-z., Chen, J., Xiang, N., & Wei, B. (2013). Surface properties and corrosion behavior of Co-Cr alloy fabricated with selective laser melting technique. *Cell biochemistry and biophysics, 67*, 983–990.

Yadollahi, A., Mahtabi, M. J., Khalili, A., Doude, H. R., & Newman Jr, J. C. (2018). Fatigue life prediction of additively manufactured material: Effects of surface roughness, defect size, and shape. *Fatigue and Fracture of Engineering Materials and Structures, 41*, 1602–1614.

Yan, X., Cao, W., & Li, H. (2022). Biomedical Alloys and Physical Surface Modifications: A Mini-Review. *Materials, 15*, 66.

Yan, X., Lin, H., Wu, Y., & Bai, W. (2018). Effect of two heat treatments on mechanical properties of selective-laser-melted Co-Cr metal-ceramic alloys for application in thin removable partial dentures. *The Journal of prosthetic dentistry, 119*, 1028–e1.

Yang, A., Han, Y., Pan, Y., Xing, H., & Li, J. (2017). Optimum surface roughness prediction for titanium alloy by adopting response surface methodology. *Results in Physics, 7*, 1046–1050.

Ye, C., Zhang, C., Zhao, J., & Dong, Y. (2021). Effects of post-processing on the surface finish, porosity, residual stresses, and fatigue performance of additive manufactured metals: a review. *Journal of Materials Engineering and Performance, 30*, 6407–6425.

Yong, Z., Chang, L., Jiang, S., Xie, D., Xing, F., Shen, H., . . . Tian, Z. (2023). Parameter optimization of T800 coating fabricated by EHLA based on response surface methodology. *Optics and Laser Technology*, *158*, 108837.

Yung, K. C., Xiao, T. Y., Choy, H. S., Wang, W. J., & Cai, Z. X. (2018). Laser polishing of additive manufactured CoCr alloy components with complex surface geometry. *Journal of Materials Processing Technology, 262*, 53–64.

Zaman, H. A., Sharif, S., Kim, D.-W., Idris, M. H., Suhaimi, M. A., & Tumurkhuyag, Z. (2017). Machinability of cobalt-based and cobalt chromium molybdenum alloys-a review. *Procedia Manufacturing, 11*, 563–570.

Zhai, Y., Galarraga, H., & Lados, D. A. (2016). Microstructure, static properties, and fatigue crack growth mechanisms in Ti-6Al-4V fabricated by additive manufacturing: LENS and EBM. *Engineering failure analysis, 69*, 3–14.

Zhang, B., Li, Y., & Bai, Q. (2017). Defect formation mechanisms in selective laser melting: A review. *Chinese Journal of Mechanical Engineering, 30*, 515–527.

Zhang, W., Shang, X., Hu, M., He, X., Yang, B., Dai, K., . . . others. (2023). Microstructure and corrosion-wear behaviors for laser cladding repaired martensitic stainless steels using Co-based and Ni-based powders. *Materials Today Communications, 35*, 106287.

Zhang, X., & Liou, F. (2021). Introduction to additive manufacturing. In *Additive Manufacturing* (pp. 1–31). Elsevier.

Zhang, X., Li, W., & Liou, F. (2022). Additive manufacturing of cobalt-based alloy on tool steel by directed energy deposition. *Optics and Laser Technology, 148*, 107738.

Zhao, B., Song, J., Xie, L., Hu, Z., & Chen, J. (2021). Surface roughness effect on fatigue strength of aluminum alloy using revised stress field intensity approach. *Scientific reports, 11*, 1–17.

Zheng, B., Haley, J. C., Yang, N., Yee, J., Terrassa, K. W., Zhou, Y., . . . Schoenung, J. M. (2019). On the evolution of microstructure and defect control in 316L SS components

fabricated via directed energy deposition. *Materials Science and Engineering: A, 764*, 138243.

Zhou, Y., Li, N., Yan, J., & Zeng, Q. (2018). Comparative analysis of the microstructures and mechanical properties of Co-Cr dental alloys fabricated by different methods. *The Journal of prosthetic dentistry, 120*, 617–623.

Zhu, L., Xue, P., Lan, Q., Meng, G., Ren, Y., Yang, Z., . . . Liu, Z. (2021). Recent research and development status of laser cladding: A review. *Optics and Laser Technology, 138*, 106915.

APPENDICES

Appendix I: Publications

1. A.M Nyakundi, M.R Maina, R.V.S Prasad, E.O Olakanmi, and Sisa Pityana. Optimization of functional performance of additively manufactured cobalt-chromium-molybdenum alloy for dental implant applications. Journal of Manufacturing Processes, 120:1087-1103, 2024. https://doi.org/10.1016/j.jmapro.2024.05.005.

Appendix II: Chemical Composition of Cobalt-Chromium Molybdenum alloy

Table 1: Chemical composition of cobalt-chromium-molybdenum alloy (wt%)as per the manufacturer's specification.

Si	C	N	O	Co	Cr	Mn	Mo	Fe	S
0.712	0.01	0.096	0.039	Bal.	28.25	0.19	6.09	0.275	0.003

Appendix III: Flowability Study

The powder flow study was conducted to translate the powder feed rate from grams per minute (g/min) to revolutions per minute (rpm). The duration of powder flow was kept constant during the study (2 minutes). A particular feed rate value in rpm was set in the LENS machine, and the mass of powder was recorded after 2 minutes. The process was repeated thrice for each rpm. The flowability equation was then used to calculate the powder feed rate in rpm. Laser power was not used in the flowability study. Gas flow rate, spot diameter, layer thickness, and hatch spacing were also kept constant.

Table 1: Flowability study converting powder feed rate from grams per minute to revolutions per minute

Revolutions per minute	Grams per minute
1.50	1.50
1.50	1.50
1.50	1.50
2.00	2.00
2.00	2.50
2.00	3.00
2.50	2.50
2.50	3.00
2.50	2.50
3.00	3.50
3.00	3.50
3.00	3.50
3.50	4.00
3.50	5.50
3.50	3.00
4.00	5.50
4.00	4.50
4.00	4.50